

MULTI-COLOR LASER INDUCED FLUORESCENCE LIDAR

A DISSERTATION SUBMITTED TO THE GRADUATE DIVISION OF THE
UNIVERSITY OF HAWAI'I IN PARTIAL FULFILLMENT
OF THE REQUIREMENTS FOR THE DEGREE OF

DOCTOR OF PHILOSOPHY

IN

PHYSICS

AUGUST 2006

By
Troy T. Hix

Dissertation Committee:

John M.J. Madey, Chairperson
Pui K. Lam
Sandip Pakvasa
Eric B. Szarmes
Thomas Bopp

We certify that we have read this dissertation and that, in our opinion,
it is satisfactory in scope and quality as a dissertation for the degree of
Doctor of Philosophy in Physics.

DISSERTATION COMMITTEE

Chairperson

Copyright 2006

by

Troy T. Hix

To Mom and Dad,

Katsuko and Terry C. Hix.

Acknowledgements

During the course of this research, I have benefited from the support of many individuals and institutions. I would like to express my appreciation to all, and in particular I would like to thank the following:

My thesis advisor, Professor John M.J. Madey, for providing a complete educational experience from administering an excellent electrodynamics class to encouraging self guided laboratory conduct based on a fundamental understanding of the apparatus and of the physics. Under his vision and direction, the management structure maintained and administered in the FEL group has allowed me learn and successfully accomplish my daily tasks in an efficient manner. The weekly meetings (investigator, science, breakout) were excellent forums which provided organized communication channels with the FEL group administration and facilitated productive collaboration with my colleagues. His direct impact on daily laboratory tasks cannot be overstated. The successful fabrication of many of the custom apparatus used in this research significantly (sometimes entirely) depended on Dr. Madey's work. The most significant contributions include the "Hg pulser" (fabrication and integration into the YAG/dye laser system) discussed in Chapter 5 and the instrumentation technique (for example, the design of the high pass filter) in Chapter 6. To me, Dr. Madey serves as an exemplar not only as a scientist, but as a person by daily demonstrating an unwavering high level of integrity. To him I owe an enormous debt and offer my deepest gratitude.

Professor Eric B. Szarmes for his professional guidance during my apprenticeship. His lecture and laboratory courses in optics have formed the fundamental core of knowledge which I use in my daily work. He consistently encourages excellence (by example as well as by request) from those around him; working towards his expectations has allowed my work ethic and quality to improve tremendously since my arrival to the University of Hawaii.

Professor Pui K. Lam for his extraordinary patience and broad range of expertise when dealing with my specific questions during the course of this research. His unique ability to identify misconceptions and compose the perfect explanation when confronted with typical (i.e. naive) questions from students was very important to my understanding of the physical principles behind this research. In particular, the calculations in chapter two and the software used in chapters three and four have benefited from his direct influence.

Professor Sandip Pakvasa for being on my committee and clarifying density matrix methods in graduate quantum; Professor Thomas Bopp for joining my committee at the last minute yet still finding the time to complete a thorough review of this dissertation.

There were many UH faculty other than those on my committee who helped me along the way: Professor Fred Harris for his reading course in which I learned to program in C; Professor Shiv Sharma for giving me access to the equipment in his lab – my very first fluorescence data was acquired using the Argon ion laser and spectrometer in his lab; Professor Peter Crooker for his initial investigation into potential targets for this line of research was very valuable (AHI Design Note 3300-02); Professor Xerxes Tata for serving as my advisor during my first few years at the university – his continued interest in my education, even after I joined the FEL group, was very much appreciated; Professor Gary Varner for allowing access to his well equipped lab and donating the time of his students and the equipment in his lab – the fast photodiode used in Chapter 5 was developed through this collaboration; Professor Chester A. Vause for his collaboration when I first joined the FEL group; Dr. Teng Chen for her advice and direct help with the aromatic compound experiments in Chapter 5; Dr. Hugh Hubble for his initial work on procuring the laser sources used in this research; Dr. Barry Lienert for acting as a liaison between Dr. Sharma’s relatively well equipped research group and the FEL research group when it was first “gearing up” – Dr. Lienert has continued to work with our group and over the years has made many contributions to my research, one of the most valuable was the integration of the CCD array and the CT-103 monochromator.

Over the years, I have had the pleasure of working with some excellent graduate students. My peers provided me with the most tangible support since we were all going through the same difficulties simultaneously. I would like to specifically thank: Peter Grach positive attitude and support while I was composing my dissertation; Sigrid Greene for her help in graduate electrodynamics and for setting an example by graduating on time; Saddia Kemal for her help in the lab during some of the key data acquisition runs for this research – specifically the RF measurements in Chapter 6; Derrick Kong for his sound advice and dissertation LaTeX folder; Joseph Laszlo for his discussions on general education and dissertation advice (since we were on a parallel course to graduate in August 2006); Huan Ma for his conceptual help when ever I need clarification on spectroscopic principals; Frank Price for all his help over the years (we joined the group at nearly the same time, so he was my closest peer while I was conducting this research) – specifically his help in any

computer related issue from LabView to memory allocation in C, his collaboration on our data acquisition work to support Dr. Teng Chen, his procurement strategies for equipping the FEL laboratories when the labs were new, and his parallel work on the calculations and computer models in Chapter 3 and 4; Gang Sun for his expert advice concerning *any* mathematical difficulties I would have; and Amos Yarom for his contributions during qualifier exam study sessions and numerous conversations on physics.

Through the FEL group, I have had access to an excellent support staff. Henry Follmer, Melvin Matsunaga, Roy Tom, and Lehua Shelly have made valuable contributions to the design and fabrication of the custom hardware associated with the research presented here. I would also like to thank Fred Gladu, Bill Richert, and Gary Ridout from UMA Group Ltd for their lessons in organization and management. It is in this area I need the most help.

The significance of financial sponsorship in any research effort cannot be understated – it is in many ways essential. This research would not have been possible without the support of the U.S. Army Space & Missile Defense Command under contract # DASG60-99-C-0057 and DASG60-99-C-0048.

Finally, I would like to thank my family for all the years of support which only a family can provide, especially through the last few difficult years. Specifically, I would like to thank my brother, Thomas C. Hix for showing me that with a little kindness and inquisitive curiosity, the world will reveal its wonders.

ABSTRACT

Active remote detection methods using laser excitation (a sub-category of the broad field of “laser based imaging, detection, and ranging” or LIDAR) are known to be sensitive to relatively small concentrations (compared to atmospheric concentrations) of molecular targets when the excitation region is free of “contaminating” molecules. However, when one considers the detection of trace molecular constituents in the atmosphere, the broad non-resonant response of the abundant molecular atmospheric “contaminants” will overwhelm and mask the resonant response of the targeted molecular species, even when using ideal laser pulses.

This situation can be improved through the application of optical quantum control methods. Highly specialized laser pulse trains containing multi-color pulses with custom tuned properties are designed to control the target molecule and guide it to a particular final state which will fluoresce in a “dark” spectral region; a region free from the non-resonant response of the abundant molecular atmospheric contaminants. In this way the masking effects of the atmosphere are attenuated and the “contaminant free” sensitivity levels of LIDAR systems may be approached in low altitude remote detection applications.

In this dissertation, the basic equations of motion for molecular control are developed and numerically explored in the LIDAR context: thermal effects, random orientation effects, and collisional effects are considered. The impacts of the “stimulated Raman adiabatic passage” (STIRAP) process are numerically simulated given the apparent statistical and spatial properties of the tunable laser sources to which we have access. The fluorescence response of a molecular iodine isotope is compared natural iodine in a simplified numerical simulation resulting in a target signal eight orders of magnitude greater than the non-target in the “dark” spectral region.

The development of a three color dye laser apparatus is outlined. It was discovered that the laser output has features which will not allow coherent control of thermal molecular systems: the multi-mode nature of the dye laser output (transverse and axial) is measured and analyzed. The dissertation ends with a discussion of passive filtering techniques which may be implemented to render the dye laser output useable for bench-top demonstrations of the proposed remote detection method.

Contents

Acknowledgements	v
Abstract	viii
List of Figures	xii
List of Acronyms	xv
1 Introduction	1
2 General Analysis	4
2.1 Interaction formalism	5
2.1.1 General equation of motion	5
2.1.2 Two level system	7
2.1.3 Semi-classical behavior of a randomly oriented ensemble	9
2.1.4 Detuning effects	11
2.2 LIDAR geometries	13
2.2.1 Receiver phase space	13
2.2.2 Monochromator resolution	14
2.2.3 Velocity distribution	19
2.2.4 Side view geometry	20
2.2.5 Backscatter geometry	24
2.3 Conclusion	27
3 Population Transfer Simulations	29
3.1 Transform limited pulse sequences	30
3.1.1 One color	30
3.1.2 Two color	31
3.1.3 Three color	36
3.2 Random excitation amplitude simulations	40
3.2.1 Three π pulse sequence	42
3.2.2 STIRAP sequence followed by a π pulse	42
3.2.3 Three color optimal sequence	43
3.2.4 Histogram comparison	43
3.3 Stochastic collision model and density matrix methods	43

3.3.1	Collision model	45
3.3.2	Density matrix formalism	46
3.3.3	Collision model parametric fit	49
3.4	Conclusion	52
4	Molecular Laser Induced Fluorescence Simulations	54
4.1	Molecular iodine	55
4.1.1	Required (single color) beam properties to control iodine	55
4.1.2	Energy level model	56
4.2	Multi-color LIF simulation	57
4.2.1	The Lorentzian tail	57
4.2.2	Dynamics approximation	58
4.2.3	Single vs. three color LIF	60
4.3	Coherent population transfer	61
4.3.1	STIRAP pulse height insensitivity	63
4.3.2	The STIRAP detuning ridge	67
4.4	Conclusion	71
5	Laboratory Tests and Apparatus Development	73
5.1	Preliminary tests	74
5.1.1	Broadband molecular iodine absorption	74
5.1.2	Boxcar averager and Hg pulser	76
5.1.3	Red and green HeNe LIF	76
5.2	Dye laser test	77
5.2.1	Dye laser absorption in molecular iodine	78
5.2.2	Resonant laser induced fluorescence	79
5.2.3	Transition selection	81
5.3	Single fluorescence line decay	83
5.3.1	Pockels cell system integration	83
5.3.2	Single fluorescence line decay in molecular iodine	83
5.4	Aromatic compound LIF	85
5.5	Conclusion	86
6	Mode Content of the Dye Laser System	87
6.1	Transverse mode structure of the dye laser output	87
6.1.1	Experiment layout	88
6.1.2	M^2 estimate	88
6.1.3	Hermite-Gauss mode superposition	90
6.2	Dye laser output axial mode structure	91
6.2.1	Mode beating	92
6.2.2	Apparatus	92
6.2.3	Photodiode calibration	94
6.2.4	Experiment layout	97
6.2.5	Data acquisition	98
6.2.6	Data analysis	100

6.3	Conclusion	105
7	Issues for the Design and Operation of Multicolor Dye Laser Systems	106
7.1	General description	106
7.1.1	Single dye laser conditioning	106
7.1.2	Controlled three pulse sequence	108
7.1.3	Interaction and data acquisition	109
7.2	Layout	109
7.2.1	Dye laser table	109
7.2.2	Beam conditioning table	110
7.2.3	Interaction table	116
7.3	Filters	116
7.3.1	Pockels cells DC test	116
7.3.2	Pockels cells minimum pulse length	122
7.3.3	Pinholes	125
7.3.4	General discussion on etalon efficiency	128
7.3.5	Confocal etalon test	130
8	Conclusion	132
Bibliography		136

List of Figures

2.1	General LIDAR schematic	5
2.2	Semi-classical behavior of a randomly oriented ensemble	10
2.3	Extremum of the orientation averaged dynamics	10
2.4	Simulated thermal (Doppler only) effects on observed fluorescence – high fluence vs. low fluence	12
2.5	Ideal 1 m monochromator resolution (GHz)	15
2.6	Ideal 1 m monochromator resolution (inverse cm)	16
2.7	Ideal 1 m monochromator resolution (THz) for large slit widths	17
2.8	Ideal 1 m monochromator resolution (inverse cm) for large slit widths	18
2.9	Ideal 1 m monochromator resolution (nm) for large slit widths	19
2.10	Boltzmann-Maxwell distribution for molecular iodine	20
2.11	Side view geometry	21
2.12	Side-view lens optimization surface	21
2.13	Simulated thermal (Doppler and geometric) effects on observed fluorescence – 2 ns pulse	22
2.14	Simulated thermal (Doppler and geometric) effects on observed fluorescence – 200 ns pulse	23
2.15	Backscatter geometry	24
2.16	Number of molecules emitting into receiver in a LIDAR application	25
2.17	Required pulse energy to invert target molecules	26
3.1	Two level, single field diagram	30
3.2	Single color optimal solution	32
3.3	Single color optimal solution - increased pulse amplitude	32
3.4	Three level, two field diagram	33
3.5	Two pulse sequence example	34
3.6	Two color optimal pulse sequence (STIRAP)	35
3.7	Two color optimal solution	35
3.8	Two color optimal solution - increased pulse amplitude	36
3.9	$\log(\Phi_{\text{residue}})$ dependence on scaling Δ_α and A	37
3.10	Φ_{residue} dependence on scaling A and B	38
3.11	Four level, three field diagram	39
3.12	Three pulse sequence example	39
3.13	Three color optimal pulse sequence	40
3.14	Three color optimal solution	41

3.15	Three color optimal solution - increased pulse amplitude	41
3.16	Residue for runs using three π pulses	42
3.17	Residue for runs using the STIRAP sequence followed by a π pulse	43
3.18	Residue for runs using three color STIRAP	44
3.19	Stochastic simulation histograms	44
3.20	Collisionless evolution of a three state system	45
3.21	Evolution of a three state system with collisions - example 1	46
3.22	Evolution of a three state system with collisions - example 2	47
3.23	Average dynamics of one million stochastic runs	51
4.1	Required fluence for inversion of the two level iodine molecule	56
4.2	Single transition diagram	59
4.3	"N" transition diagram	59
4.4	Simulated single color LIF from non-target molecule (iodine non-isotope) .	61
4.5	Simulated single color LIF from target molecule (iodine isotope)	62
4.6	Simulated three color LIF from target molecule (iodine isotope)	62
4.7	Residue surface for various pulse intensities	63
4.8	Amplitude "robustness" of the two color STIRAP	64
4.9	Amplitude "non-robustness" of the three color STIRAP	65
4.10	STIRAP inversion of a randomly oriented ensemble	66
4.11	Inversion probability across a Gaussian beam profile	67
4.12	STIRAP detuning ridge	68
4.13	STIRAP detuning ridge fit	68
4.14	Stokes and pump pulses in a Λ system	69
4.15	Simulated three π -pulse pathway LIF line strengths (target)	70
4.16	Simulated three π -pulse pathway LIF line strengths (non-target)	70
4.17	Simulated STIRAP + π -pulse pathway LIF line strengths (target)	71
4.18	Simulated STIRAP + π -pulse pathway LIF line strengths (non-target)	72
5.1	Red LED absorption in molecular iodine	74
5.2	Yellow LED absorption in molecular iodine	75
5.3	Green LED absorption in molecular iodine	75
5.4	Red HeNe LIF from the "baked potato" iodine cell	77
5.5	Red HeNe LIF from a "clean" commercial iodine cell (Thorlabs)	78
5.6	Iodine absorption dye laser scan	79
5.7	535.8901 nm LIF from the "baked potato" iodine cell	80
5.8	535.8843 nm LIF (from "transition one")	82
5.9	535.8901 nm LIF (from "transition two")	82
5.10	Decay of 535.893 nm LIF line at 632.9 nm	84
5.11	LIF from a solid anthracene flake illuminated by a 355 nm YAG	85
5.12	Grating ghosts from 1064 nm laser illumination	86
6.1	Dye laser output M^2 estimate	89
6.2	Transverse beam profiles from Spiricon camera	90
6.3	Superposition of the first four Hermite-Gauss modes	91
6.4	Boxcar gate placement for RF beat measurement	94

6.5	Photodiode calibration block diagram	95
6.6	Photodiode calibration fit	96
6.7	Block diagram RF beat spectrum measurement	97
6.8	Highpass filter response	98
6.9	Photodiode signal through the highpass filter (and 14 dB attenuator)	99
6.10	Dye laser #22 scanned with the 7L12	101
6.11	Dye laser #22 scanned with the 7L14	101
6.12	Dye laser #23 scanned with the 7L12	102
6.13	Dye laser #23 scanned with the 7L14	102
6.14	Both dye lasers scanned with the 7L12 (raw data)	103
6.15	Both dye lasers scanned with the 7L14 (raw data)	103
6.16	Dye laser # 23, with YAG pump with the seeder on/off, scanned with the 7L12 (raw data)	104
6.17	Gaussian fit for a single RF beat spectral feature	104
7.1	Single dye laser conditioning block diagram	107
7.2	Three conditioned and synchronized dye lasers block diagram	108
7.3	Interaction and data acquisition block diagram	109
7.4	Laser positions on dye laser table	111
7.5	YAG beam positions	112
7.6	Dye beam positions	113
7.7	Beam mileposts and optics on the dye laser table	114
7.8	Beam conditioning table	115
7.9	Interaction table beam mileposts and optical component labels	117
7.10	Interaction table beam positions	118
7.11	Beam mileposts and optics on the dye laser table	119
7.12	DC test of 628nm coated Pockels cell	120
7.13	DC test of 532nm coated Pockels cell	120
7.14	Pulse length data/calculation table	122
7.15	Pockels cell minimum pulse length (temporal profiles)	123
7.16	Pockels cell minimum pulse length (spectral profiles)	124
7.17	TEM00 envelope for dye laser #21	126
7.18	Rayleigh range (724 nm) and spot size vs. pinhole diameter	127
7.19	Energy in the Airy function central max vs. pinhole size.	128
7.20	Green HeNe transmission through a scaned confocal etalon	129
7.21	Green HeNe transmission through a scaned confocal etalon (zoom)	131
7.22	Green HeNe transmission through a scaned near confocal etalon	131

List of Acronyms

ADC Analog-to-Digital Converter

AR Anti-Reflection

CCD Charge-Coupled Device

CW Continuous Wave

DC Direct Current

FCF Franck-Condon Factor

FEL Free Electron Laser

FSR Free Spectral Range

FWHM Full Width Half Maximum

HeNe Helium-Neon Laser

LED Light Emitting Diode

LIDAR Light Imaging Detection and Ranging

LIF Laser Induced Fluorescence

ND Neutral Density

PC Personal Computer

PMT PhotoMultiplier Tube

RF Radio Frequency

SNR Signal to Noise Ratio

STP Standard Temperature and Pressure

STIRAP Stimulated Raman Adiabatic Passage

TTL Transistor Transistor Logic

UV Ultraviolet

YAG Yttrium Aluminum Garnet

Chapter 1

Introduction

This research is motivated by the need to develop “laser imaging, detection, and ranging systems” (LIDAR) in the context of remote sensing. Currently, LIDARs have various applications in geology and atmospheric physics: detecting the Seattle Fault through dense vegetation cover [4], mapping glaciers [5], conducting planetary surveys [57], and atmospheric monitoring [25, 30].

There are many applications of remote sensing LIDARs from monitoring ozone distributions [29] to military applications. We seek to explore the selectivity and sensitivity limit of laser induced fluorescence based LIDAR techniques. Relatively modest LIDAR systems [40] exhibit sensitivity to very low concentrations (less than a particle/cm³) of target molecules. The limiting mechanism is interference from non-target molecules. At low altitudes, the concentration of molecules in the atmosphere is around 10¹⁹ molecules/cm³.

Coherent control of a quantum system was experimentally realized in 1946 [13] in a system of interacting nuclear paramagnets. The formalism associated with the dynamics [59] generates equations of motion identical to those for an atomic system interacting with a coherent laser field [18, 12] (they are also identical to the equations governing power transfer between coupled electronic modes [53]). Adiabatic inversion of atomic systems with light pulses was first suggested by Treacy [82] in 1968. For general reviews on the current state of coherent control methods in laser spectroscopy see references [34], [8], [64], and [36], where recent research efforts that apply sophisticated optical control methods to molecular systems theoretically [11, 75, 20, 35, 16, 61, 43, 87] and experimentally [35, 85, 63, 70] are described; even a new state of matter, phaseonium, has been named [72, 2].

The main noise issue in LIDAR applications is the intervening atmosphere, not just between the target region and the receiver but also at the target region itself. In the

following argument, we ignore the effects of the intervening atmosphere between the target region and transmitter/receiver. This assumption is suspect for long range demonstrations since the intervening atmosphere may alter key characteristics of the laser beam on its way to the target region; however, for bench top demonstrations, this assumption is valid since the path length between the transmitter and target region is relatively small.

Once a pulse train is transported to the target region, with its key characteristics intact, one must still contend with the distinct possibility that the non-target molecules will emit/scatter radiation along with the target molecules. At concentration ratios near unity, careful selection (or tuning) of the excitation laser pulse wavelength is usually enough to ensure the target fluorescence dominates; however, when one considers the problem of detecting low concentration targets, i.e. smaller than a part per billion, simple wavelength tuning is not sufficient to bring the SNR above unity. This is mainly due to two factors. First, the molecular constituents of the atmosphere typically have a dense energy level structure making the tuning approach analogous to hitting an archery target through a thick grove of trees. Secondly, the fluorescence process is exponentially damped in time, giving it a Lorentzian response in frequency. This gives rise to the famous 6dB/octave roll off, which allows the weak fluorescence response from an abundant non-target molecule to dominate the strong fluorescence response from a dilute target molecule.

Inspired by the recent successes in the application of quantum control to molecular systems [85, 3, 68] we propose that application of the concepts and methods of multi-color coherent molecular control to the LIDAR remote sensing problem will lead to systems with increased sensitivity and selectivity. Through the use of computer simulations, it is shown that multi–color techniques might allow signal (target molecule) to noise (non–target atmospheric constituents) ratios around 10^8 , implying remote detection of trace molecules in the atmosphere with concentrations as low as 10^{11} molecules/cm³ (unity SNR). Motivated by these theoretical insights, we execute a battery of basic laboratory tests to develop the apparatus, methods, and knowledge associated with multi-color spectroscopy. This work took place in six main stages using molecular iodine as a trial target: 1) broadband absorption spectroscopy using “light emitting diode” (LED) output, 2) red and green HeNe laser induced fluorescence (LIF), 3) narrowband absorption spectroscopy using dye laser output, 4) resonant LIF using dye laser output, 5) resonant LIF decay (single line), and 6) dye laser output mode spectrum diagnostic. In stage (6) it is discovered that some of the inherent characteristics of the dye laser sources used here are incompatible with molecular

coherent control. Currently, research efforts are centered on dealing with the multi-mode nature of these laser sources.

In the following chapters, significant and original contributions to the merger of quantum control and remote sensing LIDAR systems are highlighted. Chapters 2-4 describe analytic and numerical studies; the key results are an analysis of the average behavior of excited molecules when one takes into account the thermal properties (random orientation and velocity) of the target, the effects of different LIDAR geometries when the phase space constraints of the detector system are taken into consideration, the increased target/non-target discrimination obtained by using three color coherent population transfer, the advantages of the “saturation” effect of the STIRAP process and its line shape.

Chapter 5 presents a chronological description of the stages of laboratory development. The most significant data sets include three LED absorption spectra, a relatively large spectral scan of resonant dye laser induced fluorescence from a modestly prepared sample cell, a demonstration of transition discrimination in the molecular iodine energy manifold, and the temporal profile of a single resonant dye laser induced fluorescence line. An aromatic compound LIF experiment which exposes a short coming of the 1 m monochromator in the lab is included to underscore the developmental nature of these tests and to emphasize the fact that iodine is only a trial molecule: there are many possibilities for future demonstrations.

Chapter 6 encompasses an entire stage of laboratory development because of the importance and complexity of the stage: an extensive analysis of the mode content of the dye lasers. Detailed measurements of the dye laser RF beat spectrum and the dye laser transverse profiles are presented. The transverse mode profile is modeled using the Gauss-Laguerre resonator modes.

Chapter 7 describes the current system design and discusses the remaining issues that need to be addressed before multi-color experiments can start. Beam line design including delay lines seems trivial until one considers the implementation of filtering systems to reduce the number of modes in the dye laser output. The results from an initial set of measurements of Pockels cell performance, a discussion of the efficiency of narrow band etalons, a discussion on the integration of pinhole filters into the beam line, and a test of a confocal etalon are presented.

Chapter 2

General Analysis

This chapter presents the main points from two basic studies: the equations of motion describing the interaction of the laser field and the target system are developed, and the connection between this research and the LIDAR remote sensing problem (see Figure 2.1) is established. We analyze the impact of random molecular *classical* orientation and the thermal distribution of molecular velocities on the average observed behavior in LIF benchtop experiments; and the fundamental limits of LIDAR systems are explored using simple geometric and phase space arguments.

This is an idealized introduction. Many details are ignored to clarify the arguments. The formalism is very simplified and will be revisited in later chapters. In the phase space analysis of LIDAR systems, details of the detection process are ignored. The only detector feature preserved is the finite phase space available to the receiver. The acceptance phase space of the Interactive Technologies CT-103 1 m monochromator is used as a prototype and is by no means optimal (integrating spheres and atomic/molecular detection methods could increase the phase space available to the receiver). In an actual deployable system, a full analysis along the lines of the methods used in reference [6] should be used.

Many introductory texts [53, 88, 15, 71] outline the methods and assumptions used here to derive the equations of motion. These results are used to derive the average behavior of a randomly oriented ensemble. Reference [74] gives the well known expression for the Maxwell-Boltzmann speed distribution from the kinetic theory of gases. This distribution is used to model the effects of the random motion of the target molecules on observed intensity fluctuations. Reference [37] describes the Liouville Theorem and reference [67] describes the “ABCD” matrix method of ray tracing which were both used to find the optimal lens combination of the receiver in the bench top experiment.

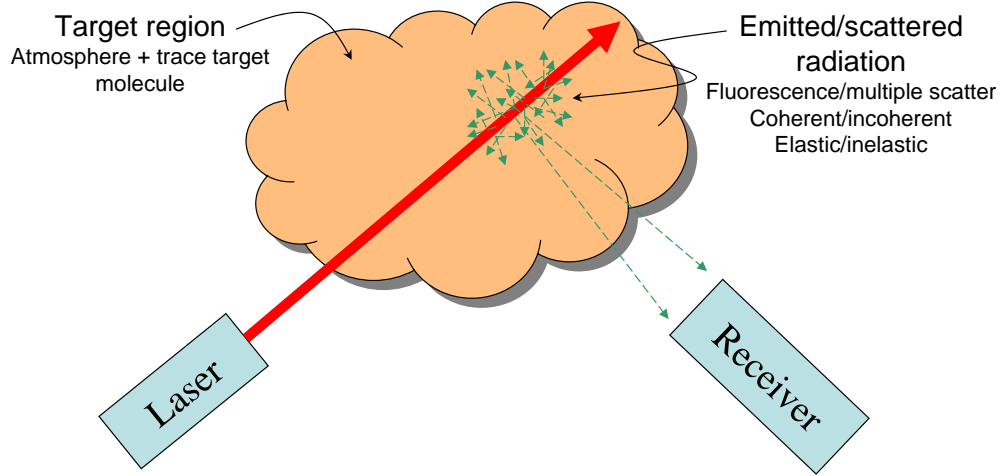


Figure 2.1: General remote sensing LIDAR schematic. A laser beam is used to excite a region of atmosphere while a receiver (telescope) collects the resulting emitted/scattered radiation. The spectral and temporal features of the acquired signal are used to determine the relative abundance of specific trace molecules.

2.1 Interaction formalism

The proposed detection scheme revolves around the laser excitation of a thermal target; i.e. the interaction of a highly prepared optical beam with a relatively unprepared system at equilibrium with ambient conditions. The general equation of motion is derived, the simple example of a two level system subject to a single mode field is examined, and the effects of random orientation and detuning effects are included.

2.1.1 General equation of motion

Consider an atom which interacts with a multi-mode radiation field. We model the interaction with the minimal-coupling Hamiltonian under the dipole approximation in the radiation gauge [71]:

$$H = H_0 + H'. \quad (2.1.1)$$

where H_0 is the Hamiltonian of the atomic system, namely

$$H_0 |a\rangle = \hbar\omega_a |a\rangle \quad (2.1.2)$$

where $|a\rangle$ is some energy state of the atom, and $\hbar\omega_a$ is the energy of the state $|a\rangle$; the energy eigenbasis $\{|x\rangle\}$ is assumed complete for electrons bound to the nucleus of the atom (ionization and scattering states are not included here). H' is the interaction Hamiltonian, namely

$$H' = e\vec{E}_n \cdot \vec{r}, \quad (2.1.3)$$

where e is the charge of an electron, \vec{E}_n is the local electric field at the atom due to the nth radiation mode (assumed uniform over the atom), and \vec{r} is the coordinate of the electron (the atomic nucleus is the origin).

If the modes are linearly polarized in the same direction and coherent then the fields can be written as

$$\vec{E}_n = \hat{\varepsilon} E_n \frac{e^{i(\nu_n t + \phi_n)} - e^{-i(\nu_n t + \phi_n)}}{2i} \quad (2.1.4)$$

where $\hat{\varepsilon}$ is the unit polarization vector for the modes, E_n is the magnitude of the nth mode, ν_n is the frequency of the nth mode, and ϕ_n is the arbitrary phase of the nth mode. Now we can write

$$H' = \sum_n \frac{1}{2i} E_n M e^{i(\nu_n t + \phi_n)} + c.c. \quad (2.1.5)$$

where

$$M \equiv e\hat{\varepsilon} \cdot \vec{r} \quad (2.1.6)$$

represents the amplitude of the coupling for the nth mode.

The system obeys the Schrödinger equation

$$i\hbar \dot{|\psi\rangle} = H |\psi\rangle. \quad (2.1.7)$$

If we project the general solution $|\psi\rangle$ into $\{|x\rangle\}$, i.e.

$$|\psi\rangle = \sum_a c_a(t) e^{-i\omega_a t} |a\rangle \quad (2.1.8)$$

where $c_a(t)$ is the probability amplitude associated with state $|a\rangle$ for $|\psi\rangle$, then Equation 2.1.7 can be rewritten as [15]

$$\dot{c}_a = \frac{1}{i\hbar} \sum_b H'_{ab} e^{(i\omega_{ab} t)} c_b \quad (2.1.9)$$

where

$$H'_{ab} = \langle a | H' | b \rangle, \quad |a\rangle, |b\rangle \in \{|x\rangle\} \quad (2.1.10)$$

and

$$\omega_{ab} = \omega_a - \omega_b \quad (2.1.11)$$

is the transition energy. Now we combine Equations 2.1.5 and 2.1.9 to obtain the equation of motion for an atom interacting with a multi-mode radiation field:

$$\boxed{\dot{c}_a = \sum_{b,n} \frac{E_n M_{ab}}{2\hbar} (e^{-i\nu_n t} - e^{i\nu_n t}) e^{i\omega_{ab} t} c_b,} \quad (2.1.12)$$

where M_{ab} (called the dipole matrix element) is defined as

$$M_{ab} \equiv \langle a | M | b \rangle, \quad |a\rangle, |b\rangle \in \{|x\rangle\}. \quad (2.1.13)$$

Finally, we introduce

$$\xi = \frac{2\hbar}{eE_o a_o} \quad (2.1.14)$$

where e is the elementary charge, E_o is an arbitrary constant with units of the electric field, and a_o is the Bohr radius, so that Equation 2.1.12 can be written in the dimensionless form (convenient for computer simulations)

$$\frac{dc_a}{d\tau} = \sum_{b,n} \Delta_{abn} (e^{-i\nu_n \xi \tau} - e^{i\nu_n \xi \tau}) e^{i\omega_{ab} \xi \tau} c_b \quad (2.1.15)$$

where

$$\Delta_{abn} = \xi \frac{E_n M_{ab}}{2\hbar} \quad (2.1.16)$$

and

$$\tau = \frac{t}{\xi}. \quad (2.1.17)$$

2.1.2 Two level system

If we assume that

$$\omega_b - \omega_a \neq \omega_c - \omega_a \quad (2.1.18)$$

then pairs of states can be selectively and unambiguously coupled. For real optical beams and real atoms this condition must be generalized to account for laser mode structure/bandwidth and atomic (molecular) transition line widths. Suppose there exists a system in which this is true for at least one transition and consider the simplest example of a single mode field interacting resonantly between the states involved in the transition. Using the rotating

wave approximation [90] and a single mode with frequency $\nu \equiv \omega_1 - \omega_0$, one can show that Equation 2.1.15 reduces to

$$\dot{c}_0 = -\Delta c_1 \quad (2.1.19a)$$

$$\dot{c}_1 = +\Delta c_0 \quad (2.1.19b)$$

where $\Delta \equiv \Delta_{10} = \Delta_{01}$ and $|0\rangle, |1\rangle \in \{|x\rangle\}$. Of the two selectively coupled states, state $|0\rangle$ is the “ground” (initially occupied), and state $|1\rangle$ is the targeted excited state (initially unoccupied).

The solution to Equation 2.1.19 can be written as

$$P_1(\tau) = \sin^2(\Delta \cdot \tau) \quad (2.1.20)$$

where $P_1(\tau) \equiv |c_1|^2$ is the probability of finding the system in the excited state $|1\rangle$. When $\Delta \cdot \tau = \pi/2$ the probability of finding the system in $|1\rangle$ is unity, thus whatever portion of the ensemble which was in $|0\rangle$ at $\tau = 0$ will be in $|1\rangle$ when τ satisfies $\Delta \cdot \tau = \pi/2$. It is convenient to define a “Rabi” frequency associated with the dynamics described by Equation 2.1.19; in the literature the “Rabi” frequency is defined as the angular frequency associated with one complete oscillation (twice the angular frequency associated with the argument of the sine function in Equation 2.1.20 since it is squared) or

$$\Omega_R \equiv 2 \frac{\Delta}{\xi} = \frac{E_n M_{ab}}{\hbar}. \quad (2.1.21)$$

Now Equation 2.1.20 becomes

$$P_1(t) = \sin^2\left(\frac{\Omega_R}{2}t\right)$$

(2.1.22)

where t is in seconds.

Next we seek to derive a relationship between parameters of a tophat pulse with electric field amplitude E and duration t and the resulting fluence when given a specific value of $\Delta\tau$ (usually $\pi/2$). From Equations 2.1.16 and 2.1.17 we see that the electric field provided by the pulse satisfies

$$E = \frac{(\Delta\tau)2\hbar}{Mt} \quad (2.1.23)$$

where $E \equiv E_0$ is the electric field associated with the single mode in this example; thus, the fluence required is

$$f = 2c\hbar^2\epsilon_o(\Delta\tau)^2 \frac{1}{M^2 t}$$

(2.1.24)

where ϵ_0 is the permittivity of free space. When only considering the final state of the two level system, it can be shown [7] that the *area* under the amplitude (not intensity) profile of the pulse determines the final state; thus, for a given desired final state, we may concern ourselves with only the total energy contained in the pulse used to excite the system and ignore the exact shape of the profile. Hence, Equation 2.1.24 is valid regardless of the pulse shape (even though it was derived for a tophat).

2.1.3 Semi-classical behavior of a randomly oriented ensemble

Suppose there exists an ensemble of molecules in which we can assign a classical dipole moment to each molecule. Let an incident beam of coherent linearly polarized light interact with each molecule through its dipole moment such that the coupling strength is proportional to $\hat{p} \cdot \hat{\varepsilon}$ where \hat{p} is the direction of the dipole moment and $\hat{\varepsilon}$ the direction of the beam polarization. If the system is unprepared, i.e. we assume it is in thermodynamic equilibrium with its surroundings, the “orientation polarization” of the system will be completely incoherent.

Specifically, the normalized dipole vectors of the molecules will be uniformly distributed on the surface of the unit sphere and hence the projections of these vectors against the polarization axis of the incident light are also uniformly distributed. Thus, since the dipole interaction depends linearly on this projection, the distribution of coupling strengths in the ensemble will be uniformly distributed between zero and the maximum case (when the polarization and the dipole moment vectors point in the same direction).

Since the frequency of the Rabi oscillations depend linearly on the matrix element, the Rabi frequency is uniformly distributed in the ensemble. Now, for some molecule with a Rabi frequency reduced from the maximum by a factor $F \in [0, 1]$, the probability of excitation at time τ

$$P_1(\tau) = \sin^2((F\Delta) \cdot \tau) \quad (2.1.25)$$

Thus, since the distribution is uniform, the average behavior of a (large) ensemble is

$$P'(\tau) = \int_0^1 \sin^2(F\Delta\tau) dF = \frac{1}{2} (1 - \text{sinc}(2\Delta\tau)) \quad (2.1.26)$$

or

$$P'(t) = \frac{1}{2} (1 - \text{sinc}(\Omega_R t)) \quad (2.1.27)$$

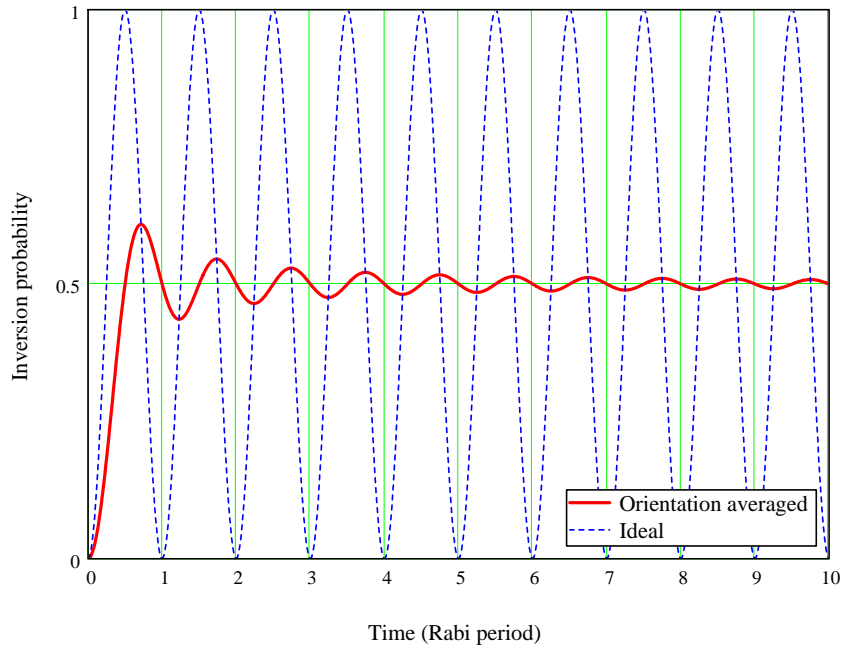


Figure 2.2: Semi-classical behavior of a randomly oriented ensemble. Equation 2.1.20 is shown as the “ideal” behavior while the semi-classical result, Equation 2.1.26, is called “orientation averaged”.

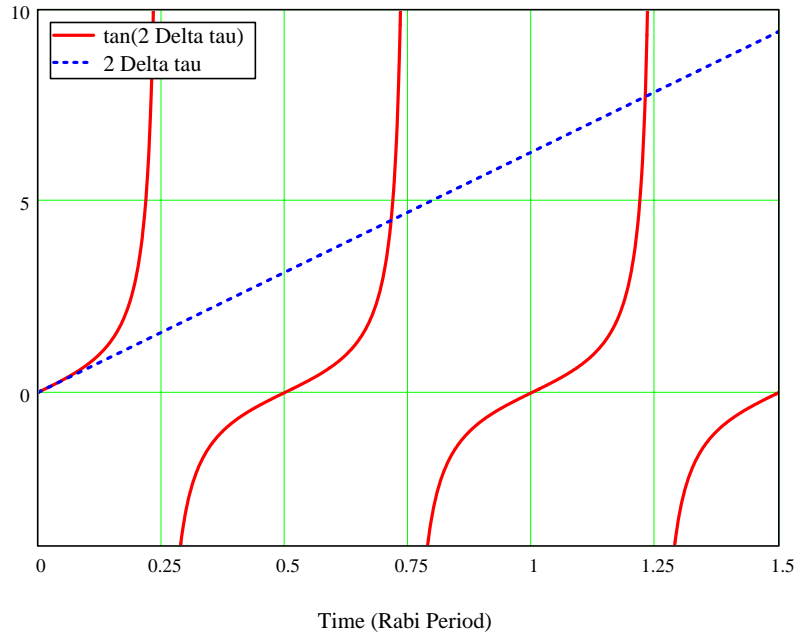


Figure 2.3: Extremum of the averaged dynamics. The two intersections shown here represent the first absolute maxim and first local minim of the semi-classical behavior shown in Figure 2.2. The first maximum has moved from $1/2$ Rabi period to about 0.715148 Rabi period. The first minimum, which ideally occurs at one Rabi period, has moved to about 1.229512 Rabi period.

where

$$\text{sinc}(x) \equiv \frac{\sin(x)}{x}. \quad (2.1.28)$$

See Figure 2.2 for a comparison between the ideal dynamics of a single molecule and the average behavior our thermal ensemble.

By examining the derivative of Equation 2.1.26 one finds that the extrema are located at the solutions to

$$2\Delta\tau = \tan(2\Delta\tau). \quad (2.1.29)$$

See Figure 2.3 for a plot of the solution. The implications of these results are that more power will be required to induce the molecules to invert within a give time window (due to the forward shift of the maxima) and the resulting inversion probability will be reduced by a factor of ~ 0.6 . It can be shown that this is a worse case scenario (in terms of reduced modulation depth and forward shift of the maxima) when one compares this semi-classical behavior to the behavior resulting from a quantum mechanical treatment of the dipole approximation in the spherical harmonic basis set (personal communication, Pui K. Lam, June 2006).

2.1.4 Detuning effects

Consider the same two level system studied in section 2.1.2. If we start with the same assumptions except instead of perfect resonance we allow for a small mismatch between the excitation field and the transition under consideration (i.e. $\nu \sim \omega_1 - \omega_2$) we get

$$\dot{c}_0 = -\Delta e^{i\xi\tau(\delta\omega)} c_1 \quad (2.1.30a)$$

$$\dot{c}_1 = +\Delta e^{i\xi\tau(-\delta\omega)} c_0 \quad (2.1.30b)$$

where $\delta\omega = \nu - (\omega_1 - \omega_2)$, $\Delta \equiv \Delta_{10} = \Delta_{01}$, and $|0\rangle, |1\rangle \in \{|x\rangle\}$. Of the two selectively coupled states, state $|0\rangle$ is the “ground”, i.e. initially occupied; and state $|1\rangle$ is the targeted excited state, initially unoccupied.

The solution to 2.1.30 is

$$c_0 = \exp\left(i\frac{\Phi}{2}\tau\right) \left(\cos\left(\frac{\Omega}{2}\tau\right) - i \sin\left(\frac{\Omega}{2}\tau\right) \right) \quad (2.1.31a)$$

$$c_1 = \frac{2\Delta}{\Omega} \exp\left(-i\frac{\Phi}{2}\tau\right) \sin\left(\frac{\Omega}{2}\tau\right) \quad (2.1.31b)$$

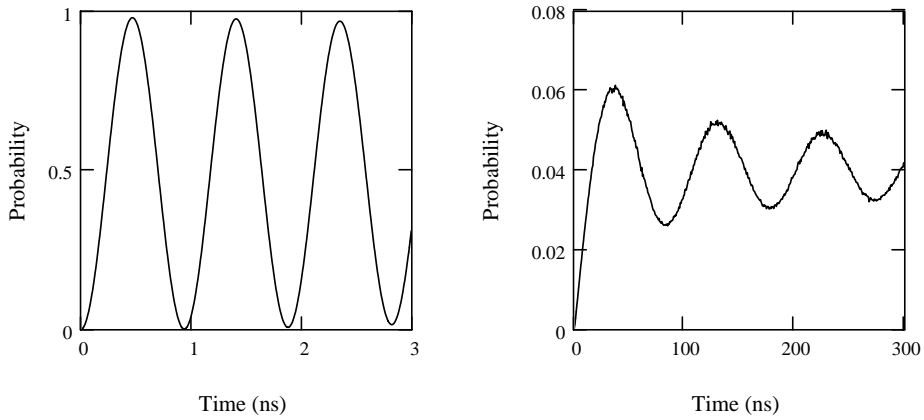


Figure 2.4: Simulated thermal (Doppler only) effects on observed fluorescence – high fluence vs. low fluence. For these two simulations we use a fluence of 1000 J/m^2 for the left plot and a fluence of 10 J/m^2 for the right plot. The target is thermal molecular iodine gas with dipole matrix element $3.6 \times 10^{-32} \text{ Cm}$ (including FCF), at $T = 293 \text{ K}$.

where $\Phi \equiv \xi \cdot \delta\omega$ (dimensionless detuning) and $\Omega \equiv \sqrt{\Phi^2 + 4\Delta^2}$. Now

$$P_1(\tau) = \left(\frac{2\Delta}{\Omega} \right)^2 \sin^2 \left(\frac{\Omega}{2} \tau \right) \quad (2.1.32)$$

or

$$P_1(\tau, \Phi) = \frac{1}{1 + \left(\frac{\Phi}{2\Delta} \right)^2} \sin^2 \left(\Delta\tau \sqrt{1 + \left(\frac{\Phi}{2\Delta} \right)^2} \right) \quad (2.1.33)$$

where $P_1(\tau) \equiv |c_1|^2$. This can be rewritten as

$$P_1(t, \delta\omega) = \frac{1}{1 + \left(\frac{\delta\omega}{\Omega_R} \right)^2} \sin^2 \left(\frac{\Omega_R}{2} t \sqrt{1 + \left(\frac{\delta\omega}{\Omega_R} \right)^2} \right). \quad (2.1.34)$$

Clearly we would like to work in the limit $\delta\omega/\Omega_R \ll 1$ (this is equivalent to $\Phi/2\Delta \ll 1$); unfortunately, this ratio is near unity for ambient atmospheric targets excited with ns laser pulses. Ω_R must be faster than the relaxation processes in the atmosphere, about 1ns; thus $\Omega_R \sim 1 \text{ GHz}$. $\Delta\omega$ is forced to be at least 0.36 GHz due to Doppler broadening; however, laser line broadening produces an equivalent effect, thus the transform limit of the 1 ns laser pulse will place a lower limit on $\delta\omega$: again about 1 GHz. See Figure 2.4 for a comparison between “fast” population transfer (using a 2 ns pulse) and a “slow” transfer (using a 200 ns pulse).

2.2 LIDAR geometries

For a geometry appropriate for a benchtop demonstration experiment (side view), a computer model is used to explore the effects of phase space constraints of thermal velocities on the photon capture probability. In the last subsection (Section 2.2.5), a simple geometric argument is applied to general LIDAR systems to place limits on the photon capture probability and quantify the required pulse energies for molecular control.

2.2.1 Receiver phase space

Consider the linear systems of ray optics where rays are traced through a series of optical components [67]. The rays are assigned two parameters at each position z along the beam line: x (or y) which represents the distance from the optic axis and α which represents the angle the ray makes with the optic axis. The rays form vectors in a *phase space* in which their motion down the beam line is modeled; x (or y) corresponds to the *position* coordinate while α (which is related to the transverse velocity of the ray) corresponds to the *momentum* coordinate. Optical components such as thin lenses or drift regions (free space regions between lenses) are represented by matrices which can be used to transform any ray to some other position along the beam line. In this study, “bundles” of rays are tracked along various beam lines to determine the collection efficiency of two beam line geometries appropriate for LIF investigation.

In terms of the ray optics phase space described above, any receiver in an optical system can be assigned a finite region of phase space to which it is sensitive. This region can be transformed to the target region where it can be overlapped with the phase space of the fluorescence in the target region. The Liouville Theorem [37] states that the bundle of rays will flow through phase space as an incompressible fluid. This places a fundamental limit to the coupling between the receiver and target region. Suppose the receiver has an acceptance “half” angle of 0.07 radians (this was an initial estimate for the monochromator used in the experiments described later in this dissertation). If we assume the spatial extent of the fluorescence is not a limiting factor, then with respect to the angular limits, the Liouville Theorem states that the receiver is sensitive to at most

$$\frac{0.14^2}{4\pi} = 0.00156 \quad (2.2.1)$$

or a little over one thousandth of the emitted energy.

Moreover, this phase space overlap, in combination with a molecular density and inversion probability, can be interpreted as a “photon capture probability” for the detection system. For example, suppose there were 2×10^5 molecules in the sensitive region and 50% of the molecules were inverted and decayed optically; then the angular overlap from Equation 2.2.1 implies we should capture 156 photons in our detection system.

2.2.2 Monochromator resolution

The resolution of the 1 m monochromator is calculated from simple assumptions. Suppose monochromatic light is incident on a rectangular slit. The far field diffraction pattern (1 m away) is collimated and sent to a diffraction grating. We assume the significant portion of the illuminated grating completely contains the central maximum of the far field diffraction pattern (squared sinc function). The angular width of the central maximum is given by

$$\theta = 2 \arcsin \left(\frac{\lambda}{a} \right) \quad (2.2.2)$$

where λ is the wavelength of the monochromatic light and a is the width of the slit. Thus, the number of lines illuminated on the grating is (assuming small angles)

$$\kappa = L\theta\rho = L2\frac{\lambda}{a}\rho \quad (2.2.3)$$

where L is the distance between the input slits and the collimating optic and ρ is the groove density of the grating.

The resolving power R of a grating monochromator can be written in terms of the number of illuminated grooves using the Rayleigh criterion [38]

$$R = \frac{\lambda}{\Delta\lambda} = m\kappa \quad (2.2.4)$$

where m is the diffraction order. Thus

$R = 2mL\rho\frac{\lambda}{a}$

(2.2.5)

For the Interactive Technology CT-103 monochromator $m = 1$, $L = 1$ m, and $\rho = 1200$ lines per mm. The grating in the CT-103 is about $3\frac{7}{8}$ " wide; thus there is an additional constraint on Equation 2.2.5:

$$2\frac{\lambda}{a}L < 3\frac{7}{8}" \quad (2.2.6)$$

For small slit widths (5–50 microns) figure 2.5 (2.6) shows the resolution of the CT-103 calculated from Equation 2.2.5 for various wavelengths in GHz (inverse cm). Figures 2.7,

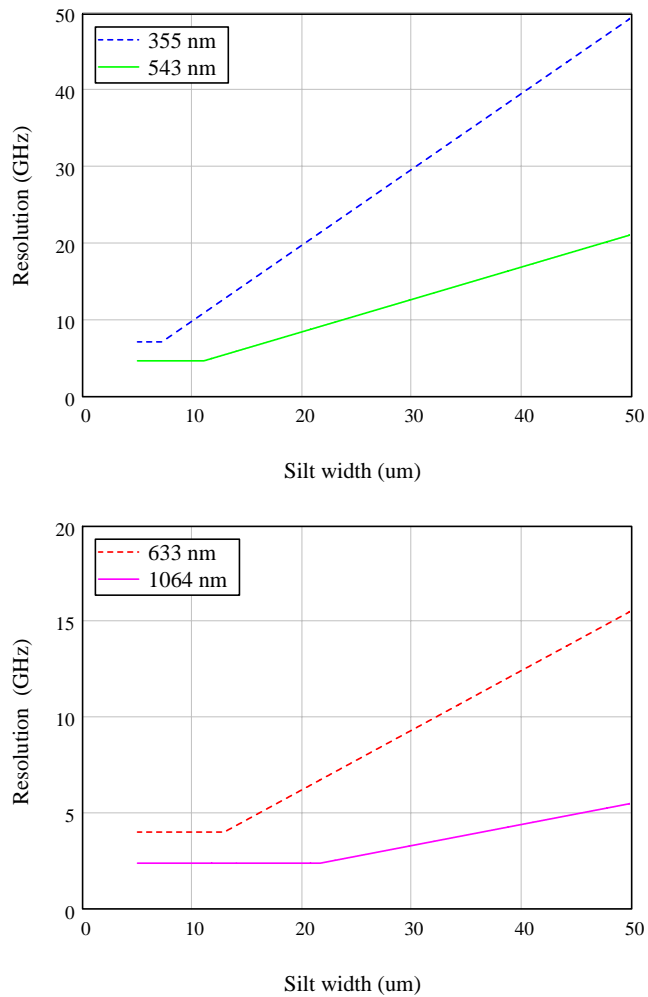


Figure 2.5: Ideal 1 m monochromator resolution (GHz)

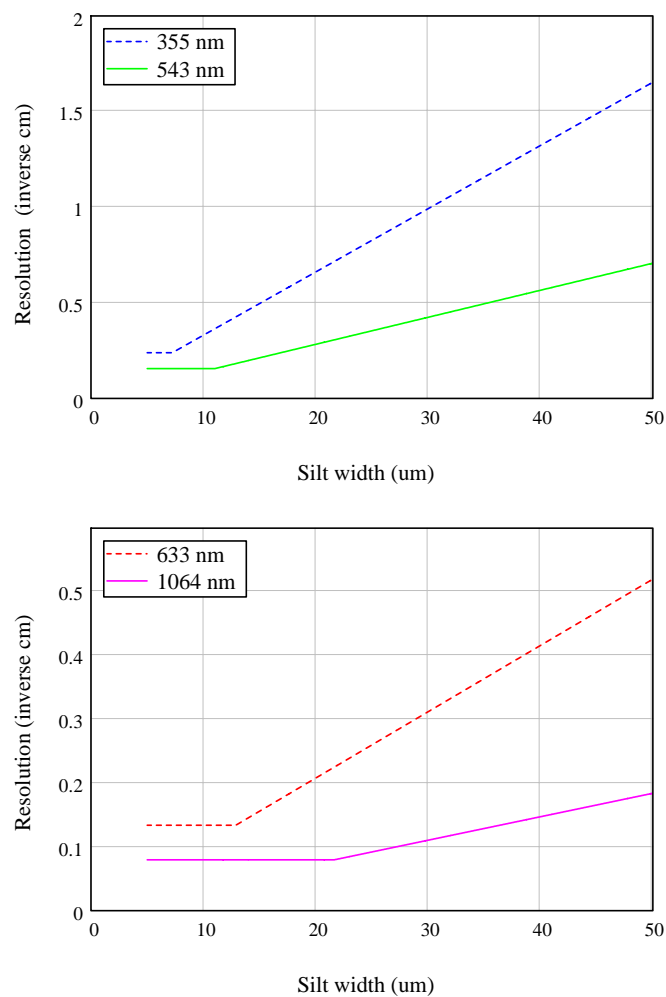


Figure 2.6: Ideal 1 m monochromator resolution (inverse cm)

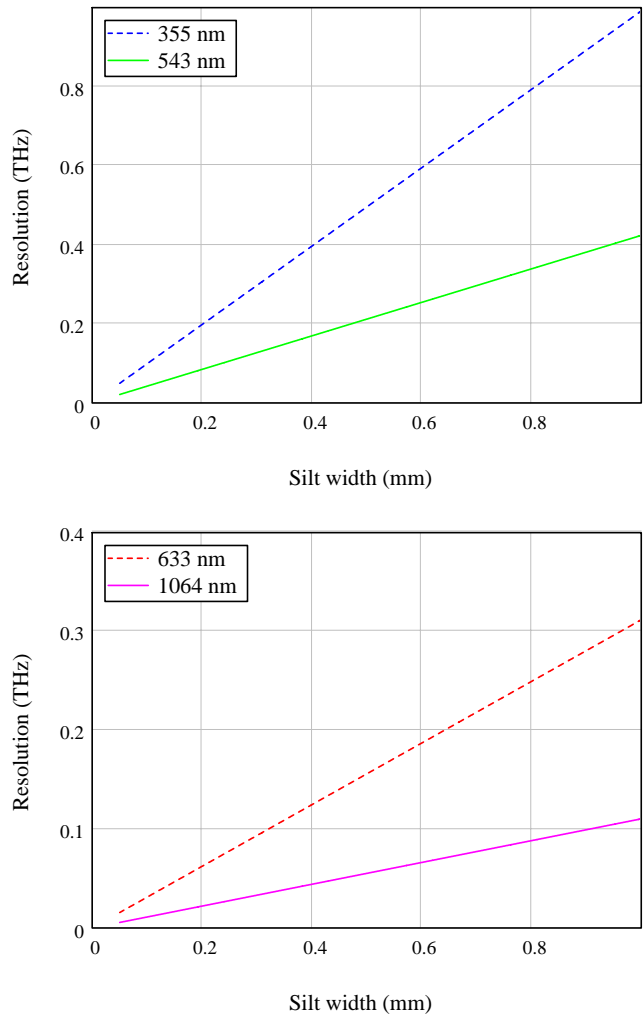


Figure 2.7: Ideal 1 m monochromator resolution (THz) for large slit widths

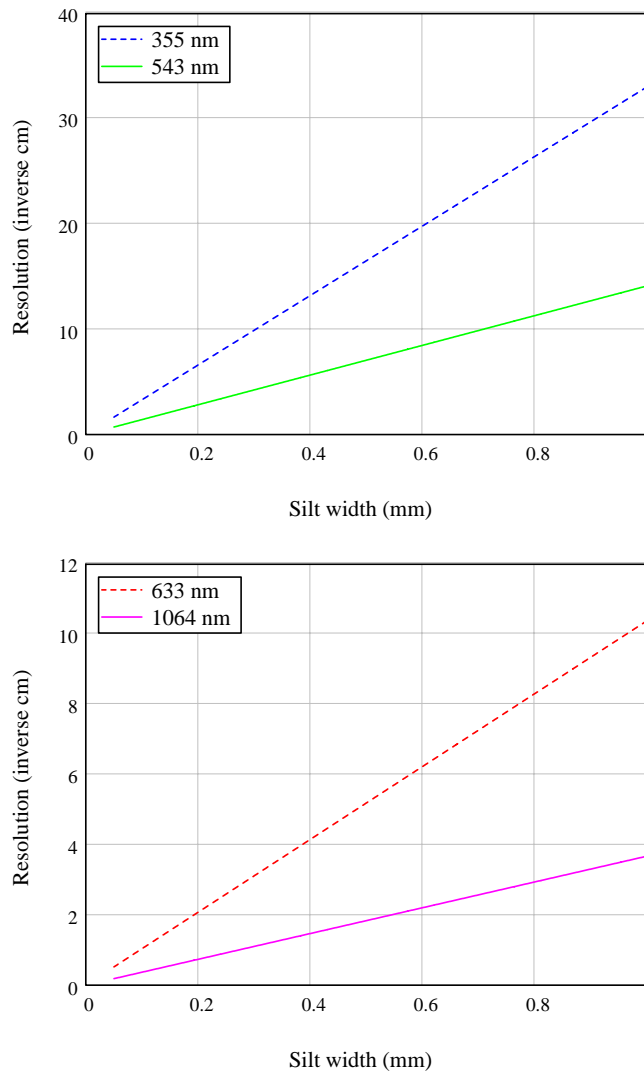


Figure 2.8: Ideal 1 m monochromator resolution (inverse cm) for large slit widths

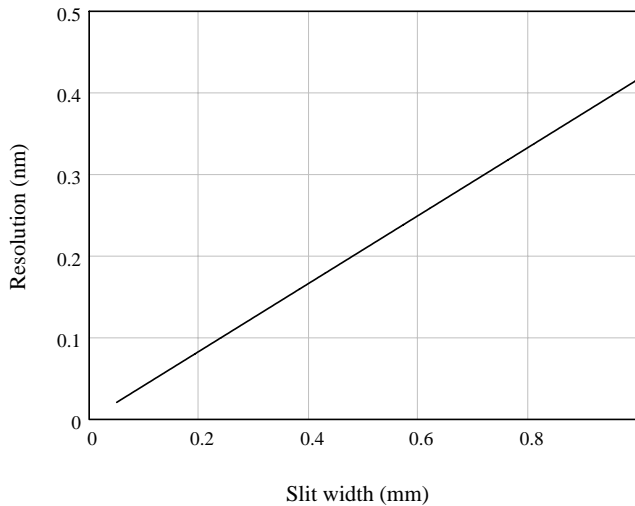


Figure 2.9: Ideal 1 m monochromator resolution (nm) for large slit widths - Equations 2.2.4 and 2.2.5 imply $\Delta\lambda = a/(2mL\rho)$; here the resolution ($\Delta\lambda$) is plotted for $m = 1$, $L = 1$ m, and $\rho = 1200$ lines per mm.

2.8, and 2.9 show the resolution of the CT-103 for larger slit widths (50–1000 microns).

2.2.3 Velocity distribution

The distribution of molecular speeds in a gas is governed by Maxwell-Boltzmann statistics. This distribution impacts this study through the equation of motion (Equation 2.1.34) as a Doppler shift and through the “geometric” effects associated with linear molecular motion in the target region. The Doppler shift is proportional to the projection of the molecular velocity vector onto the laser beam wave front normal; the effects of the Doppler shift are described in Section 2.1.4. The “geometric” effects are the temporal modulation of the excitation the molecule experiences by either leaving the excitation region before the pulse ends or entering the excitation region after the pulse has already started (or both). Additionally, the point in time at which the molecule emits its fluorescence photon may occur after the molecule leaves the region to which the receiver is sensitive.

The Maxwell-Boltzmann probability density function for molecular speeds is given by [74]

$$\rho(|v|) = \sqrt{\frac{2}{\pi}} \left(\frac{m}{kT}\right)^{\frac{3}{2}} v^2 \exp\left(-\frac{mv^2}{2kT}\right) \quad (2.2.7)$$

where k is the Boltzmann constant, T is the temperature (in K), m is the molecular mass, and v^2 is the square of the molecular speed. See Figure 2.10 for a plot of this distribution.

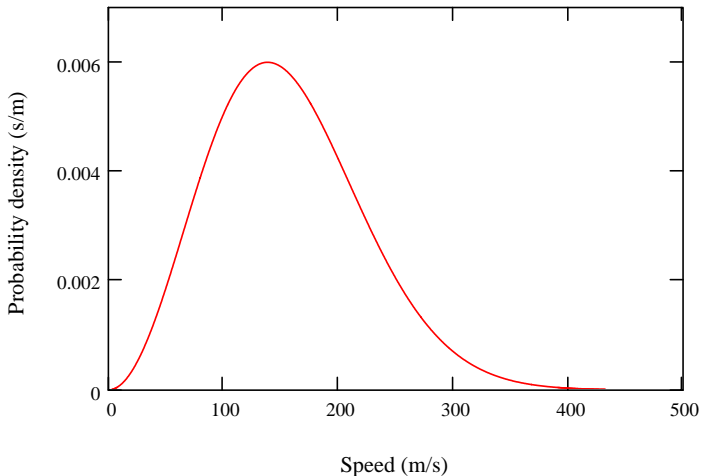


Figure 2.10: Boltzmann–Maxwell distribution for molecular iodine. For this plot and associated simulations, $T = 293$ K, $m = 2 \times 127$ u ($u = 1.6605402 \times 10^{-27}$ kg). The root mean square speed is 167 m/s, the average speed is 156 m/s, and the most probable speed is 139 m/s.

2.2.4 Side view geometry

Consider an optical setup where a laser beam line is intersected orthogonally at its focus by a receiver beam line. Let a coordinate system be centered at the intersection where the z-axis corresponds to the receiver beam line and the x-axis corresponds to the laser beam line (see Figure 2.11). Ray bundles (corresponding to the sensitive phase space region for the CT103 monochromator) are transformed to the intersection and the overlap with focused laser beam is determined. Based on that overlap, an “excited sensitive volume” is defined at the target region for various two-lens combinations in the receiver beam line. The overlap will naturally include any cropping of phase space in the angular dimension. A solid angle of acceptance is defined and the excited sensitive volume is scaled by the ratio of this solid angle over 4π . The surface formed by this scaled volume (as a function of lens focal lengths) is used to determine the optimal lens combination for laboratory scale versions of the side view geometry. See Figure 2.12 for a resulting surface applicable to a bench top experiment.

Suppose we choose a symmetric pair of 200mm lenses (i.e. unity magnification), now we can examine the dynamic and geometric effects of the velocity distribution on the detection system. Using the same geometry as above, we construct a rectangular region at the intersection to represent the sensitive volume with respect to the detection system (the “sensitive” volume). The height of the region in the y-direction is equal to the height of

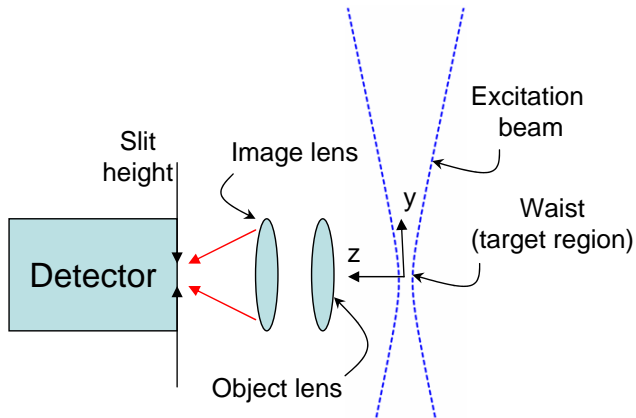


Figure 2.11: Side view geometry. For the calculation in Figure 2.12, each object (image) lens is placed one focal length from the target region (detector input). The slit such that its long dimension (height) is oriented in the y-direction and its narrow dimension is oriented in the x-direction.

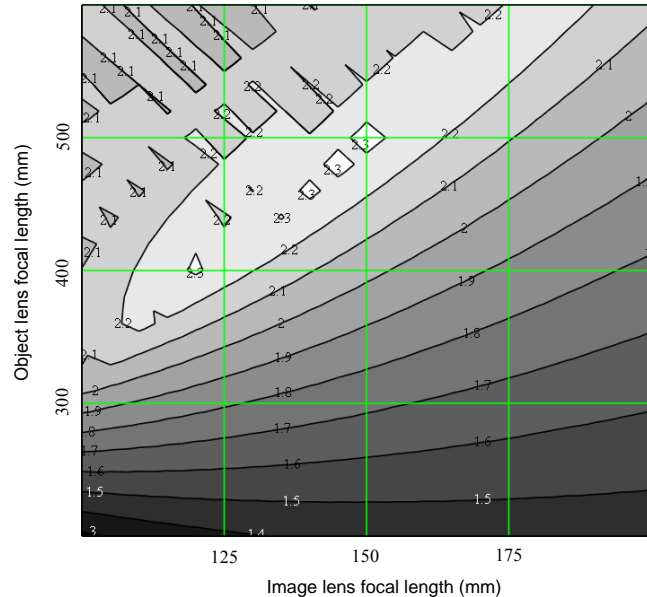


Figure 2.12: Side-view lens optimization surface. For this calculation the beam waist diameter is 1 mm, the wavelength is $0.63 \mu\text{m}$, the slitwidth is $300 \mu\text{m}$, the slit height is 0.5 cm, and the monochromator acceptance angle is 52 mrad. The object lens is placed one focal length from the sample, while the image lens is placed one focal length from the monochromator input. The units for the contour in the plot are 10^{-12} m^3 (scaled volume). Thus if the target was air (near 10^{25} molecules per cubic meter) we would expect this system to be sensitive to 10^{13} atmospheric molecules (assuming all molecules decay optically in an isotropic fashion).

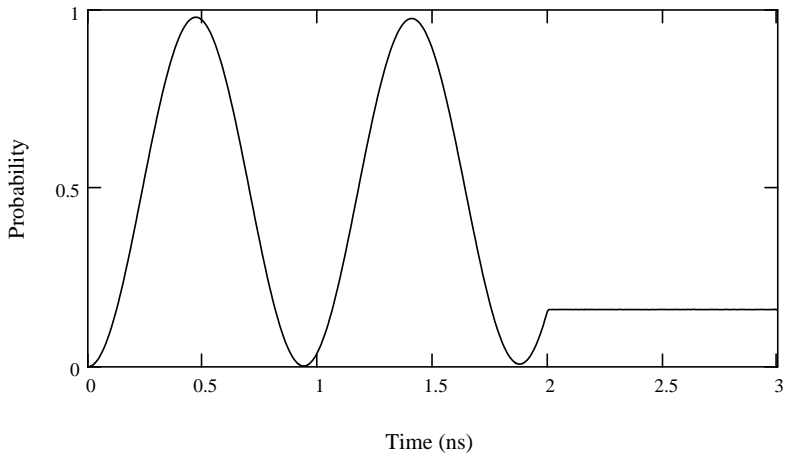


Figure 2.13: Simulated thermal (Doppler and geometric) effects on observed fluorescence – 2 ns pulse. For this simulation a top hat pulse (temporal and spatial) with duration 2 ns, fluence of 1000 J/m^2 , and beam diameter 1 mm (about 1 mJ per pulse), excites a thermal molecular iodine gas, with dipole matrix element $3.6 \times 10^{-32} \text{ Cm}$ (including FCF), at $T = 293\text{K}$. The axial dimension of the sensitive region is set to $300 \mu\text{m}$; this is set to the slit width, which is selected such that the J-splitting in iodine fluorescence can still be resolved. The transverse dimension of the sensitive region is set to 0.5 cm (slit mask).

the monochromator input slit. The width of the region in the z-direction and x-direction is equal to the width of the monochromator input slit. Laser beam excitation of the region is modeled by a second rectangular region (also centered at the intersection) which is temporally switched (top hat envelope with a width equal to the laser pulse length). The width of the region in the z-direction and x-direction is equal to the waist diameter of the laser beam. The height of the region in the y-direction is equal to the Rayleigh range of the laser beam.

An ensemble of molecules is generated in the sensitive region and tracked backwards in time, starting from some time t , to determine the average effect of molecular velocity on the ensemble dynamics at some instant. The ensemble is uniformly distributed in the volume and given the Maxwell-Boltzmann speed distribution (the velocities are isotropic). Each member of the ensemble is ballistically tracked and the duration and delay of its exposure to the excitation volume is recorded. The evolution of the (two level) molecule is calculated according to Equation 2.1.34 and; thus, by averaging over the entire ensemble, the average probability of inversion is calculated for molecules in the detector's sensitive region at time t . This is repeated for many times t to track the average behavior of the ensemble for some time interval. See Figures 2.13 and 2.14 for some results applicable to

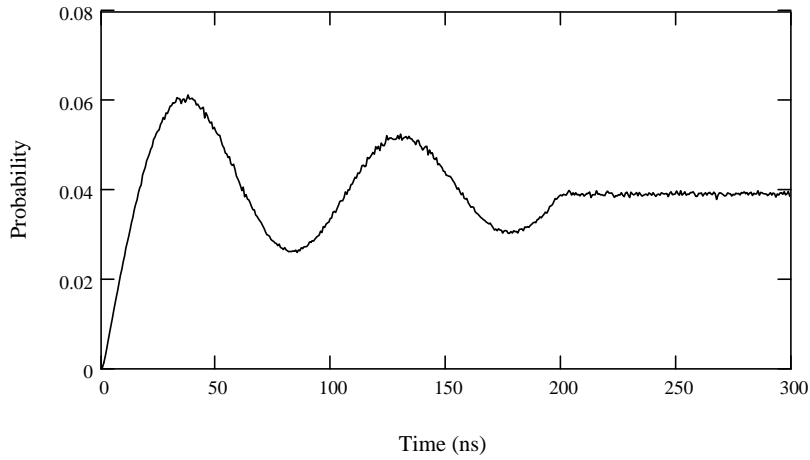


Figure 2.14: Simulated thermal (Doppler and geometric) effects on observed fluorescence – 200 ns pulse. The calculations presented here have nearly the same parameters as Figure 2.13 (left is ideal, right is polarization averaged) except these require a smaller fluence of 10 J/m^2 to induce two complete oscillations in 200 ns (instead of 1000 J/m^2 for 2 ns). The peak power of the pulse is 50 W – four orders of magnitude larger than the typical CW HeNe laser.

a bench top experiment. Comparing these two Figures to Figure 2.4 we see that geometric effects are insignificant when using relatively large waists (and the molecules are relatively heavy and slow like iodine).

Even if we assume all of the inverted molecules decay optically, the collisional decay rate places limits on the number of photons emitted from the ensemble. If the collision rate dominates, it can be shown that (personal communication, Pui K. Lam, June 2006)

$$n = \frac{\tau_c}{\tau_s} N \quad (2.2.8)$$

where n is the number of emitted photons, τ_c is the collision life time, τ_s is the spontaneous life time, and N is the number of inverted molecules. Using the above results we can obtain an estimate for the number of photons captured in the detection system. Assuming the density of molecular iodine at 293K is near 10^{21} per m^3 , the scaled volume (from Figure 2.12) is near $2 \times 10^{-12} \text{ m}^3$, the maximum inversion probability is near 6×10^{-2} (down from around 0.6 – see Figure 2.14), and $\tau_c/\tau_s = 0.1 \times 10^{-6}/7 \times 10^{-3} \sim 1 \times 10^{-5}$ (τ_s is derived using the same matrix element mentioned in the caption of Figure 2.13); then the total number of photons captured in the monochromator should be near 1200. It should be noted that for the 2 ns pulse (Figure 2.13), even though the maximum inversion probability (0.6) is an order of magnitude larger; the ratio $\tau_c/\tau_s = 1 \times 10^{-9}/7 \times 10^{-3} \sim 1 \times 10^{-7}$ is two orders of

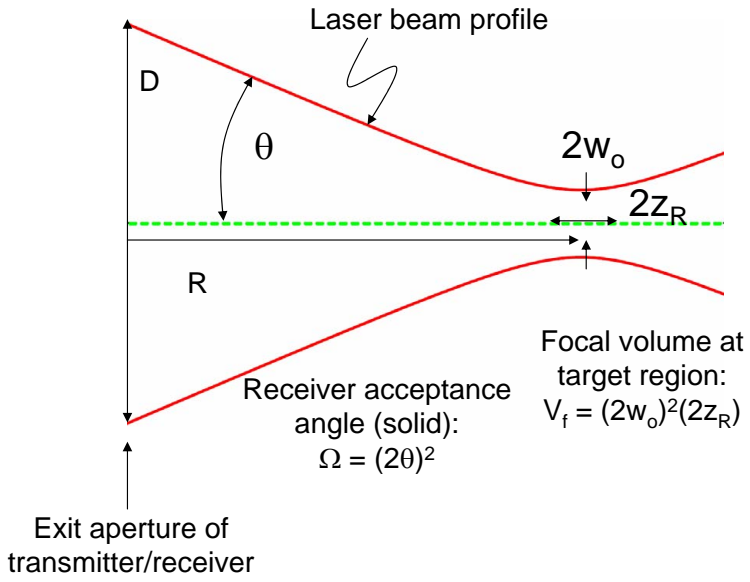


Figure 2.15: Backscatter geometry. After leaving the exit aperture of diameter D , a laser beam is brought to a focus a distance R from the aperture. The dimensions of the focal volume and the far-field divergence (θ) depend only on D , R , and the laser wavelength λ .

magnitude *smaller* for a reduced number of captured photons when compared to the 200 ns pulse.

2.2.5 Backscatter geometry

Consider an optical setup where a laser beam line is merged with receiver beam line. The merge could be facilitated through the use of a dichroic beam splitter: reflecting the wavelength associated with the laser while transmitting the broad spectrum associated with the fluorescence radiation. By allowing some of the laser focusing optics to double as the receiver optics gives rise to unique geometries where the receiver and laser source are localized and their beam lines are extended to some remote target region (a LIDAR application). See Figure 2.15 for a beam line diagram.

The probability of photon detection is proportional to

$$ABCD \int \int \rho(\vec{r}) P(\vec{r}, t) \Phi(\vec{r}, \hat{c}) d\vec{r} d\Omega \quad (2.2.9)$$

where A is the fraction of target molecules which couple to the laser radiation, B represents atmospheric attenuation effects like Mie scattering, absorption, etc., C represents the fraction of excited molecules that decay optically within the bandwidth of the detector, D

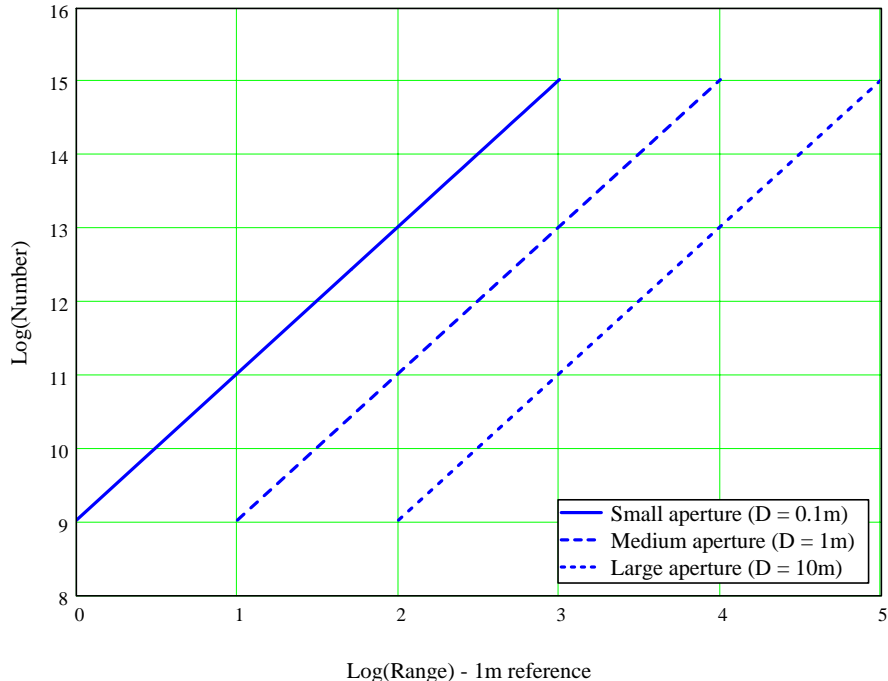


Figure 2.16: Number of molecules emitting into receiver acceptance area (ideal: $A = B = C = D \equiv 1$ in Equation 2.2.9). The ratio R/D must be larger than unity to satisfy the approximations used to construct Equations 2.2.12 and 2.2.11. Here we have used $\lambda = 1 \mu\text{m}$, and a density of 10^{25} molecules per m^3 . Thus, with an aperture of $D = 1 \text{ m}$ and a focal length of 1 km, we expect the system to be sensitive to at most 10^{13} atmospheric molecules.

represents the fraction of optically decaying molecules which emit a photon before collisional effects force non-optical decay (see discussion at the end of Section 2.2.4), $\rho(\vec{r})$ is the density distribution of the target molecules, $P(\vec{r}, t)$ is the molecular inversion probability (this is a function of the fluence at position \vec{r} and at time t), $\Phi(\vec{r}, \hat{c})$ is the phase space factor (a function of position as well as the direction of travel of the emitted photon \hat{c}). In the following analysis some approximations are made to estimate this integral. First we ignore A , B , C , and D , thus we simply calculate the photon capture probability assuming all molecules optically decay isotropically. The density is assumed uniform, Φ is simply taken to limit the integration volume to the focal volume and introduce a factor equal to the solid angle fraction available to the detector from the target region, and P is assumed to be equal to unity.

The output aperture, with diameter D , is taken as the origin and the target is at the focus of a Gaussian beam which is some distance, R , from the output aperture. The Gaussian beam emerges from the output aperture with a clear aperture compatible with a far-field ripple of less than 1% [76]. The integration limits are taken as the boundaries of a

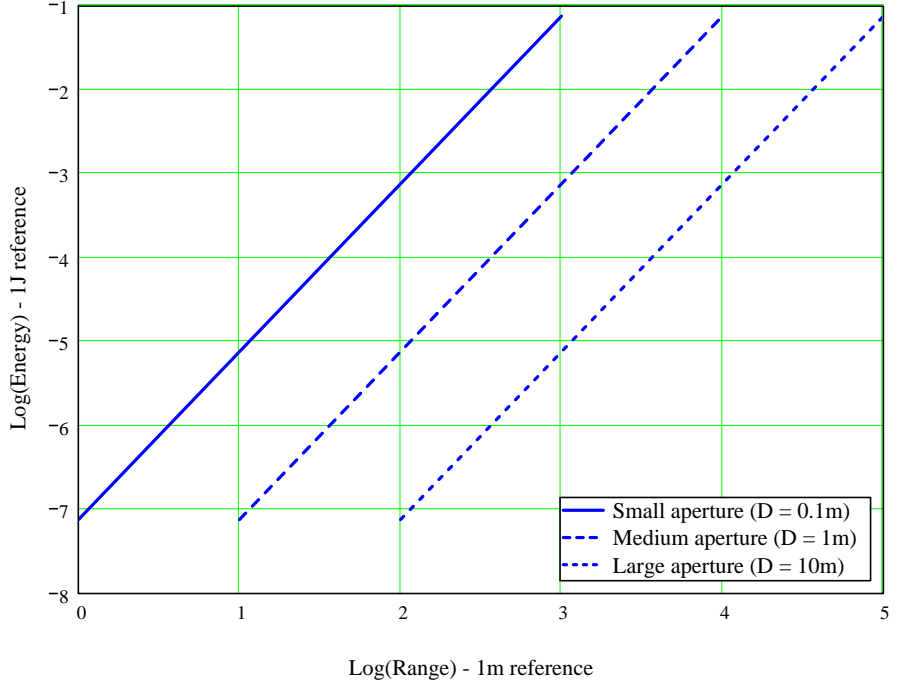


Figure 2.17: Required pulse energy to invert target molecules. Here we have used the dipole matrix element approximated in Section 4.1.1 ($M = 3.6 \times 10^{-32}$ Cm), tophat pulse duration $t = 1$ ns, $\lambda = 1$ μ m, and $\Delta\tau = \pi/2$ in Equation 2.2.12.

rectangular volume centered at the focus: the extent of the region along the beam axis is taken as the Rayleigh range and the transverse dimensions are taken as the waist diameter. The solid angle fraction is taken as

$$\frac{(2\theta)^2}{4\pi} \quad (2.2.10)$$

where θ is the far-field divergence *half* angle of the Gaussian beam [76]. Using these ideas, one can arrive at the following expression for the scaled volume (the product of the volume and the solid angle fraction)

$$V_{eff} = \frac{4.6^2}{2\pi^2} \lambda^3 \left(\frac{R}{D}\right)^2. \quad (2.2.11)$$

The required pulse energy depends on the fluence (Equation 2.1.24) and the focal spot diameter. The relationship is

$$E = \frac{42.32}{\pi} c \hbar^2 \epsilon_o \frac{(\Delta\tau)^2}{M^2 t} \lambda^2 \left(\frac{R}{D}\right)^2. \quad (2.2.12)$$

See Figures 2.16 and 2.17 for plots of these functions for various aperture sizes.

The key features of these equations illustrate the potential sensitivity and limitations of LIDAR geometries when one is concerned with LIF type experiments. The effective sensitive volume, Equation 2.2.11, *increases* as the square range, R . The obvious drawback is seen in Equation 2.2.12 where the required energy also increases with the square of the range. Indeed the ratio

$$\frac{V}{E} = \frac{1}{4\pi c \hbar^2 \epsilon_0} \frac{M^2 t}{(\Delta\tau)^2} \lambda \quad (2.2.13)$$

should be maximized for the most efficient application. λ has a natural upper limit set by atmospheric transmission: optical wavelengths greater than 10 um are heavily attenuated. Collisional damping at STP forces t to be less than 1 ns. $\Delta\tau$ is $\pi/2$ for Rabi oscillation population inversion; however, some coherent process require the quantity to increase by an order of magnitude or more (see Chapter 3). Most molecules have matrix elements, M , around one D ($D = 10^{-18}$ esu and 1 Cm = 2.99792458×10^9 esu).

2.3 Conclusion

The equations of motion for population inversion of a thermal ensemble excited by a linearly polarized laser beam are presented; and the basic equations governing the collection efficiency of general LIDAR systems are developed. We have introduced the basic equations upon which other results in this dissertation are based. The calculated limits on collection efficiency will be referenced later to make claims on the ultimate sensitivity of LIDAR systems using coherent control.

This research is the synthesis of two general fields: coherent quantum control and LIDAR. The most important (to this line of research) fundamental relationships from each field were derived in this chapter. The effect of the thermal velocities associated with gas samples, in fact, played an important role in both areas: in terms of coherent control, the velocity gives us a general equation of motion for laser excited gas molecules; additionally, this velocity distribution is shown to have a significant impact on the observed behavior of these molecules in bench top scale demonstrations.

The molecular orientation distribution is shown to have a “damping” effect on the dynamics. The best one can hope for (assuming the worst case scenario – i.e. the classical case) is a little more than 60% population inversion. For higher pulse energies (or equivalently longer pulse lengths) the ensemble quickly loses coherence and the population of the ground and excited states balance at 50%/50%. The velocity distribution is shown

to lower the oscillation frequency. In addition, it reduces the maximum inversion and shifts the high energy/long pulse balance from 50%/50% toward the ground state. The velocity distribution also has a “damping” effect when one considers finite laser spot sizes and the finite acceptance space of the detection device. For our monochromator, it is found that spot sizes near 1 mm will avoid this effect.

The analysis of the backscattered LIDAR geometry led to encouraging results. First we see that the number of molecules to which the system is sensitive increases with range. This interesting result is tempered by the fact that the energy required increases at the same rate. At the moment, it seems unrealistic to expect more than 1 J per ns pulse. This limits the range of a reasonable LIDAR system using a 1 m aperture to about 1 km. The number of atmospheric molecules to which this system would be sensitive is around 10^{13} . It is important to note that these calculations used our estimate for the matrix element, M , of the iodine molecule. The LIDAR “efficiency” ratio (Equation 2.2.13) depends on M^2 (the matrix element squared) and thus the range limits may change significantly for molecules with larger M ’s.

Chapter 3

Population Transfer Simulations

In this chapter, the basic equations of motion for multi-color population transfer are explored using a numerical integrator. Specific computer model parameters are calculated such that well known efficient multi-color pulse schemes can be simulated. To analyze robustness of various coherent processes with respect to amplitude fluctuations in the laser source, three different three-color pulse schemes are compared in a stochastic simulation. Because our target molecular system is relatively uncontrolled (trace molecular species in the atmosphere), we must consider the interaction between the target species and the environment (such systems are called “open” quantum systems [14]). The de-coherence effect of collisions is studied using a simple model and the resulting motion is fit to a phenomenologically derived equation of motion using density matrix techniques in Liouville space.

The “open” nature of the problem is treated in an extremely simplified fashion. The target levels (four levels in the case of three-color excitation) are assumed to be the only states that will produce observable effects. It is known that in molecular systems, one typically must deal with a *dense* energy level structure. To model an actual application more accurately, one must include some of the nearby energy levels in the observable system.

The only pulse schemes analyzed here are of the recently demonstrated STIRAP type (and, of course, the Gaussian π -pulse). With respect to the general detection problem at hand, there may be other pulse schemes with similar or better characteristics. For example, pulses with a temporal “comb” structure may be able to take advantage of the “quantum zeno” effect [42].

See reference [83] for a basic review of laser-induced adiabatic population transfer techniques. Reference [78] reports the results of a numerical determination of the pulse parameters for STIRAP type population transfer using multi-color pulse trains. In this work,

we re-calculate the results for two and three-color pulse trains. We extend the study of these pulse schemes by exploring the pulse amplitude solution space near the two-color optimum and comparing the different schemes when subject to randomized pulse amplitudes.

Reference [76] suggests a model for the quantum dynamical effects of collisions. This model is stochastically applied to a resonant three-color excitation of a four level system using a computer program. To model the resulting “relaxation” from the stochastic model, we use density matrix techniques [24, 69, 45]. A relaxation matrix is written down, inspired by techniques reported in references [8] and [44] but generated phenomenologically, and fit to the average behavior of the stochastic model.

3.1 Transform limited pulse sequences

3.1.1 One color

Suppose the dynamics of some two level quantum system is given by

$$i \frac{\partial}{\partial t} |\Psi\rangle = i \begin{pmatrix} 0 & \alpha \\ -\alpha & 0 \end{pmatrix} |\Psi\rangle, \quad (3.1.1)$$

where the square of the nth element in $|\Psi\rangle$ is the probability of finding the system in the nth state, α is the coupling field between the zeroth (ground) and first excited state. It can be shown (see Section 2.1.2) that closed non-degenerate two level quantum systems with a completely resonant coupling field can be described this way in the energy basis (see Figure 3.1). In general the coupling field is a function of time. Consider solutions where

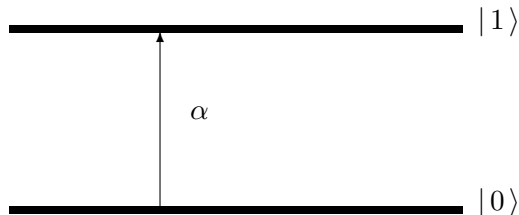


Figure 3.1: Two level, single field diagram. Ground state $|0\rangle$ and first excited state $|1\rangle$ are coupled by field α so that population transfers from the ground state to the first excited state

the coupling field is localized temporally as a Gaussian, namely

$$\alpha(t) = A \exp\left(-\ln(16)\frac{(t - t_\alpha)^2}{\sigma_\alpha^2}\right), \quad (3.1.2)$$

where A is the amplitude, t_α is location of the pulse, σ_α is the full width half max (FWHM) of the pulse amplitude.

Given an arbitrary pulse width of $\sigma_\alpha = 2$, we seek to find the pulse height A that corresponds to a complete inversion (ground state completely depleted). Suppose the solution, $|\Psi\rangle$, to (3.1.1) is known. Consider the cost function

$$\Phi = P_0(t = t_{final}) \quad (3.1.3)$$

where P_0 be the probability that the system is found in the ground state (i.e. $\langle 0|0 \rangle$); thus, if $P_0 = 0$ then the two level system is completely inverted. A MathCAD program is used to minimize (3.1.3) as a function of A for a system initially in the ground state over the time interval $[0, 30]$ (thus Equation 3.1.3 is evaluated at $t = 30$). A fourth-order Runge-Kutta fixed-step method is used to find the solution at 5000 points in the time interval. The MathCAD function “Minimize” is used to find the optimal solution. The “Minimize” function tries the conjugate gradient, quasi-Newton, and Levenberg-Marquardt methods in succession until one converges.

Figure 3.2 shows the pulse and resulting motion in $\langle \Phi | \Phi \rangle$ at a local optimum. There are many local optima as one increases A . The nature of these repeated optima becomes obvious when one considers the analytic solution (they are successive Rabi oscillations), Equation 2.1.20; in lieu of such a discussion we present an example (see figure 3.3).

3.1.2 Two color

Suppose the dynamics of some three level quantum system is given by

$$i \frac{\partial}{\partial t} |\Psi\rangle = i \begin{pmatrix} 0 & \alpha & 0 \\ -\alpha & 0 & \beta \\ 0 & -\beta & 0 \end{pmatrix} |\Psi\rangle, \quad (3.1.4)$$

where the square of the nth element in $|\Psi\rangle$ is the probability of finding the system in the nth state, α is the coupling field between the zeroth (ground) and first state and β is the coupling field between the first and second state. Using the same methods as in Section

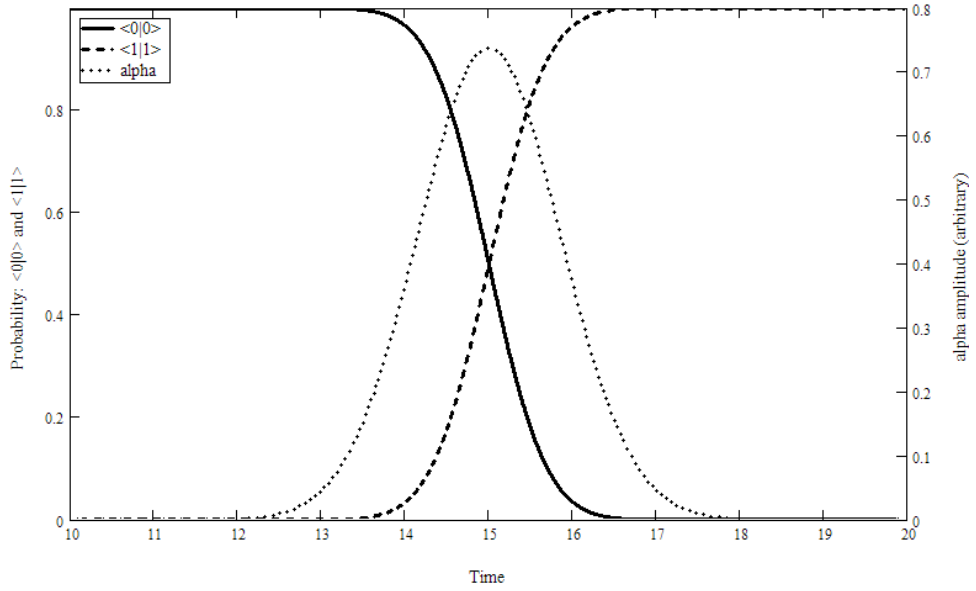


Figure 3.2: Single color optimal solution. With $\sigma_\alpha \equiv 2$, this local optimum occurs when $A = 0.737832313319$. Many more local optima occur with increasing A . If the pulse area is ξ , then $\xi - \pi/2 \sim 10^{-12}$ (the precision of A). In the literature, this is called a π -pulse.

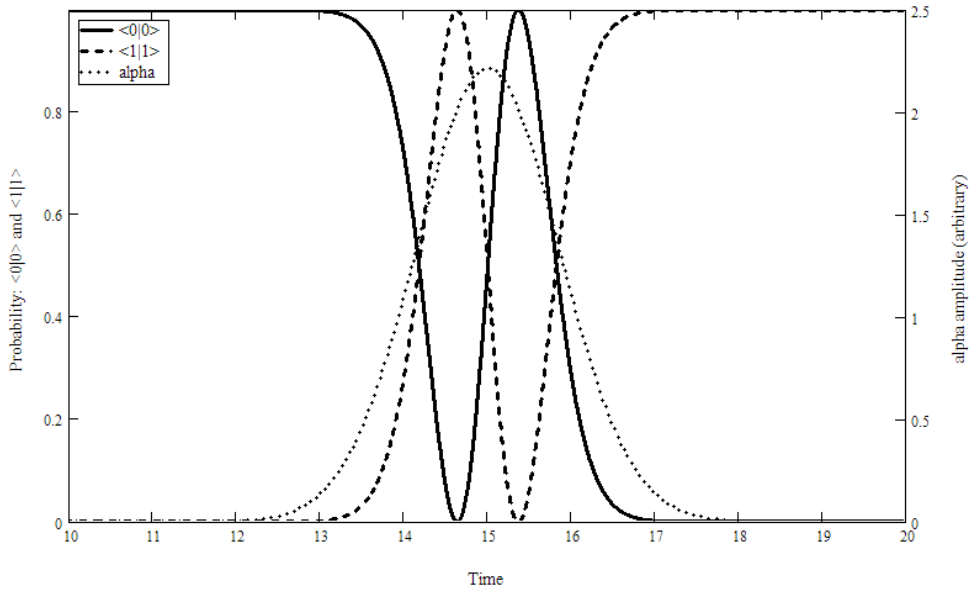


Figure 3.3: Single color optimal solution - increased pulse amplitude. This local optimum occurs when $A = 3 \times 0.737832313319$ (three times the area of the π -pulse).

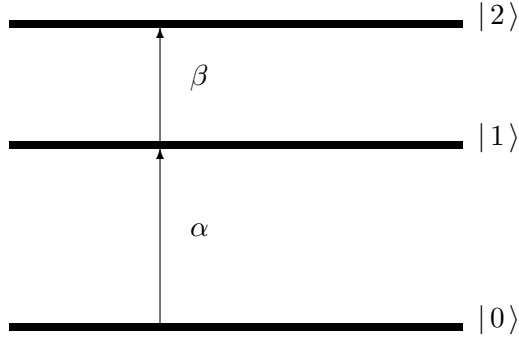


Figure 3.4: Three level, two field diagram. Ground state $|0\rangle$, first excited state $|1\rangle$, and second excited state $|2\rangle$ are coupled by fields α and β so that population transfers from the ground state to the second excited state

2.1.2, it can be shown that closed non-degenerate three level quantum systems with two completely resonant “ladder” coupling fields can be described this way in the energy basis (see Figure 3.4). Again, we consider temporally localized coupling fields of the form given in equation (4.11) for α and similarly for β . Let the position of α be given in terms of β ’s position; namely let Δ_α be the temporal distance alpha *leads* beta; specifically

$$t_\alpha = t_0 - \frac{\Delta_\alpha}{2} \quad (3.1.5a)$$

$$t_\beta = t_0 + \frac{\Delta_\alpha}{2} \quad (3.1.5b)$$

where t_0 is the center of the pulse sequence. For example, in the sequential order shown in Figure 3.5, Δ_α is positive. Suppose the solution, $|\Psi\rangle$, to (3.1.1) is known at $N+1$ points from t_0 to t_N where $t_i < t_j$ when $i < j \forall i, j \in \{0, 1, \dots, N\}$. Let $|n\rangle_i$ be the value of the n th component ($n \in \{0, 1, 2\}$) of the solution, $|\Psi\rangle$, at time t_i . Consider the cost function

$$\Phi = w\Phi_{residue} + \Phi_{intermediate} \quad (3.1.6)$$

where

$$\Phi_{residue} = P_0(t_N) + P_1(t_N). \quad (3.1.7)$$

$$\Phi_{intermediate} = \sum_i^N P_1(t_i). \quad (3.1.8)$$

and w is some weight factor. A MathCAD program is used to minimize (3.1.6) as a function of σ_α (or σ_β), A , B , and Δ_α for a system initially in the ground state over the time interval $[0, 30]$ ($t_0 = 15$). A fourth-order Runge-Kutta fixed-step method is used to find the solution

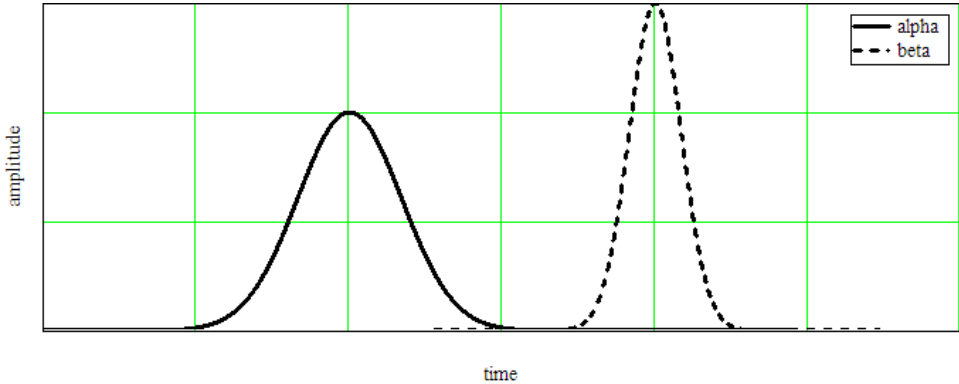


Figure 3.5: Two pulse sequence example. In general the pulses α and β have arbitrary widths σ_α and σ_β as well as arbitrary amplitudes A and B . Here Δ_α is positive since α precedes β .

at 5000 points in the time interval. The MathCAD function “Minimize” is used to find the optimal solution.

After some initial runs, some symmetries in the solutions prompted the following reduction of variables: $\sigma_\alpha = \sigma_\beta = 2$ and $A = B$; thus, the solution space is two dimensional, namely Δ_α and A . Figure 3.6 shows the pulse sequence which minimized the cost function and figure 3.7 show the resulting motion in $\langle \Psi | \Psi \rangle$. In fact, a family of local optima exist. These optima improve, in general, as pulse amplitude increases. Figure 3.8 shows an example of an optimum where the pulses used have nearly twice the amplitude as the pulses shown in figure 3.6.

The pulse sequence in Figure 3.6 is called the STIRAP pulse sequence in the literature [78]. Its interesting properties include a “counter-intuitive” pulse sequence and the near zero population of the intermediate state during the entire process while the ground and upper state undergo inversion. One would expect the pulse taking the probability up the ladder from the ground state to the first excited state should go first. In Figure 3.6 we see that the pulse sequence is reversed (hence the term “counter-intuitive”); however, notice that there is significant overlap.

For the optimal solution, $\Phi_{residue} = 9 \times 10^{-15}$, we map out the surface this variable defines in solution space using two coordinate systems. The region in solution space near the optimal solution shown in Figure 3.6 was mapped out by allowing the magnitude of Δ_α and A to vary by $\pm 50\%$. Figure 3.9 shows the resulting $\log(\Psi_{residue})$ surface. The region in solution space near the optimal solution shown in Figure 3.6 was mapped out by allowing

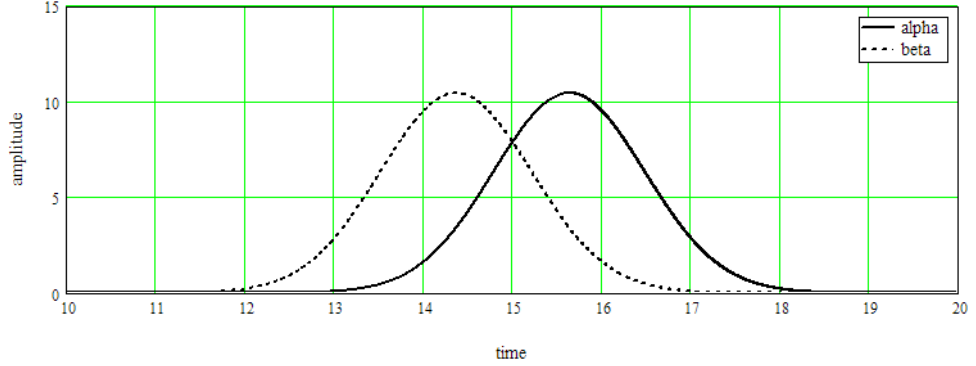


Figure 3.6: Two color optimal pulse sequence (STIRAP). With $\sigma_\alpha = \sigma_\beta \equiv 2$, the optimization program produced $\Delta_\alpha = -1.26997923288$ and $A = 10.4616402919$ (14.179 times the area of the π -pulse) while w was set to 10^8 . Note that although $\Delta_\alpha < 0$, reflecting the fact that β precedes α , the pulses significantly overlap.

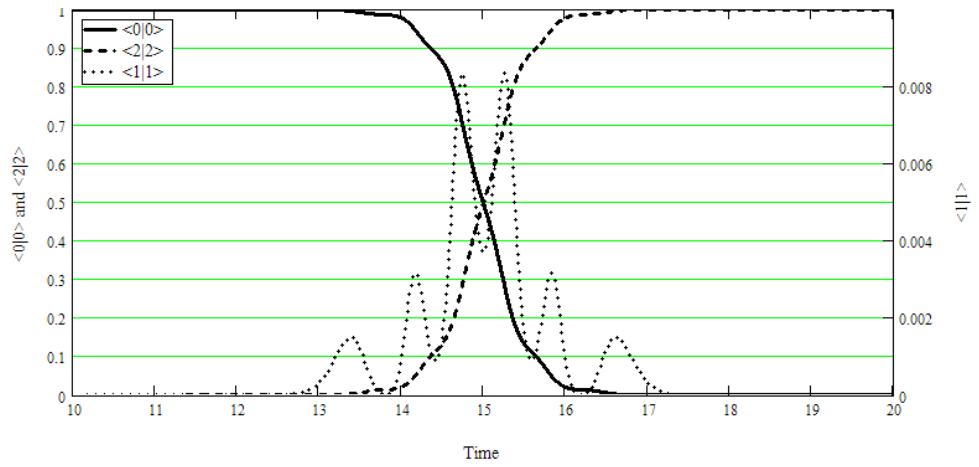


Figure 3.7: Two color optimal solution. $\langle \Psi | \Psi \rangle$'s behavior at the optimum using the pulse sequence from Figure 3.6. Note that $\langle 0|0 \rangle$ and $\langle 2|2 \rangle$ are shown at a different scale than $\langle 1|1 \rangle$. This solution effectively transfers population directly from the ground state to the second excited state without significantly populating the first excited state.

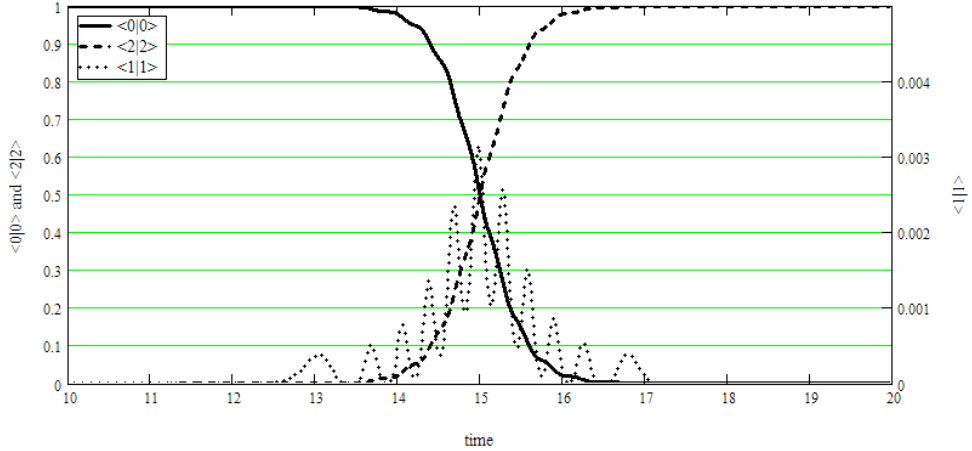


Figure 3.8: Two color optimal solution - increased pulse amplitude. $\langle \Psi | \Psi \rangle$'s behavior at an optimum with increased pulse amplitudes. Note that $\langle 0 | 0 \rangle$ and $\langle 2 | 2 \rangle$ are shown at a different scale than $\langle 1 | 1 \rangle$. Notice the decrease in the average height of $\langle 1 | 1 \rangle$ when compared to $\langle 1 | 1 \rangle$ in figure 3.7. For this solution $\Delta_\alpha = -1.3146820926$ and $A = 19.5606505329$ (26.511 times the area of the π -pulse).

the magnitude of A and B to vary by $\pm 50\%$. Figure 3.10 shows the resulting $\log(\Psi_{residue})$ surface. Figures 3.9 and 3.10 show the robustness of the STIRAP process with regards to population transfer. Since the residue is less than 10^{-2} for most of the points (i.e. there is very little population left over in states 0 and 1) population transfer is nearly complete for relatively large detuning of certain pulse parameters (amplitude and delay). This means that even if there are fluctuations in these parameters, the targeted two color pathway will still result in nearly complete population transfer; thus the probability that the final target state releases a fluorescence photon is nearly independent of these types of fluctuations.

3.1.3 Three color

Suppose the dynamics of some four level quantum system is given by

$$i \frac{\partial}{\partial t} |\Psi\rangle = i \begin{pmatrix} 0 & \alpha & 0 & 0 \\ -\alpha & 0 & \beta & 0 \\ 0 & -\beta & 0 & \gamma \\ 0 & 0 & -\gamma & 0 \end{pmatrix} |\Psi\rangle, \quad (3.1.9)$$

where the square of the nth element in Ψ is the probability of finding the system in the nth state, α is the coupling field between the zeroth (ground) and first state, β is the coupling field between the first and second state, and γ is the coupling field between the second and

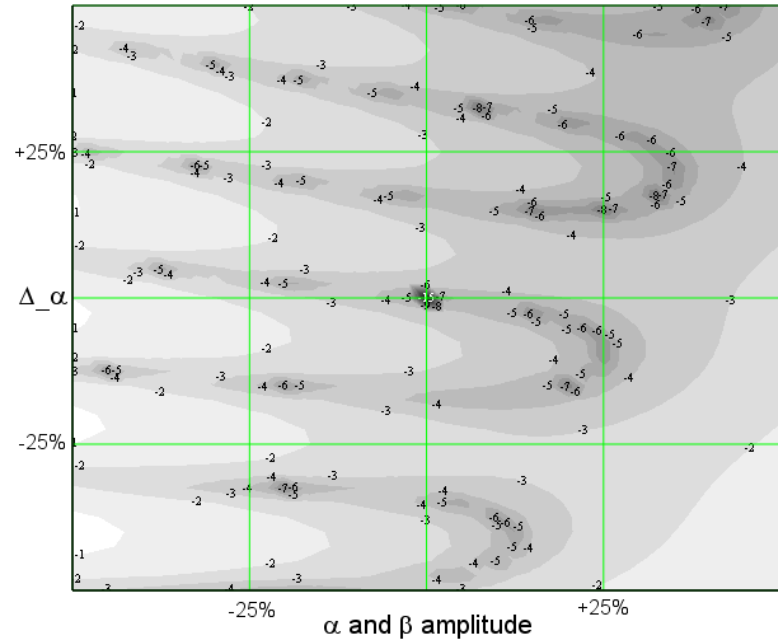


Figure 3.9: $\log(\Phi_{\text{residue}})$ dependence on scaling Δ_α and A . There are many local optima arranged in a repeating crescent shape. In general the local optima and the average height of the nearby surface decreases as Δ_α and A increase. There are 41^2 evenly spaced points here.

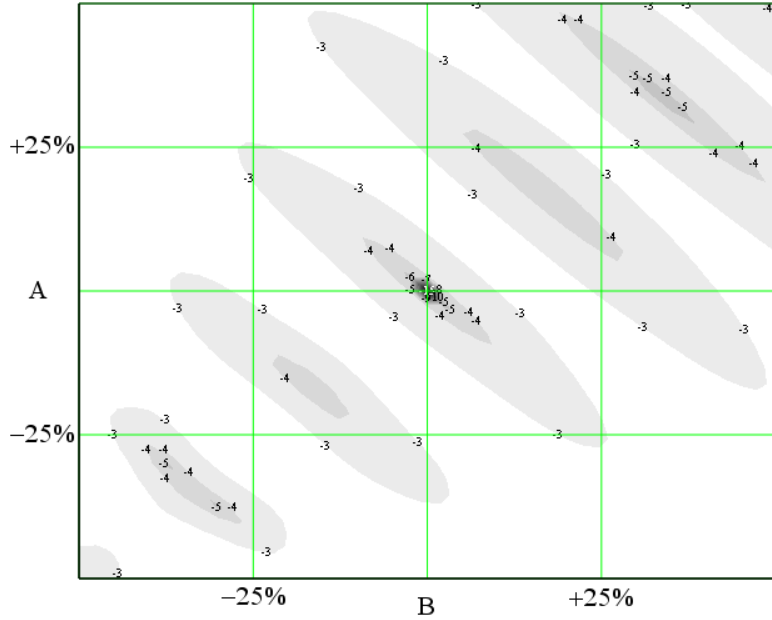


Figure 3.10: $\Phi_{residue}$ dependence on scaling A and B . There are many local optima along the line defined by $A = B$. These optima improve as amplitudes A and B increase; and, in general, the surface slopes down as A and B increase. There are 41^2 evenly spaced points here.

third state. Using the same methods as in Section 2.1.2, it can be shown that closed non-degenerate four level quantum systems with three completely resonant “ladder” coupling fields can be described this way in the energy basis (see figure 3.11). Again we consider temporally localized coupling fields of the form (4.11). Let the positions of α and γ be given in terms of β ’s position; namely let Δ_α be the temporal distance alpha *leads* beta and Δ_γ be the temporal distance gamma *lags* beta; specifically

$$t_\alpha = t_0 - \Delta_\alpha \quad (3.1.10a)$$

$$t_\beta = t_0 \quad (3.1.10b)$$

$$t_\gamma = t_0 + \Delta_\gamma \quad (3.1.10c)$$

where t_0 is the middle of the pulse sequence (and the position of β). Thus, for a sequential order as shown in Figure 3.12, both Δ_α and Δ_γ are positive. Suppose the solution, $|\Psi\rangle$, to (3.1.1) is known at $N+1$ points from t_0 to t_N where $t_i < t_j$ when $i < j \forall i, j \in \{0, 1, \dots, N\}$. Let $|n\rangle_i$ be the value of the n th component ($n \in \{0, 1, 2, 3\}$) of the solution, $|\Psi\rangle$, at time t_i . Consider the cost function

$$\Phi = w\Phi_{residue} + \Phi_{intermediate} \quad (3.1.11)$$

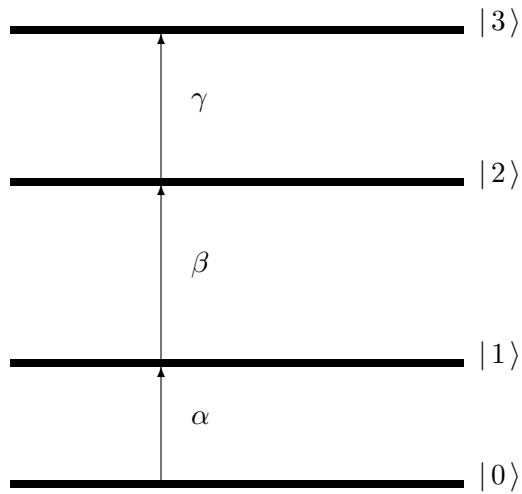


Figure 3.11: Four level, three field diagram. Ground state $|0\rangle$, first excited state $|1\rangle$, second excited state $|2\rangle$ and third excited state $|3\rangle$ are coupled by fields α , β , and γ so that population transfers from the ground state to the third excited state

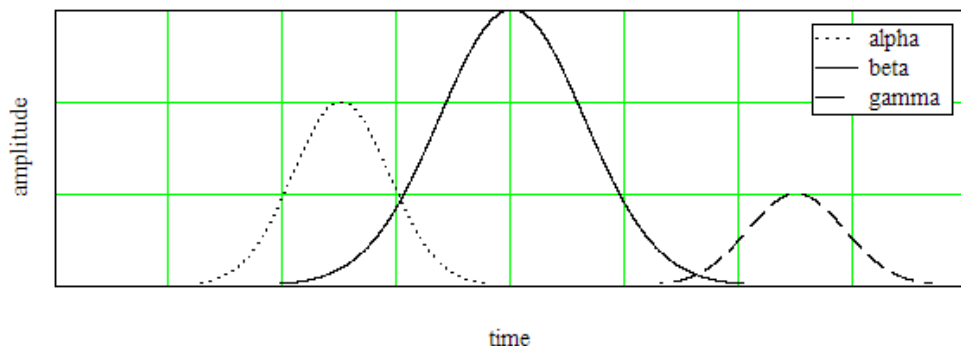


Figure 3.12: Three pulse sequence example. In general the pulses α , β , and γ have arbitrary widths σ_α , σ_β , and σ_γ as well as arbitrary amplitudes A , B , and C .

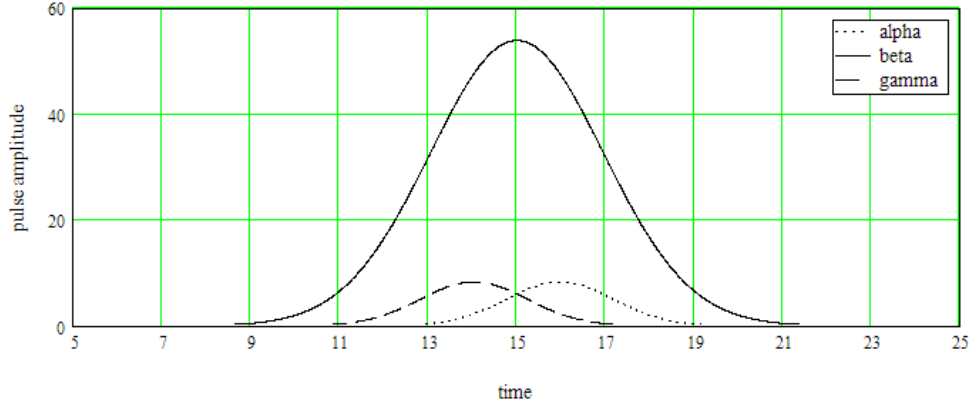


Figure 3.13: Three color optimal pulse sequence. When $w = 10^8$, the local optimum occurs when $\sigma_\alpha = \sigma_\gamma = 2.84885872022$, $\sigma_\beta = 4.59093152823$, $A = C = 8.28793940926$ (5.093 times the area of the π -pulse), $B = 53.8858080585$ (53.363 times the area of the π -pulse), and $\Delta_\alpha = \Delta_\gamma = -0.972655687674$.

where

$$\Phi_{residue} = P_0(t_N) + P_1(t_N) + P_2(t_N) \quad (3.1.12)$$

$$\Phi_{intermediate} = \sum_i^N P_1(t_i) + P_2(t_i) \quad (3.1.13)$$

and w is some weight factor. A MathCAD program was written to minimize (3.1.11) as a function of σ_α , σ_β , σ_γ , A , B , C , Δ_α and Δ_γ . After some initial runs, some symmetries in the solutions prompted the following reduction of variables: $\sigma_\alpha = \sigma_\gamma$, $A = C$, $\Delta_\alpha = \Delta_\gamma$. Figure 3.13 shows the pulse sequence which minimized the cost function and figure 3.14 shows the resulting motion in $\langle \Psi | \Psi \rangle$.

In general, there are many local optima in the five dimensional solution space. It was found (with some exploring) that these optima generally improve with increasing amplitudes A , B , and C . Figure 3.15 show an example of one such solution. Note again the “counter-intuitive” pulse order of the first and last pulse.

3.2 Random excitation amplitude simulations

It was observed in the laboratory that the dye lasers, intended for use in a demonstration experiment of these processes, exhibit relatively large ($\sim 20\%$) intensity fluctuations. Here we estimate the effect of these fluctuations on the population transfer efficiency of various three color transfer schemes.

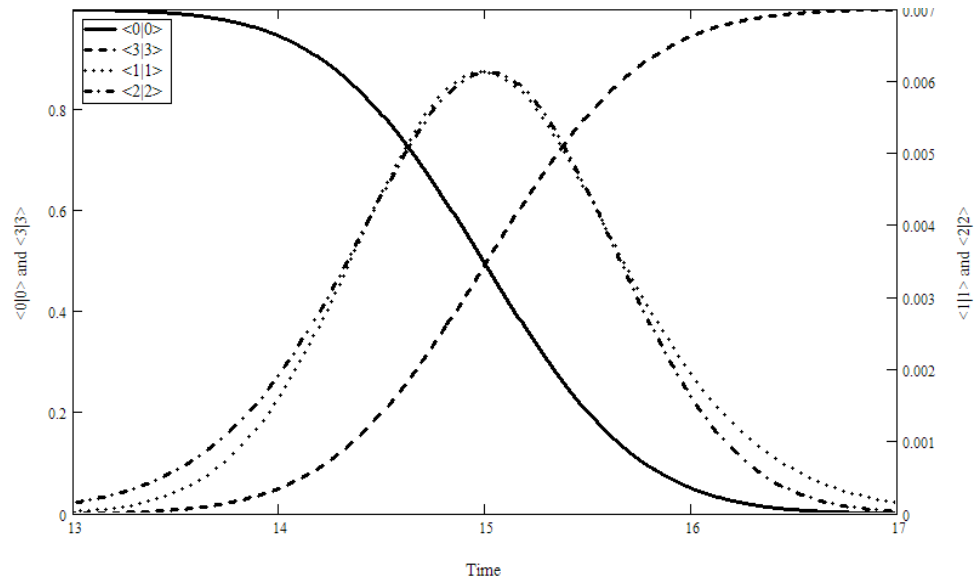


Figure 3.14: Three color optimal solution. Occupation probability of the intermediate states $|1\rangle$ and $|2\rangle$ remain small while states $|0\rangle$ and $|3\rangle$ essentially exchange unity occupation probability in what looks like a single color π -pulse process (see figure 3.2).

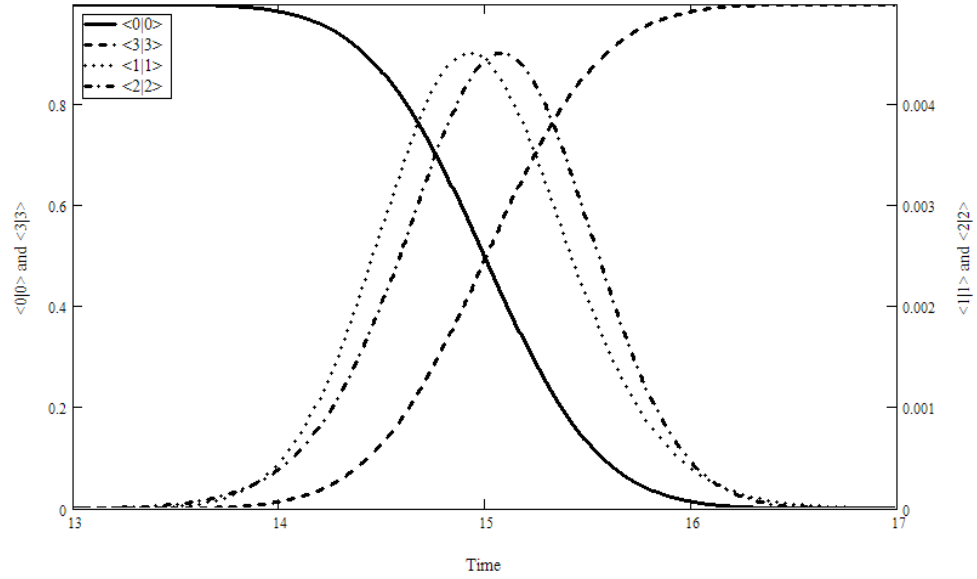


Figure 3.15: Three color optimal solution - increased pulse amplitude. The local optimum ($w = 10^8$) occurs when $\sigma_\alpha = \sigma_\gamma = 2.19612383897$, $\sigma_\beta = 4.57812933276$, $A = C = 15.8819988348$ (7.524 times the area of the π -pulse), $B = 101.198555496$ (99.937 times the area of the π -pulse), and $\Delta_\alpha = \Delta_\gamma = -0.93886228288$.

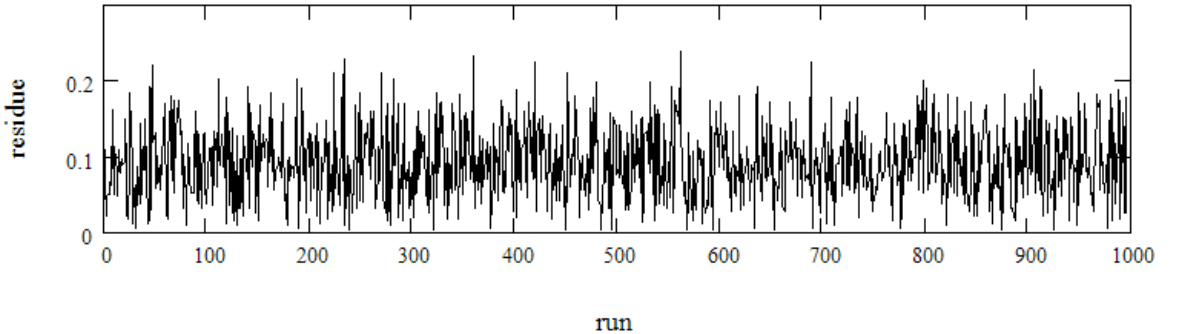


Figure 3.16: Residue for runs using three π pulses. Three pulses of the form shown in figure 3.2 were used at $t_\alpha = 5$, $t_\beta = 15$, and $t_\gamma = 25$. The pulse amplitudes A , B , and C varied uniformly on the interval $[-20\%, +20\%]$ for 1000 runs.

3.2.1 Three π pulse sequence

We examine a three π pulse sequence. Each pulse has the temporal profile (4.11) with $\sigma_\alpha = \sigma_\beta = \sigma_\gamma = 2$ and $A = B = C = 0.737832313319$. The centers of each pulse were placed symmetrically in the interval $[0, 30]$: $t_\alpha = 5$, $t_\beta = 15$, and $t_\gamma = 25$. For each run the amplitudes are selected in a uniform random fashion on the interval $[-20\%, +20\%]$ using the “runif” random number generator in MathCAD. Then a fourth-order Runge-Kutta fixed-step method is used to find the solution at 5001 points in the interval, and hence the residue ($\Psi_{residue}$) for each run. See figure 3.16.

3.2.2 STIRAP sequence followed by a π pulse

We examine a STIRAP sequence followed by pi pulse. The first two pulses are a STIRAP sequence with $t_\beta = 10$, $t_\alpha = t_\beta - \Delta_\alpha = 10 + 1.26997923288$ and $A = B = 10.4616402919$. The last pulse is a π pulse with $\sigma_\gamma = 2$, $t_\gamma = 25$, and $C = 0.737832313319$. For each run the amplitudes are selected in a uniform random fashion on the interval $[-20\%, +20\%]$ using the “runif” random number generator in MathCAD. Then a fourth-order Runge-Kutta fixed-step method is used to find the solution at 5001 points in the interval, and hence the residue ($\Psi_{residue}$) for each run. See figure 3.17.

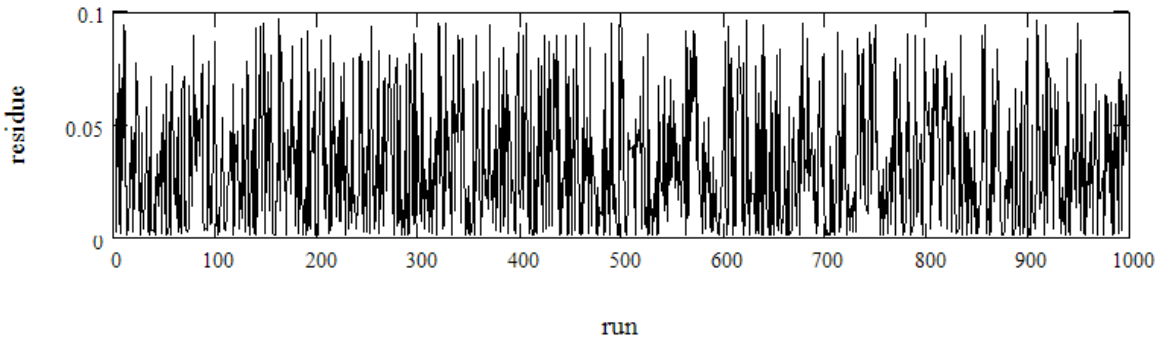


Figure 3.17: Residue for runs using the STIRAP sequence followed by a π pulse. This pulse sequence consists of a STIRAP sequence of the form shown in figure 3.6 followed by a pi pulse of the form shown in figure 3.2. The pulse amplitudes A , B , and C varied uniformly on the interval $[-20\%, +20\%]$ for 1000 runs.

3.2.3 Three color optimal sequence

We examine a three color optimal solution. For each run, a pulse sequence of the form shown in figure 3.13 is used where the amplitudes are selected in a uniform random fashion on the interval $[-20\%, +20\%]$ using the “runif” random number generator in MathCAD. Then a fourth-order Runge-Kutta fixed-step method is used to find the solution at 5001 points in the interval, and hence the residue ($\Psi_{residue}$) for each run. See figure 3.18.

3.2.4 Histogram comparison

We use a histogram to compare the three different three pulse sequences. The runs shown in figures 3.16, 3.17, and 3.18 were sorted in 0.01 wide bins. In Figure 3.19 we see that the two coherent processes (STIRAP + π and three color STIRAP) tend to result in nearly complete population transfer, while the sequential π pulse scheme tends to leave about 10% of the population in the lower levels. Thus, the STIRAP processes may not be negatively effected by the power fluctuations in the dye laser output.

3.3 Stochastic collision model and density matrix methods

First, we examine the effect of collision using a “state vector” approach assuming that the effect of collisions is to simply randomize the “phase” of the atom. Then we try to merge this idea with density matrix methods using a computer fit to the free parameters in a

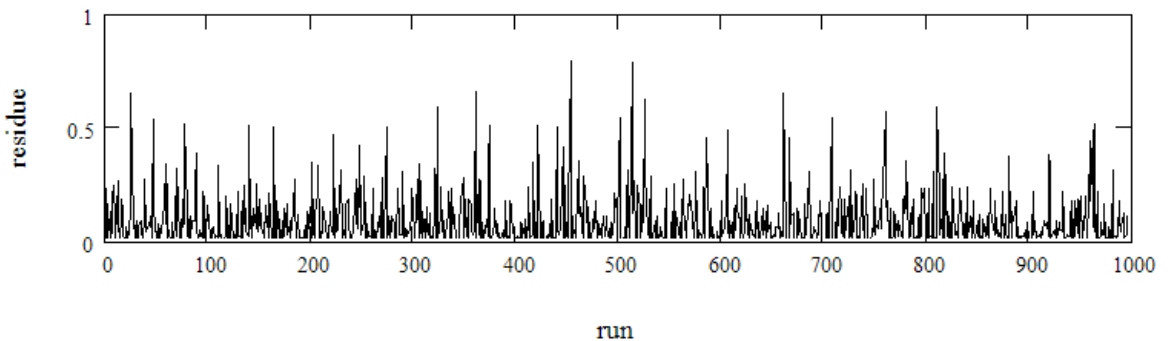


Figure 3.18: Residue for runs using three color STIRAP. A pulse sequence of the form show in figure 3.13 is used here. The pulse amplitudes A , B , and C varied uniformly on the interval $[-20\%, +20\%]$ for 1000 runs.

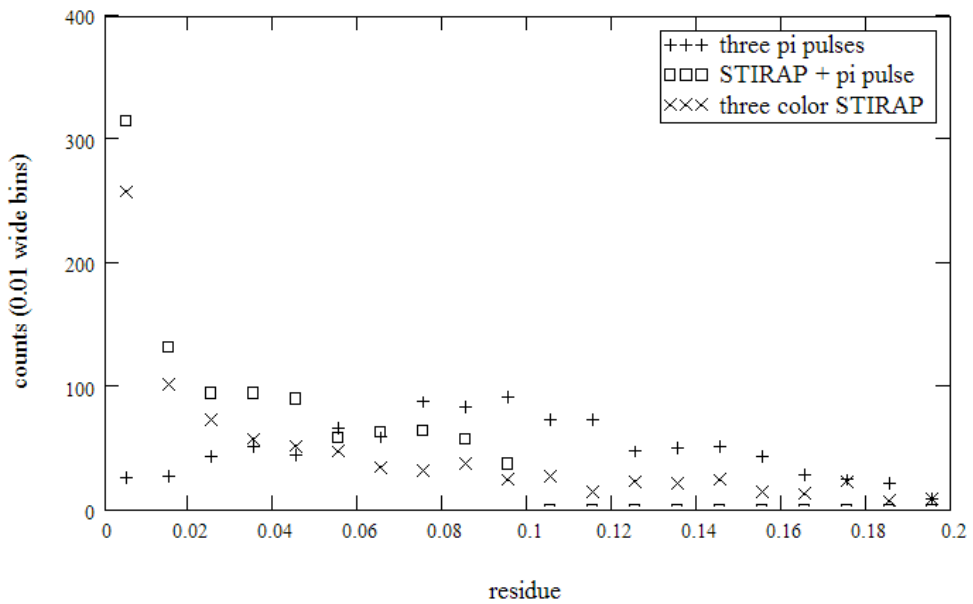


Figure 3.19: Stochastic simulation histograms. Notice that the three π pulse sequence has a peak somewhere near 0.1 while the other two sequences seem peaked near zero.

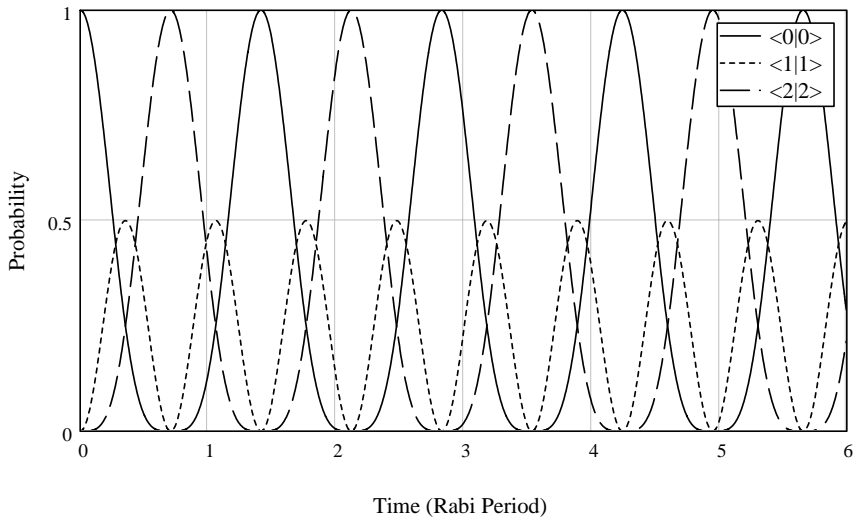


Figure 3.20: Collisionless evolution of a three state system. For this (and the following simulations) $\alpha = \beta = 1$ and the time scale is the two state Rabi period associated with α (or β).

“relaxation” matrix. Modeling the effects of collisions in a stochastic manner (as in Section 3.3.1 is computationally intensive and slow. The density matrix method is computational simple and would be preferred for further investigation into collisional effects.

3.3.1 Collision model

Reference [76] describes a model for the collisional effects on the quantum mechanical evolution of an atomic system. The main effect of collisions is to randomize the phase of the expansion coefficients (i.e. the “c’s” in Equations 2.1.8 and 2.1.9) as they evolve. (Collisions may also transfer population with relatively low probability in inelastic collisions, but this is ignored in this analysis.) This model is easy to implement in computer code written to solve Equation 2.1.9. As the code solves the equation, it is interrupted randomly. The phase of the expansion coefficients (the expansion coefficients are in general complex) are uniformly randomized on the interval $[0, 2\pi]$ while leaving the magnitude intact. Then the numerical integrator picks up where it left off at the interruption, except with the new “randomized” expansion coefficients and continues until another “collision” (i.e. interruption) takes place. See Figures 3.20 through 3.22 for examples.

The probability of a collision per unit time is arbitrarily selected as $0.5/\pi$ in the examples shown here (there were additional runs at $0.3/\pi$). In Figure 3.23 we see the result when one million runs are averaged together: the behavior has the appearance of damped

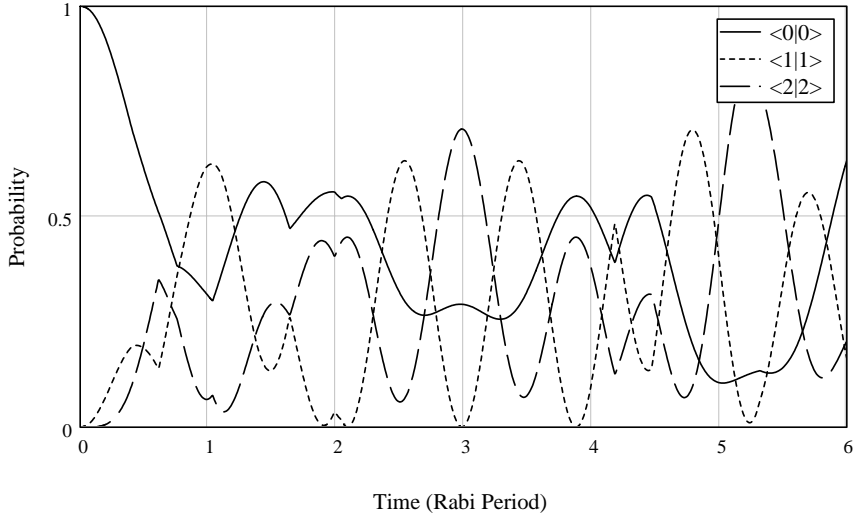


Figure 3.21: Evolution of a three state system with collisions - example 1. The probability of a collision per Rabi period is $0.5/\pi$.

oscillations. This behavior seems like it may be described in a cleaner way; if not with an analytic form, then with a differential equation. In the next section we develop a formal candidate.

3.3.2 Density matrix formalism

The equation of motion for the density matrix is given by the Liouville-von Neumann equation:

$$i\hbar \frac{\partial \rho}{\partial t} = [H, \rho]; \quad (3.3.1)$$

where H is the Hamiltonian and ρ is the density matrix. If the system of interest is not totally isolated and the degrees of freedom due to its surroundings (the so called “heat bath”) are unobserved, then equation (3.3.1) may not describe the time evolution of the system [14]. In our application, we have a target molecule (system of interest) in a “sea” of non-target atmospheric molecules (the “bath”).

We introduce a *relaxation* operator \hat{R} [9] to parameterize the effect of the surroundings:

$$i \frac{\partial \rho}{\partial t} = [H, \rho] + i \hat{R} \vec{\rho}. \quad (3.3.2)$$

If we are working in n dimensional Hilbert space, the left hand side and the first two terms on the right hand side are $n \times n$ matrices. Since the last term is in Liouville space (i.e.

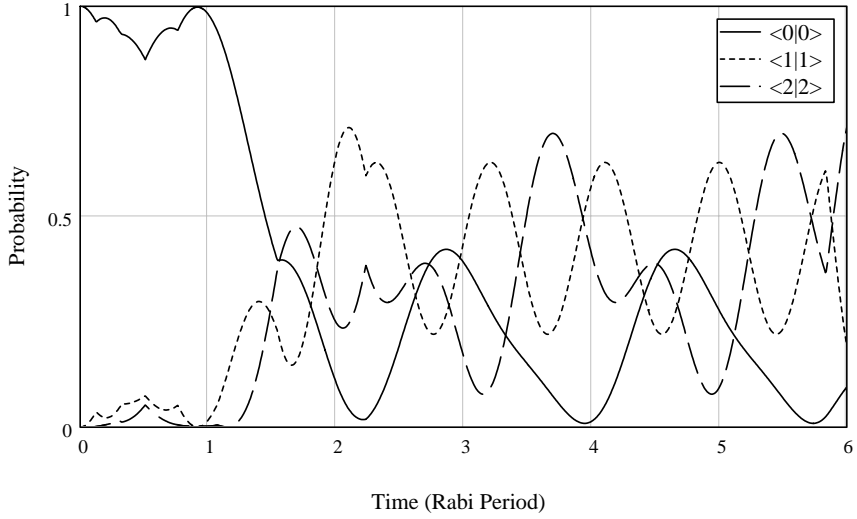


Figure 3.22: Evolution of a three state system with collisions - example 2. The probability of a collision per Rabi period is $0.5/\pi$.

$\vec{\rho} = (\rho_{00}, \dots, \rho_{nn})^T$ and \hat{R} is a $n^2 \times n^2$ matrix) there remains a one to one correspondence between the elements of each term in the equation of motion.

Let us consider the example of a many-level system (perhaps a target molecule with its many ro-vibrational levels) where we are only concerned with a small subset of these levels – specifically two levels (perhaps the two levels resonantly coupled with a tuned laser field). The Hamiltonian from Equation 3.1.4 is:

$$H = i \begin{pmatrix} 0 & \alpha \\ -\alpha & 0 \end{pmatrix}. \quad (3.3.3)$$

Next we give the relaxation matrix a specific form.

$$\hat{R} = \hat{R}^{ext} + \hat{R}^{int} + \hat{R}^{phase}; \quad (3.3.4)$$

where \hat{R}^{ext} represents the tendency of the two level subset to relax into the other levels outside the subset (external relaxation), \hat{R}^{int} represents the tendency of one level in the subset to relax into another level in the subset (internal relaxation), and \hat{R}^{phase} represents de-phasing resulting from the relaxation process mentioned above and/or from other sources (perhaps collisions).

$$\hat{R}^{ext} = \begin{pmatrix} -\Gamma_{00} & 0 & 0 & 0 \\ 0 & 0 & 0 & 0 \\ 0 & 0 & 0 & 0 \\ 0 & 0 & 0 & -\Gamma_{11} \end{pmatrix}, \quad (3.3.5)$$

$$\hat{R}^{int} = \begin{pmatrix} -\Gamma_1^0 & 0 & 0 & \Gamma_1^0 \\ 0 & 0 & 0 & 0 \\ 0 & 0 & 0 & 0 \\ \Gamma_0^1 & 0 & 0 & -\Gamma_0^1 \end{pmatrix}, \quad \text{and} \quad (3.3.6)$$

$$\hat{R}^{phase} = \begin{pmatrix} 0 & 0 & 0 & 0 \\ 0 & \gamma_{01} & 0 & 0 \\ 0 & 0 & \gamma_{01} & 0 \\ 0 & 0 & 0 & 0 \end{pmatrix}; \quad (3.3.7)$$

where Γ_{ii} is the relaxation rate of the state i to some external state, Γ_j^i is the relaxation rate of state i into state j , and γ_{ij} is the relaxation rate of ρ_{ij} ($i \neq j$). Γ_{ii} is the rate at state i relaxes to some other level *outside* the subset under consideration; hence if $\Gamma_{ii} \neq 0$ then probability will not be conserved in equation (3.3.2). γ_{ij} is applied to only the off diagonal terms in the density matrix; thus it is the rate at which the system loses coherence.

Now suppose our subsystem has three levels (see Figure 3.4). The Hamiltonian from Equation 3.1.9 is:

$$H = i \begin{pmatrix} 0 & \alpha & 0 \\ -\alpha & 0 & \beta \\ 0 & -\beta & 0 \end{pmatrix}. \quad (3.3.8)$$

Using the same definitions as in the two level case, we can write the relaxation matrix terms as

$$\hat{R}^{ext} = \begin{pmatrix} -\Gamma_{00} & 0 & 0 & 0 & 0 & 0 & 0 & 0 & 0 \\ 0 & 0 & 0 & 0 & 0 & 0 & 0 & 0 & 0 \\ 0 & 0 & 0 & 0 & 0 & 0 & 0 & 0 & 0 \\ 0 & 0 & 0 & 0 & 0 & 0 & 0 & 0 & 0 \\ 0 & 0 & 0 & 0 & -\Gamma_{11} & 0 & 0 & 0 & 0 \\ 0 & 0 & 0 & 0 & 0 & 0 & 0 & 0 & 0 \\ 0 & 0 & 0 & 0 & 0 & 0 & 0 & 0 & 0 \\ 0 & 0 & 0 & 0 & 0 & 0 & 0 & 0 & 0 \\ 0 & 0 & 0 & 0 & 0 & 0 & 0 & 0 & -\Gamma_{22} \end{pmatrix}, \quad (3.3.9)$$

$$\hat{R}^{int} = \begin{pmatrix} -\Gamma_1^0 - \Gamma_2^0 & 0 & 0 & 0 & \Gamma_1^0 & 0 & 0 & 0 & \Gamma_2^0 \\ 0 & 0 & 0 & 0 & 0 & 0 & 0 & 0 & 0 \\ 0 & 0 & 0 & 0 & 0 & 0 & 0 & 0 & 0 \\ 0 & 0 & 0 & 0 & 0 & 0 & 0 & 0 & 0 \\ \Gamma_0^1 & 0 & 0 & 0 & -\Gamma_0^1 - \Gamma_2^1 & 0 & 0 & 0 & \Gamma_2^1 \\ 0 & 0 & 0 & 0 & 0 & 0 & 0 & 0 & 0 \\ 0 & 0 & 0 & 0 & 0 & 0 & 0 & 0 & 0 \\ 0 & 0 & 0 & 0 & 0 & 0 & 0 & 0 & 0 \\ \Gamma_0^2 & 0 & 0 & 0 & \Gamma_1^2 & 0 & 0 & 0 & -\Gamma_0^2 - \Gamma_1^2 \end{pmatrix}, \quad (3.3.10)$$

and

$$\hat{R}^{phase} = \begin{pmatrix} 0 & 0 & 0 & 0 & 0 & 0 & 0 & 0 & 0 \\ 0 & \gamma_{01} & 0 & 0 & 0 & 0 & 0 & 0 & 0 \\ 0 & 0 & \gamma_{02} & 0 & 0 & 0 & 0 & 0 & 0 \\ 0 & 0 & 0 & \gamma_{01} & 0 & 0 & 0 & 0 & 0 \\ 0 & 0 & 0 & 0 & 0 & 0 & 0 & 0 & 0 \\ 0 & 0 & 0 & 0 & 0 & 0 & \gamma_{12} & 0 & 0 \\ 0 & 0 & 0 & 0 & 0 & 0 & 0 & \gamma_{02} & 0 \\ 0 & 0 & 0 & 0 & 0 & 0 & 0 & 0 & \gamma_{12} \\ 0 & 0 & 0 & 0 & 0 & 0 & 0 & 0 & 0 \end{pmatrix}. \quad (3.3.11)$$

3.3.3 Collision model parametric fit

The average behavior of the ensemble from Section 3.3.1 is modeled using the formalism from Section 3.3.2. Since the stochastic model conserves probability (the collision does not change the magnitude of the expansion coefficients) \hat{R}^{ext} is set to zero. If $\hat{R}^{int} = 0$ then a computer fit converges on the obvious solution quickly: namely the γ_{ij} 's in Equation 3.3.11 are all equal to the probability of a collision per unit time ($0.5/\pi$ in Figures 3.21, 3.22, and 3.23).

A more interesting check would be to see if we can distinguish between the two probability conserving terms in Equation 3.3.4 (\hat{R}^{int} and \hat{R}^{phase}) by only using the diagonals of the density matrix. The diagonal terms of the density matrix represent the probability of finding the system in a particular state – thus easily observable in an experiment. The number of free parameters in the fit is reduced (to keep the program run time less than a day) by assuming that probability only “leaks” down so that only Γ_0^2 , Γ_0^1 , and Γ_1^2 are non-

zero among the elements of \hat{R}^{int} . This is a reasonable assumption if spontaneous emission is the dominant relaxation process (other than collisions).

Now the density matrix reduces to six coupled differential equations:

$$\dot{\rho}_{00} = +\Gamma_0^1 \rho_{11} + \Gamma_0^2 \rho_{22} - \alpha(\rho_{01} + \rho_{10}) \quad (3.3.12a)$$

$$\dot{\rho}_{11} = -\Gamma_0^1 \rho_{11} + \Gamma_1^2 \rho_{22} + \alpha(\rho_{01} + \rho_{10}) - \beta(\rho_{21} + \rho_{12}) \quad (3.3.12b)$$

$$\dot{\rho}_{22} = -\Gamma_0^2 \rho_{22} - \Gamma_1^2 \rho_{22} + \beta(\rho_{12} + \rho_{21}) \quad (3.3.12c)$$

$$\dot{\rho}_{01} = -\gamma_{01} \rho_{01} + \alpha(\rho_{00} - \rho_{11}) - \beta \rho_{02} \quad (3.3.12d)$$

$$\dot{\rho}_{02} = -\gamma_{02} \rho_{02} + \beta \rho_{01} - \alpha \rho_{12} \quad (3.3.12e)$$

$$\dot{\rho}_{12} = -\gamma_{12} \rho_{12} + \alpha \rho_{02} + \beta(\rho_{11} - \rho_{22}) \quad (3.3.12f)$$

Clearly, the Γ 's should all be zero since the original model from Section 3.3.1 did not include any population transfer; however, for this “test” we will keep them and see if a computer fit can show the Γ 's to be zero using only the occupation probabilities. In an actual experiment, we may only have access to the occupation probabilities, so this situation is somewhat realistic.

To compare this model to the average ensemble behavior from Section 3.3.1 a cost function, based off of the diagonals of the density matrix, is defined:

$$\Theta(\Gamma_0^1, \Gamma_0^2, \Gamma_1^2, \gamma_{01}, \gamma_{02}, \gamma_{12}) \equiv \sum_{n,i} (P_i(t_n) - P'_i(t_n))^2 \quad (3.3.13)$$

where the sum is taken over the number of time points $n = 0, 1, \dots, 999$ and the number of states $i = 0, 1, 2$. This cost function will be large (small) if there is a large (small) difference between the dynamics from Section 3.3.1 and the density matrix dynamics; thus, we would like to minimize this cost function as a function of the gamma coefficients. The terms in the sum are

$$P_i \equiv c_i \cdot c_i^* \quad (3.3.14)$$

for the “state vector” approach (c_i is the expansion coefficient in the average ensemble behavior from Section 3.3.1) and

$$P'_i \equiv \rho_{ii} \quad (3.3.15)$$

for the “density matrix” approach from Section 3.3.2 where and ρ_{ii} is from Equation 3.3.12 (and thus a function of $\Gamma_0^1, \Gamma_0^2, \Gamma_1^2, \gamma_{01}, \gamma_{02}$, and γ_{12}).

Two simulations were run: one with the collision probability set to $0.5/\pi$ and one with the collision probability set to $0.3/\pi$. Figures 3.21 and 3.22 show individual runs that

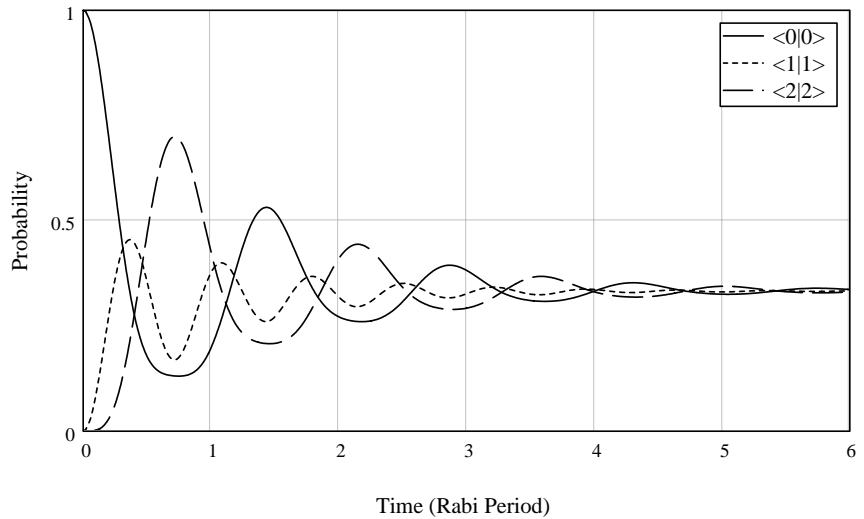


Figure 3.23: One million runs like those shown in Figure 3.21 and 3.22 are averaged to produce the plot shown above. The six parameter fit is so close that the difference is not perceptible at this scale.

are then averaged with many other runs to produce an approximation to ensemble behavior as shown in Figure 3.23. The “Simplex” parameter optimization method is used [62] to minimize the cost function, Equation 3.3.13, as a function of $\Gamma_0^1, \Gamma_0^2, \Gamma_1^2, \gamma_{01}, \gamma_{02}$, and γ_{12} . For a simulation where the collision probability set to $0.5/\pi$ we get

$$\Gamma_0^1 = 0.490795/\pi \quad (3.3.16a)$$

$$\Gamma_0^2 = 0.255223/\pi \quad (3.3.16b)$$

$$\Gamma_1^2 = 0.488124/\pi \quad (3.3.16c)$$

$$\gamma_{10} = 0.00183362/\pi \quad (3.3.16d)$$

$$\gamma_{02} = 0.315977/\pi \quad (3.3.16e)$$

$$\gamma_{12} = 3.72062 \times 10^{-5}/\pi, \quad (3.3.16f)$$

with $\Theta = 0.00648676$ (1000 points) and for a simulation where the collision probability set to $0.3/\pi$ we get

$$\Gamma_0^1 = 0.290149/\pi \quad (3.3.17a)$$

$$\Gamma_0^2 = 0.151391/\pi \quad (3.3.17b)$$

$$\Gamma_1^2 = 0.288282/\pi \quad (3.3.17c)$$

$$\gamma_{10} = 0.00650929/\pi \quad (3.3.17d)$$

$$\gamma_{02} = 0.173519/\pi \quad (3.3.17e)$$

$$\gamma_{12} = 0.00260537/\pi. \quad (3.3.17f)$$

with $\Theta = 0.00360311$ (1000 points).

The fact that the simulations fit the data very well is not that encouraging since the fit had six parameters. The results are characteristically nebulous with Γ_0^1 and Γ_1^2 apparently absorbing the effect while Γ_0^2 and γ_{02} seem to split responsibility in both simulations. It appears that internal probability damping (\hat{R}^{int}) may be indistinguishable from phase damping (\hat{R}^{phase}) when only observing state occupation probability in the collisional model. This could be further checked by running two different fits which depend only on \hat{R}^{int} or \hat{R}^{phase} and comparing the results and/or running a simulation with the pulse on for the first half and off for the second half. Once a method of assigning realistic magnitudes to the elements of these relaxation matrices is found, this formalism can be used to numerically explore the effects of relaxation on coherent control schemes.

3.4 Conclusion

This chapter covered two significant computer investigations into the dynamics of simple multi-level quantum systems under the action of pulsed control fields. These two studies proved important to the justification of this (coherent quantum control) approach to the LIDAR problem. Both of these studies are simple extensions of the basic formalism introduced in the previous chapter.

First, some novel quantum control processes were examined in terms that are important to a LIF type experiment. The two color process called STIRAP (and three color STIRAP like process) are analyzed for their robustness when faced with pulse sequences with randomly varying amplitudes. It is shown that there is an inherent insensitivity to

pulse amplitude fluctuations when the excitation pulses are beyond a certain threshold, with the two color STIRAP process being the most robust.

Second, a study of a simple collision model shows that there is a good chance that density matrix methods will be able to parameterize the relaxation effects in the dynamic model. This will facilitate computer exploration of open systems under quantum control. The hope (motivated, for example, by the quantum zeno effect [54]) is that we may discover special coherent processes which may be able to (selectively) control the temporal effects of relaxation.

Chapter 4

Molecular Laser Induced Fluorescence Simulations

In this chapter the iodine molecule is introduced, the iodine energy level system is described, two basic three color schemes are proposed, the perceived advantages are described (through computer simulation), and the rationale behind each scheme design is explained. The central idea is to selectively control a target molecule such that it fluoresces in a “dark” spectral region free from collateral noise induced by the excitation pulses. This technique is the spectral analog of the *temporal* “dark-field” detection method reported in reference [79].

We use the energy structure of the well studied molecular iodine system [51] as a numerical testing ground for some coherent population transfer methods. The beam requirements for coherent control are calculated, and the theoretical discrimination ratio of a proposed scheme is quantified. The recently demonstrated “STIRAP” process is introduced and its impact on the discrimination ratio is assessed.

The computer analysis is aided by making some simplifying assumptions. The exact Schrödinger dynamics are ignored; this allows approximate knowledge concerning the intricate and detailed molecular behavior to be gained using a modern desktop PC. The multi-color LIF process itself is under investigation here; no attempt is made to solve the traditional LIDAR problems. We do not investigate the effects of scattering, turbulence, absorption, etc.

The analysis described in this chapter relies heavily on references [39] and [27]; these resources give us detailed knowledge of the energy structure of molecular iodine and its isotopes though the use of a double power series expansion [22]. Reference [81] tabulates the

Frack–Condon Factor (FCF) for various transitions in molecular iodine. This information is combined here to provide a rough model of the dynamic response of molecular iodine to a three color coherent pulse train.

Efficient population transfer schemes were found experimentally [26] then explained theoretically [49]. Under names like “coherent population trapping” and “STIRAP” [66] these coherent process continued to be studied with analytic and computer techniques [17, 10, 46] and realized in molecular systems [68, 33]. In the following analysis, the impact of STIRAP on “orientation damping” (see Section 2.1.3) and the spatial distribution of inverted molecules are examined. The STIRAP detuning ridge is fit and its effect on isotope discrimination is modeled.

4.1 Molecular iodine

The iodine molecule has been extensively studied [55, 84, 81, 28, 27, 50, 52]; we seek to exploit this knowledge base in both our numerical studies and experimental efforts. In the visible region, the absorption spectrum of molecular iodine is dominated by transitions between the ground “X” electronic state and an upper excited electronic state called “B” [51]. Here we estimate the required beam parameters for coherent control and introduce the energy level structure.

4.1.1 Required (single color) beam properties to control iodine

Suppose the formalism from Section 2.1.1 applies to the molecular iodine system and that there exists a transition in the dominant X-B system [80] for which the condition stated in Equation 2.1.18 can be met. The following equation relates $\bar{\mu}_e(R)$ (the electronic contribution to M in the R centroid approximation) to M_{ab} (from Equation 2.1.13),

$$M_{ab} = \bar{\mu}_e(R) \langle \nu' | \nu'' \rangle \quad (4.1.1)$$

where $\bar{\mu}_e(R)$ is called the electronic transition moment and $\langle \nu' | \nu'' \rangle$ is called the Franck–Condon factor (FCF) [48, 89, 65].

Reference [50] reports the squared *electronic* dipole matrix element, $|\bar{\mu}_e(R_c)|^2 = |\bar{\mu}_e|^2$, for molecular iodine to vary from a maximum of $(2.00 \pm 0.11) \text{ D}^2$ (or $\bar{\mu}_e \sim 4.7 \times 10^{-28} \text{ Cm}$) to a minimum of $(8.7 \pm 4.6) \times 10^{-5} \text{ D}^2$ (or $\bar{\mu}_e \sim 5.7 \times 10^{-30} \text{ Cm}$) for $R_c = 2.66 \text{ \AA}$ and $R_c = 6.035 \text{ \AA}$ respectively ($D = 10^{-18} \text{ esu}$ and $1 \text{ Cm} = 2.99792458 \times 10^9 \text{ esu}$). Reference

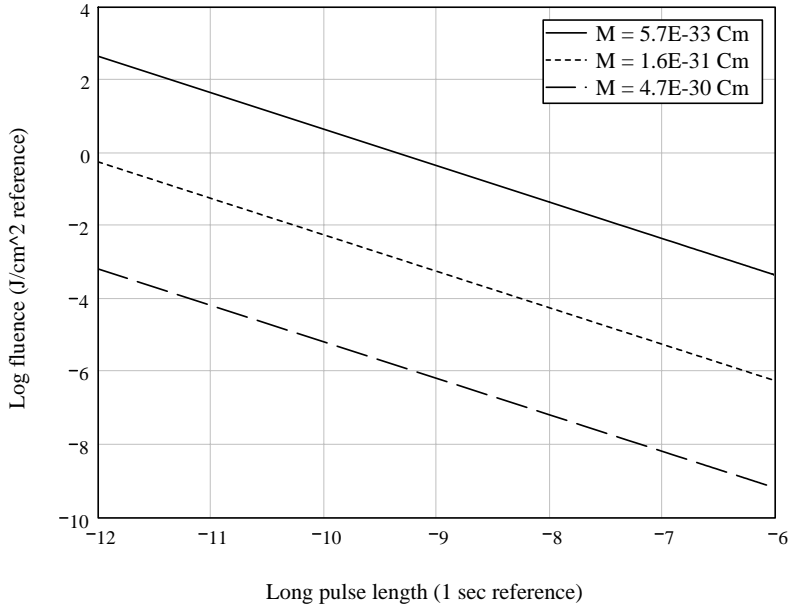


Figure 4.1: Required fluence for inversion of the two level iodine molecule. Here Equation 2.1.24 is plotted for various pulse lengths with $\Delta\tau = \pi/2$. To minimize the effect of collisions on the process, pulse length should be kept less than 1 ns when the target is at atmospheric pressure. A 1 ns pulse focused to a spot with a cross section area of about 1 mm^2 will need about 4 mJ to invert the two levels if we assume the “weak” coupling ($M = 5.7 \times 10^{-33} \text{ Cm}$). In an evacuated cell, one should be able to reduce the relaxation effects to allow 100 ns pulses. In this case, the excitation beam (with the same 1 mm^2 cross section) must have over 0.7 mW of peak power, even when assuming “strong” coupling. ($M = 4.7 \times 10^{-30} \text{ Cm}$)

[81] calculates the FCFs for numerous transitions. Most seem to be between 10^{-2} and 10^{-3} ; thus, we assume that the transition under consideration here has a FCF in this range. Many transitions have small FCFs, for example for $\nu' = \nu'' = 0$ the FCF is 1.429×10^{-9} ; however, the density of transitions in molecular iodine is high enough such that we can usually find a strong transition nearby – even when dealing with a spectral window only a few hundred MHz wide. We will take the logarithmic average of $|M_+| = 4.7 \times 10^{-30} \text{ Cm}$ and $|M_-| = 5.7 \times 10^{-33} \text{ Cm}$ as an approximate coupling:

$$M \equiv |M_{01}| = \exp \frac{\ln |M_+| + \ln |M_-|}{2} \text{ Cm} \sim 1.6 \times 10^{-31} \text{ Cm}. \quad (4.1.2)$$

In Figure 4.1 we plot Equation 2.1.24 (with $\Delta \cdot \tau = \pi/2$) for M_+ , M , and M_- .

4.1.2 Energy level model

The two energy levels in consideration here, X and B , each consist of many sublevels due to the vibrational and rotational wave functions [39]. The dependence of the

energy levels on the nuclear spins is small; however, the symmetry properties of the nuclear wave function can still influence the energy transfer during collisions (and influence which molecules couple to the laser field) [77]. Since we plan to avoid time scales which would allow collisional effects to become significant, we will ignore the nuclear portion of the wave function. When the symmetry rules for dipole transitions between X and B are applied one finds that transitions where $\Delta J = 0$ (“Q” transitions) are forbidden leaving only $\Delta J = \pm 1$ (“P” and “R” transitions).

The vibrational spacing is around 150 cm^{-1} while the rotational spacing corresponding to the P and R transitions ($\Delta J = 2$) is about 10 cm^{-1} for the Boltzmann populated transitions. Since kT is about 200 cm^{-1} at room temperature we see that many rovibrational levels will have significant population within the X electronic state. In fact, there will be hundreds of occupied rovibrational levels in the X band, each connected to tens of rovibrational states (“only” tens because of the selection rules: the initial and final vibrational states are not constrained; however, the rotational quantum numbers must obey $\Delta J = \pm 1$), making thousands of transitions which one would have to track in a model of excitation and fluorescence.

4.2 Multi-color LIF simulation

An estimate of the target/non-target discrimination ratio is calculated in this section. The iodine molecule is selected as the non-target and isotopic iodine 127–129 is used at the target; this is considered a worst case scenario since both molecules will have similar transitions. The key advantage of the three color LIF detection methods presented here is the fact that the fluorescence response of the target can be moved to higher frequencies *without* significant non-target “following”. The unique blue shifted fluorescence spectrum is found to dominate the non-target’s fluorescence in certain spectral windows.

4.2.1 The Lorentzian tail

The exponentially damped fluorescence response of the excited molecules has a Lorentzian spectral line shape:

$$L(\nu) = \frac{1}{\pi} \frac{(\Gamma/2)^2}{(\nu - \nu_0)^2 + (\Gamma/2)^2} \quad (4.2.1)$$

where Γ is the FWHM (not related to the density matrix Γ 's from Section 3.3.2), ν_0 is the frequency associated with the fluorescence transition. This is related to the exponential decay by

$$\Gamma = \frac{1}{\pi\tau} \quad (4.2.2)$$

where τ is the mean lifetime of the decay. This function is normalized such that

$$\int_{-\infty}^{\infty} L(\nu) d\nu = 1. \quad (4.2.3)$$

With respect to its peak, the Lorentzian's magnitude decreases by

$$L' = \frac{(\Gamma/2)^2}{(\nu - \nu_0)^2 + (\Gamma/2)^2} \sim \frac{(\Gamma/2)^2}{(\nu - \nu_0)^2} \quad (4.2.4)$$

where the latter case holds for $2(\nu - \nu_0)/\Gamma \gg 1$. Thus, assuming Γ is about twice the FWHM implied by a 1 ns mean lifetime (about 0.02 inverse cm), if we were able to shift the fluorescence energy of the target (i.e. the signal) to a spectral region 1000 cm^{-1} away ($|\nu - \nu_0| = 1000 \text{ cm}^{-1}$) from the non-target's fluorescence energy (i.e. noise), the energy of the non-target would be down by 10 orders of magnitude at that spectral location (SNR of 100 dB). For example, if the excitation wavelength is 628 nm (and the non-target emits its fluorescence energy at this frequency) then this would imply we would need to center our spectrometer at 591 nm or less to ensure the non-target's fluorescence response is reduced by 10 orders of magnitude. This turns out to be a lower bound on the spectral distance since some of the non-target's fluorescence energy will “follow” the target's energy to some extent. We approximate the effect of this “following” on the SNR in the following sections.

4.2.2 Dynamics approximation

We seek an approximation to the population dynamics such that we can estimate the final state of a molecular ensemble subject to various pulse sequences (with this information we can build a rough model for the resulting fluorescence spectrum); however, tracking the dynamics (with, for example, Equation 2.1.12) of the thousands of transitions involved would be difficult on a computer. In the following analysis, we ignore the dynamics and assume the probability of level inversion to a function of the detuning only. We also reduce the number of possible pathways to two: the upper electronic state can either populate through a single color transition or a three color “N” transition (see Figures 4.2 and 4.3). Suppose the probability of some specific transition inverting in a randomly selected molecule, P , is given by

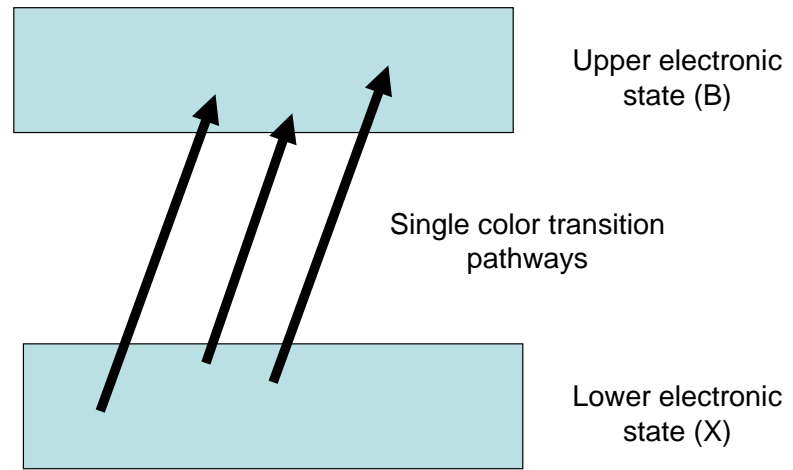


Figure 4.2: Single transition diagram. The upper and lower electronic states have a relatively dense substructure of ro-vibrational levels between which we induce transitions.

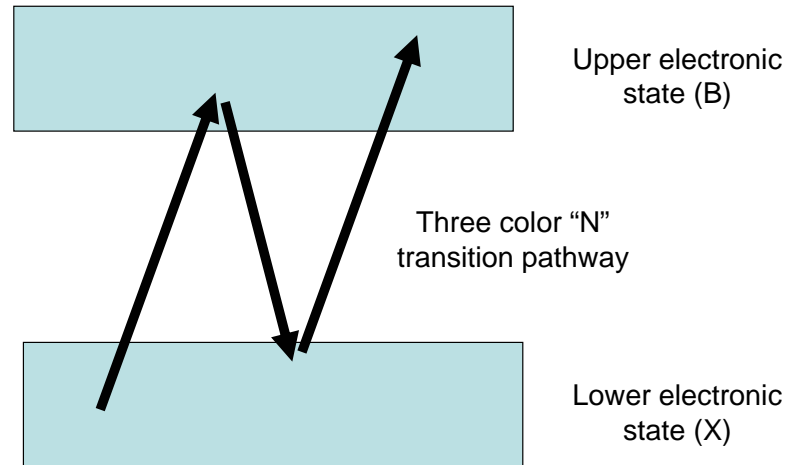


Figure 4.3: “N” transition diagram.

$$P(J'', \nu'', J', \nu') = L'(J'', \nu'', J', \nu') FCF(\nu'', \nu') Boltz(\nu'', \nu') \quad (4.2.5)$$

where L' is from Equation 4.2.4 (in Equation 4.2.5 L' is interpreted as the detuning lineshape for non-resonant excitation; however, in Section 4.2.1 it was used to describe the rate at which fluorescence energy decreases with respect to detuning of the observed spectral window – same line shape but different process), FCF is the Franck-Condon factor, and $Boltz$ is the normalized Boltzmann probability for population of the lower state (i.e. the probability that the randomly selected molecule occupies the lower state of the transition of interest). In this way we obtain an estimate on the distribution of excited upper states due to single color excitation.

For a three color process (tuned to the target molecule), the second color's effect is treated much the same way except the upper B state becomes the “source” for the population transfer. Instead of the $Boltz$ factor we use the P 's from the first color; in short, the ensemble of states “pulled” up from the X state are “pushed” back down to the X state by the second color. Now the third color “pulls” this ensemble back up to the B state. In this way we obtain an estimate of the distribution of excited upper states due to three color excitation through a designed resonant pathway (an “N” transition).

The goal here is to create a unique population inversion in the target molecule which will glow in the green, while non-targets will glow red. In addition to the resonant pathway described above, there are many pathways one would have to average to gain a good estimate of the actual distribution of the upper states when using an approximation of this type. (The alternative is to track them with Equation 2.1.12.) For the purposes of this argument, we will only compare the resonant pathway to the single color pathway. To support this assumption, the pathway is selected such that the second color pushes the resonant ensemble to an empty region of the X band. In our model we have FCFs for transitions involving lower states with vibrational quantum numbers up to 30: the energy for the X state with $\nu'' = 30$ and $J = 0$ is $5916.8561 \text{ cm}^{-1}$, more than 29 times kT ; so selecting an empty region of the X state is relatively easy.

4.2.3 Single vs. three color LIF

From these final upper state distributions a fluorescence spectrum is calculated. Each energy level in the calculated upper B state distribution is connected, in a $J = \pm 1$ pair, to each X vibrational state. A “fluorescence line strength”, S , is assigned to each

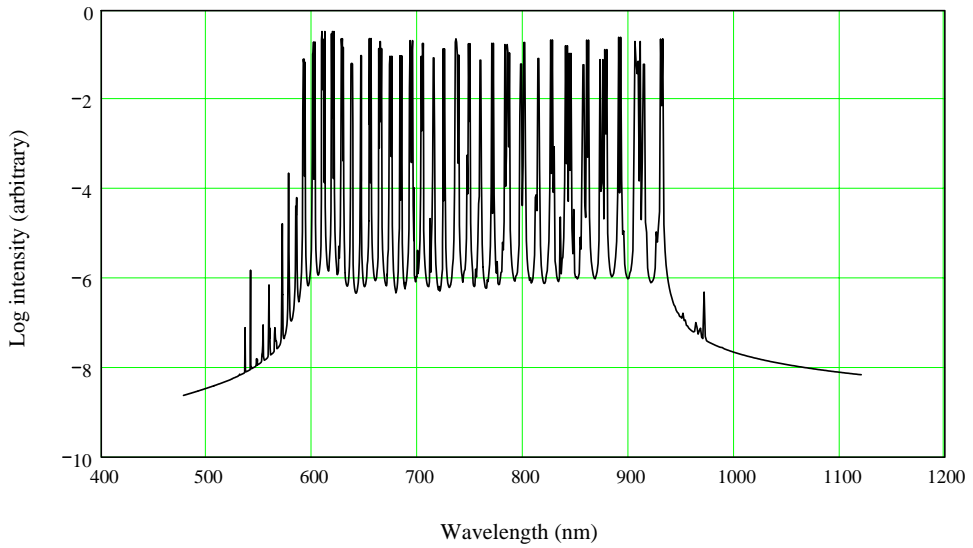


Figure 4.4: Simulated single color LIF from non-target molecule (iodine non-isotope)

possible downward transition and approximated by

$$S(\nu'', \nu') = P' FCF(\nu'', \nu') \quad (4.2.6)$$

where P' is the initial population of the fluoresceing B level (ν'') calculated for each pathway, and ν' is the vibrational number of the lower X vibrational level. The resulting fluorescence signal from each transition is modeled by Equation 4.2.1 by assigning each J-split pair to a Lorentzian scaled by S . See Figure 4.4, 4.5, and 4.6 for a plots of the resulting signal from summing the transitions for a few basic pathways. Note that when one considers the result from Section 2.2.4 (only around one thousand of iodine molecules emit into the detector in the benchtop geometry) we see that verification of these high extinction ratios becomes unlikely unless we move to a LIDAR type geometry.

4.3 Coherent population transfer

In this section we describe the unique advantages to the coherent control process under investigation. Evidence for an increase in potential LIDAR sensitivity is revealed when one considers the robust population inversion properties of these coherent process. The detuning properties are shown to not have an adverse affect on discrimination and allow near-unity population transfer efficiencies even with non-uniform spatial intensity distributions and shot-to-shot pulse height variations (we re-visit and re-analyze some of the results from Section 3.2).

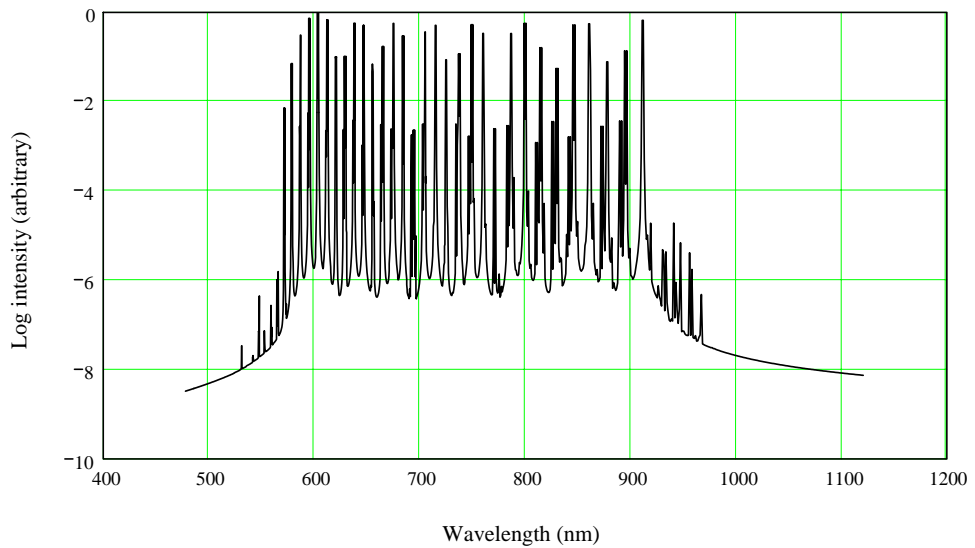


Figure 4.5: Simulated single color LIF from target molecule (iodine isotope)

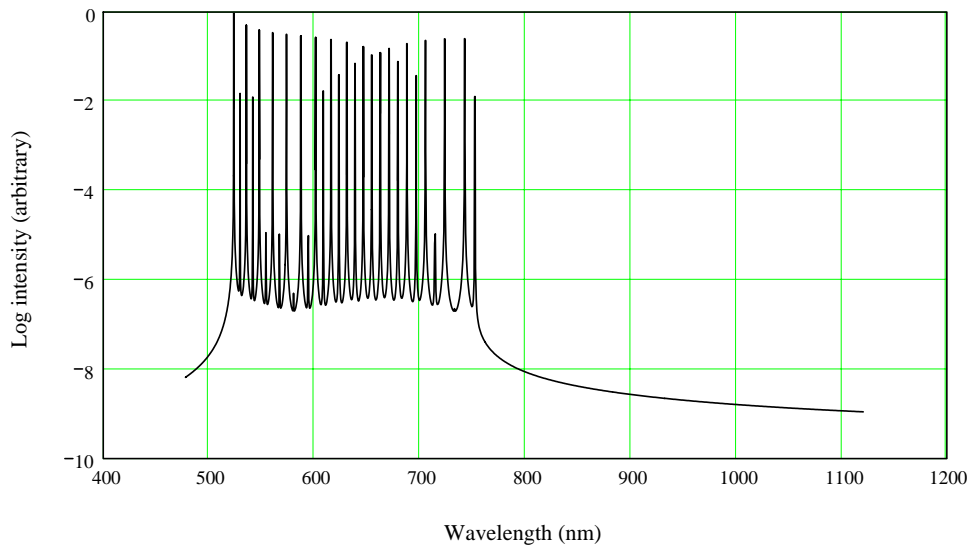


Figure 4.6: Simulated three color LIF from target molecule (iodine isotope). These simulations show that the three color LIF (shown here) is around 8 orders of magnitude more intense than the single color response of the target and non-target (see Figures 4.5 and 4.4) in the spectral region near 520 nm.

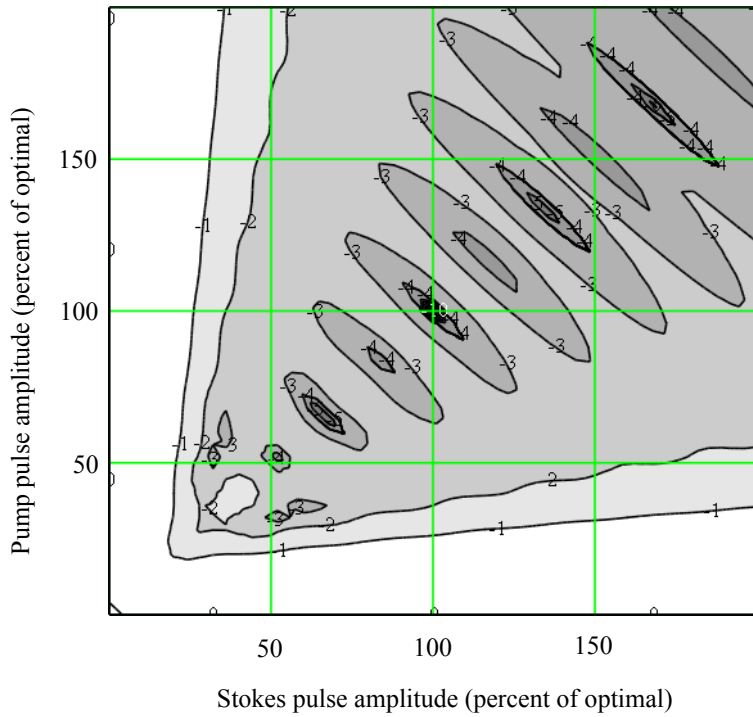


Figure 4.7: Residue surface for various pulse intensities.

4.3.1 STIRAP pulse height insensitivity

One important feature of the STIRAP process is the independence of the inversion on pulse height (first discussed in Chapter 3). Figure 4.7 shows the surface

$$\Phi' = 1 - P_2(t_N) \quad (4.3.1)$$

with respect to the amplitudes of the two pulses in the two color solution (STIRAP) shown in Figure 3.6. Φ' is defined in a manner similar to Equation 3.1.7 - in fact, the surface in Figure 4.7 is similar to, but not the same as, the surface in Figure 3.10. Since $\Phi' \sim 0$ means the inversion was mostly complete, we see that for a majority of the transitions shown in Figure 4.7 the inversion was complete to better than 1 part per thousand. Figure 4.8 shows Φ' for the case of simultaneous scaling of the pulses. Compare this to Figure 4.9 where the three color STIRAP is analyzed in a similar way, and we see that the three color STIRAP does not exhibit the same “robustness” to pulse amplitude scaling.

The robust features of the STIRAP with respect to pulse heights has more advantages than the resistance to amplitude instabilities of the laser source (explored in Section 3.2). Here we examine its effect on the “polarization damping” studied in Section 2.1.3.

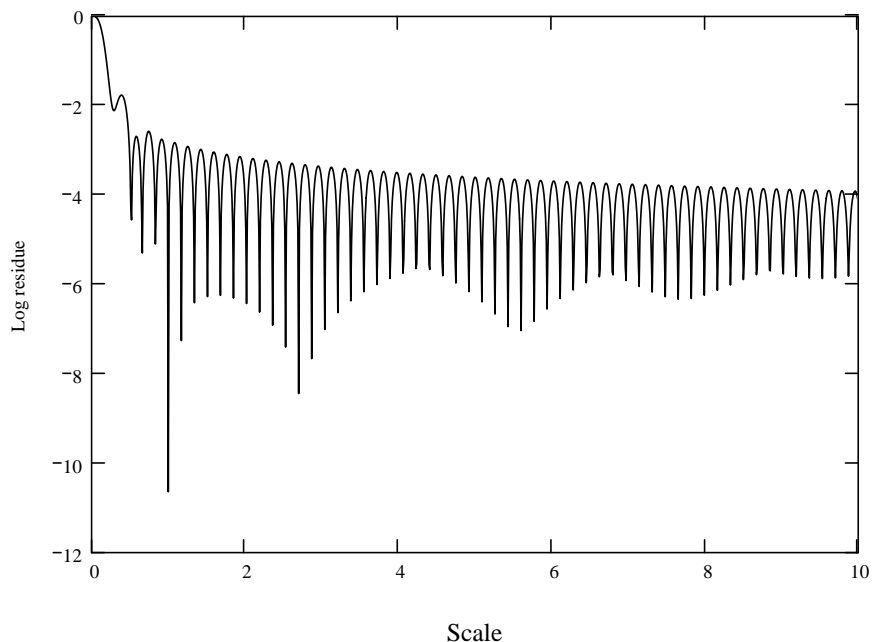


Figure 4.8: Amplitude “robustness” of the two color STIRAP. The optimal solution in Figure 3.6 is allowed to vary in pulse height by the “scale” factor (both pulses are scaled simultaneously) and the resulting residue, as defined by Equation 4.3.1 is plotted as a function of the scale. The narrow downward “spikes” are real; however, their depth may not be accurately displayed here due to “aliasing” effects between the regular spacing of computer generated points and the sharp spikes. In short, the residue is around 10^{-3} for most of the range of the “scale” factor, except for numerous “pits” where the residue drops to 10^{-6} or less.

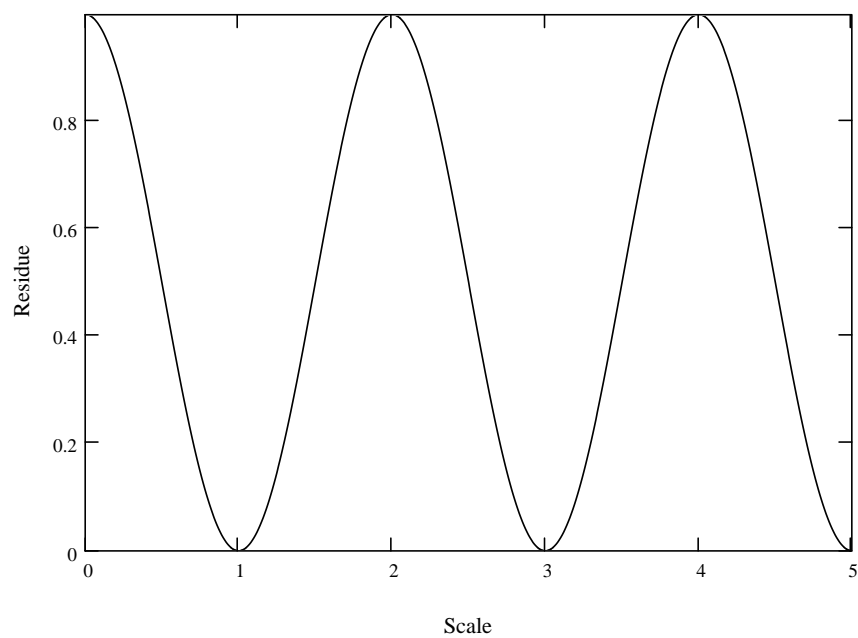


Figure 4.9: Amplitude “non-robustness” of the three color STIRAP. The optimal solution in Figure 3.13 is allowed to vary in pulse height by the “scale” factor (all three pulses are scaled simultaneously) and the resulting residue, as defined by Equation 4.3.1 is plotted as a function of the scale.

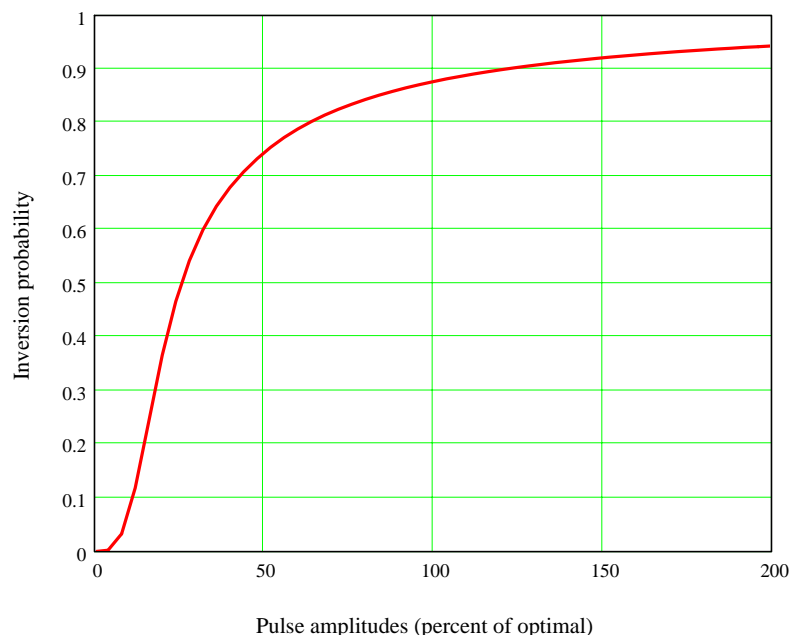


Figure 4.10: STIRAP inversion of a randomly oriented ensemble. Compare this with the dynamics shown in Figure 2.2 and we see that the STIRAP process approaches a coherent 100% inversion in the semi-classical analysis of a randomly orientated ensemble while the standard single color method of inverting the ensemble tends toward an incoherent 50% inversion with oscillations.

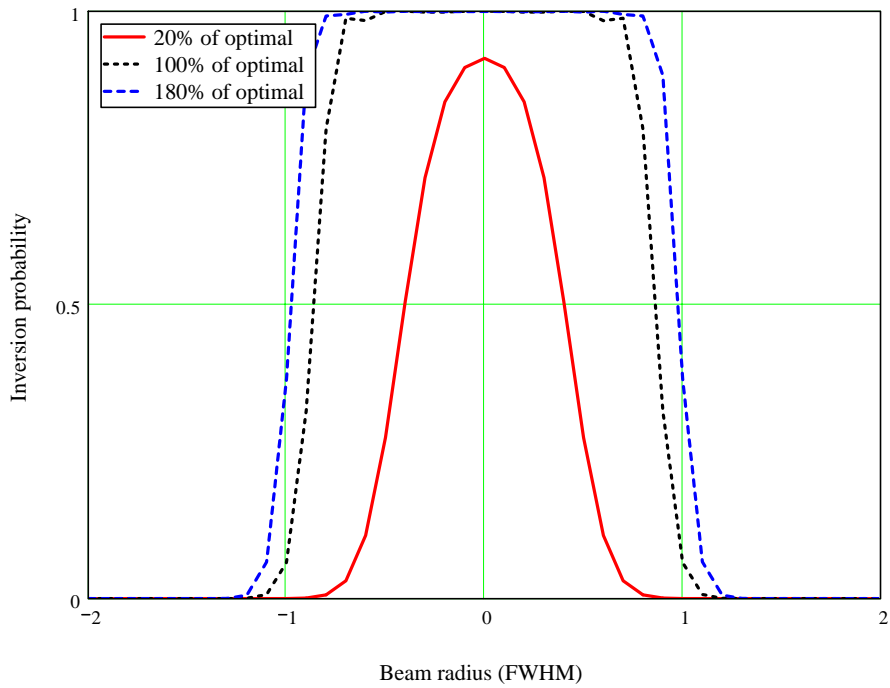


Figure 4.11: Inversion probability across a Gaussian beam profile

The pulse amplitudes are allowed to vary as a pair (the pulses remain of equal height) and an average similar to Equation 2.1.26 is calculated using a numerical integration. In Figure 4.10, we see that even at “only” 100% of the optimal pulse height over 85% of the population is inverted and at 200% of optimal the population inversion approaches 95%. The STIRAP process also turns out to be beneficial when one considers the spatial distribution of the inverted molecules an a Gaussian beam. The pulse amplitudes are allowed to vary as a pair (the pulses remain of equal height) and the population inversion is calculated across the cross section of Gaussian beam. We see in Figure 4.11 we see that near top hat cross section are possible.

4.3.2 The STIRAP detuning ridge

The STIRAP process has a unique “detuning” feature very different from the corresponding feature for two sequential π -pulses. The single π -pulse detuning curve is a sinusoid modulated by a relatively wide Lorentzian (see Section 2.1.4). The FWHM of this Lorentzian is half the Rabi frequency or, in order to beat the relaxation effects in atmospheric conditions, about one half GHz. This is on the order of the Doppler broadening, so for this discussion, the overall Lorentzian width of a single π -pulse is near 0.03 inverse

Stokes detuning vs. pump detuning (log)

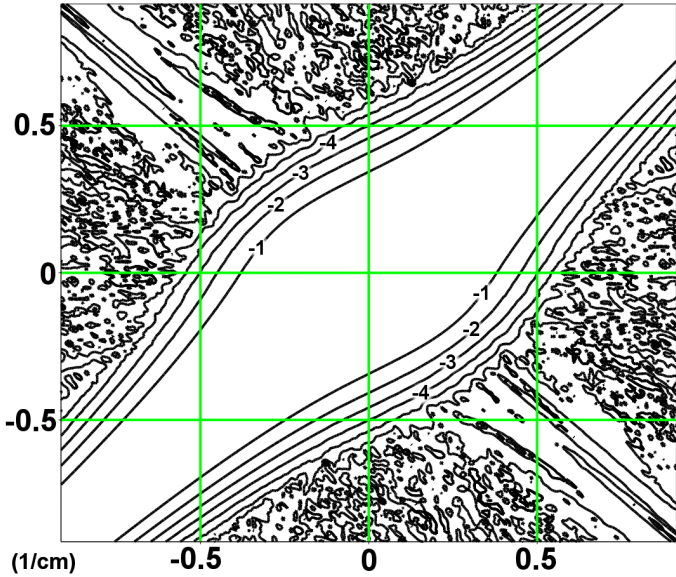


Figure 4.12: STIRAP detuning ridge - The log of the inversion probability is plotted here. See Figure 4.14 for the definition of the Stokes pulse and the pump pulse.

Stokes detuning vs. pump detuning

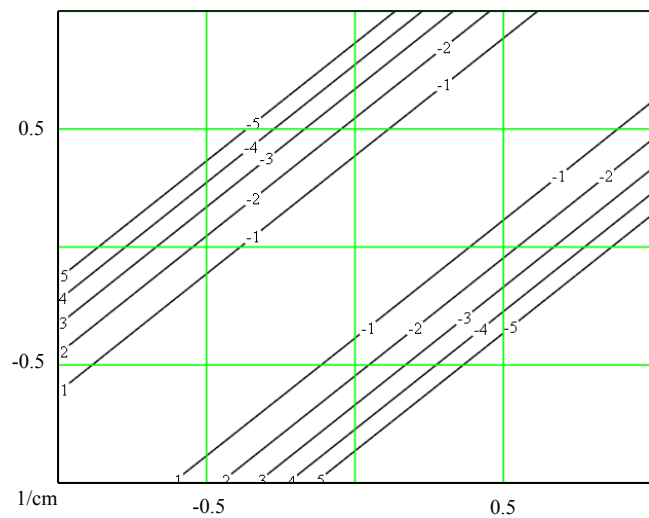


Figure 4.13: STIRAP detuning ridge fit - The log of the inversion probability is plotted here.

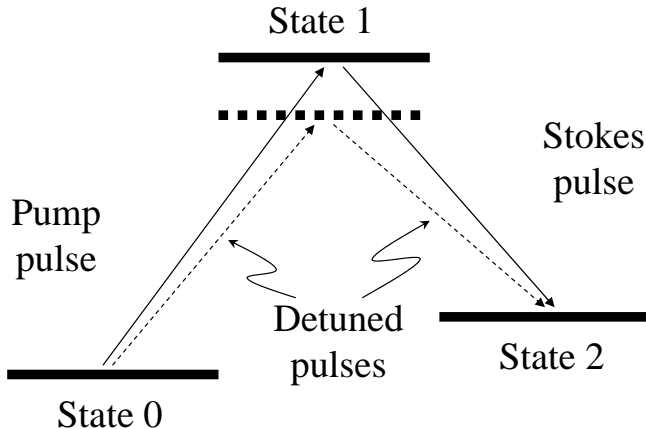


Figure 4.14: Stokes and pump pulses in a Λ system. Here we show the pump pulse (connecting states $|0\rangle$ and $|1\rangle$) and the stokes pulse (connecting states $|1\rangle$ and $|2\rangle$). In Figure 4.7 we show the effect of amplitude variations on the residue. Also shown here are two *equally* detuned pulses. The figure suggests that significant population will still transfer, but only when the detunings are nearly equal. See Figure 4.12 for an actual calculation.

cm. To obtain the two π -pulse detuning line shape we plot the surface formed by the inversion probability as a function of the first pulse (Stokes) detuning and the second pulse (pump) detuning and we get a Lorentzian ‘‘mountain’’ with a rough FWHM of 0.03 inverse cm (see Figure 4.14 for the definition of the Stokes pulse and the pump pulse).

To obtain a similar detuning feature for the STIRAP process we start with Equation 2.1.12, obtain equations similar to Equations 2.1.30, apply the STIRAP pulse sequence, and numerically calculate the inversion probability for various detunings. It is found that (see Figure 4.12) the detuning feature is a ridge with a long extent along the ridge (roughly fits a Lorentzian with a FWHM of 21.2 inverse cm) and a sharp fall-off along the anti-ridge (roughly fits a Gaussian with a FWHM of 0.424 inverse cm).

To model the effects of this detuning feature of the STIRAP process on the fluorescence spectrum we fit the ridge to an analytic function and use this fit in the computer model described in Section 4.2.2. The Lorentzian in Equation 4.2.5 is replaced with the ridge fit (see Figure 4.13) and a resulting fluorescence spectrum is calculated.

To compare the STIRAP + π -pulse (scheme 1) to the three π -pulse (scheme 2) scheme, we generate plots similar to Figure 4.6; however, instead of attaching Lorentzian line shapes to each LIF transition we simply plot each transition. See Figure 4.17 for a plot of the LIF transition supported by scheme 1 for the target molecule, Figure 4.18 for scheme 1 on the non-target molecule. Compare these plots with Figures 4.15 and 4.16 and one

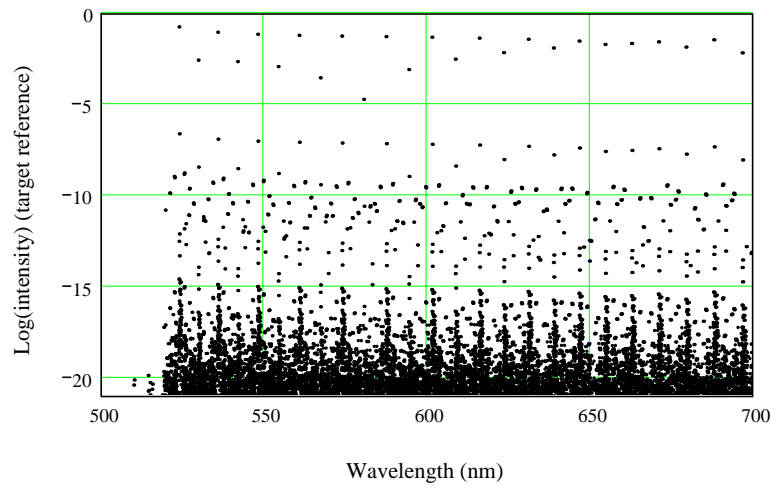


Figure 4.15: Simulated three π -pulse pathway LIF line strengths (target)

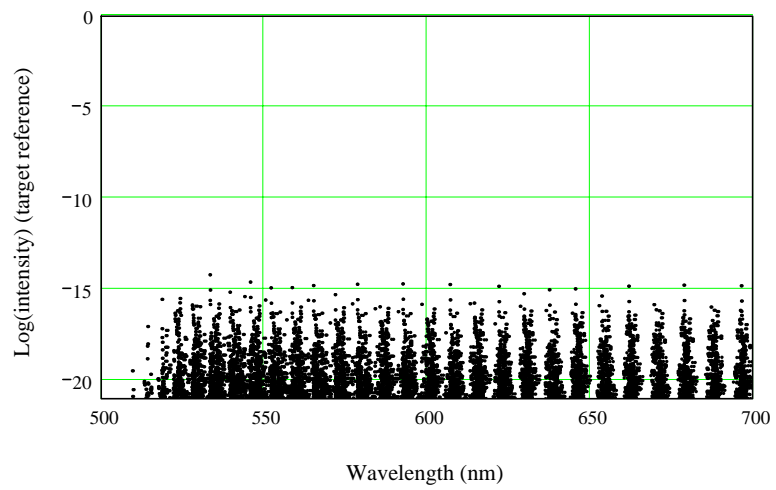


Figure 4.16: Simulated three π -pulse pathway LIF line strengths (non-target)

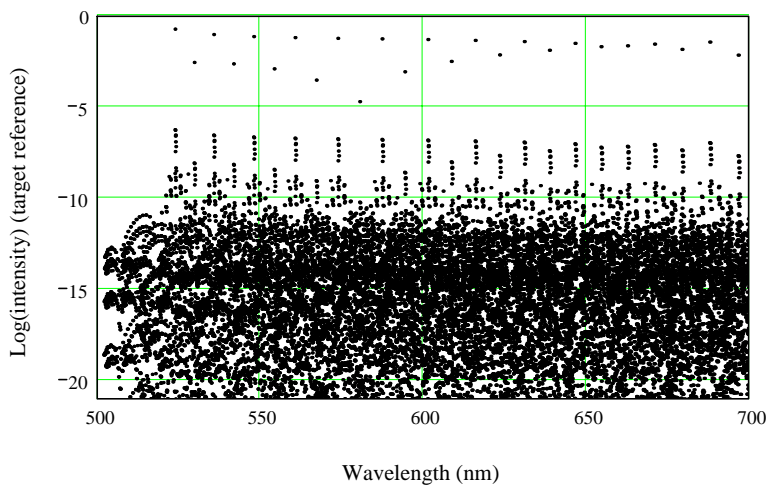


Figure 4.17: Simulated STIRAP + π -pulse pathway LIF line strengths (target)

sees that scheme 1 “pulls” more transitions through the three color pathway than scheme 2. This is one drawback of the robustness of the STIRAP process; however, it does not adversely affect the selectivity of the process since the Lorentzian tail of the fluorescence still dominates (see Figure 4.6 and 4.4).

4.4 Conclusion

The iodine molecule is introduced, the iodine energy level system is described, two basic three color schemes are proposed, the perceived advantages are described (through computer simulation), and the rationale behind each scheme design is explained.

The population transfer methods described in Chapter 3 are applied to a “real” molecular system, the $X-B$ system of iodine. The coherent process called STIRAP is shown to have some advantages: it reduces the inefficiency caused by random polarization and can distort the inversion cross section across the transverse profile of a Gaussian beam to a desirable top hat shape. The very difficult problem of dynamically modeling the iodine when subject to three color pulse sequences is made tractable by some sweeping assumptions. The “robustness” feature of the STIRAP process is placed into the context of discrimination to determine if there is an adverse affect.

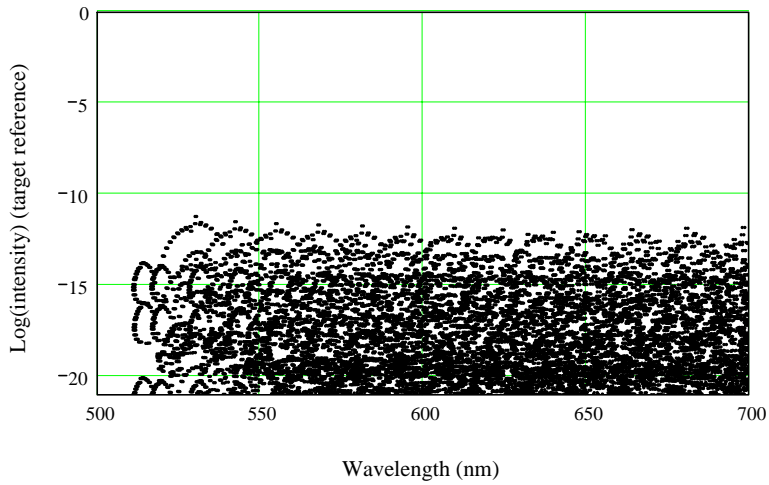


Figure 4.18: Simulated STIRAP + π -pulse pathway LIF line strengths (non-target)

A major advantage of the STIRAP line shape remains in the steep Gaussian like fall off when traversing the anti-ridge in Figure 4.12. In the dense competing energy structure of isotopic iodine, the STIRAP ridge picked up many non-target transitions; however, in some other application there may be a single localized transition or group of transitions, which produce significant noise in usual LIF schemes, but may be selectively suppressed by designing a STIRAP excitation scheme that places the non-target transition(s) far down the anti-ridge. In this way we can exploit the distinctly non-Lorentzian characteristic of this particular coherent process to develop a high SNR detection scheme.

Chapter 5

Laboratory Tests and Apparatus Development

In this chronologically organized chapter, the measurements that facilitate the development of the experimental apparatus are described. The first measurement described is a broadband absorption experiment conducted in November 2003. The basic data acquisition instrumentation is assembled and a first generation iodine cell is tested. The development continues up to a measurement of the LIF from solid anthracene conducted in March 2006 when the “ghost lines” from the grating in the 1 m monochromator are revealed. For each measurement the resulting contributions toward instrumentation are highlighted.

The loading system for a custom re-loadable sample cell is not complete and will not be included here. Experiments at various buffer gas pressures will be conducted when the system is ready; however, multi-color single-mode experiments await capable laser systems. Current efforts are centered on the production of single mode high power pulsed output using a tunable diode laser “idler” source amplified with a YAG pumped dye cell.

Reference [51] presents the absorption and LIF spectrum of molecular iodine. In this work we measure the absorption spectrum using LED’s instead of a white light source and we generate the LIF spectrum using green HeNe output and dye laser output instead of red HeNe output. Reference [47] reports the quenching of the total iodine fluorescence signal and [86] measures the lifetime of individual LIF features; however, these measurements were conducted at low pressure (0.03 Torr). In this work we look at the decay of a single LIF line at relatively high pressures.

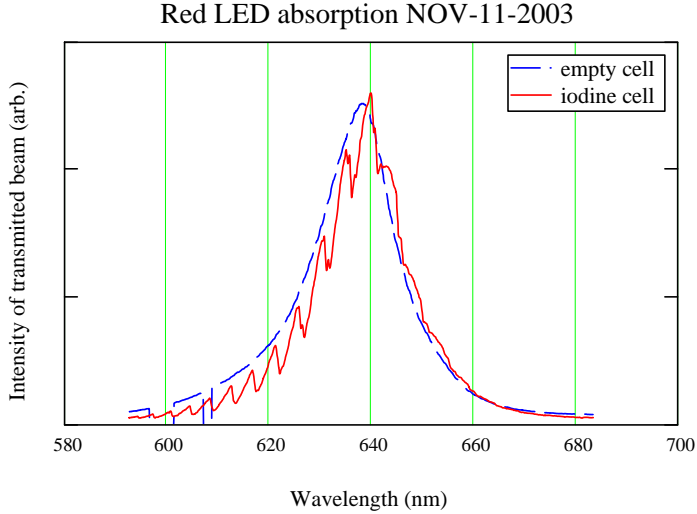


Figure 5.1: Red LED absorption in molecular iodine. The solid trace is about 2 times smaller than the dashed trace

5.1 Preliminary tests

One of the simplest fundamental spectroscopy experiments is bulk absorption. Here we describe a basic absorption experiment using low cost light sources which were immediately available: light emitting diodes (LED). The LEDs response to the high voltage output of a Hg wetted relay was measured. This allowed the development of the Hg pulser system and a fast photodiode. Finally HeNe based LIF measurements are used to vet two different beam line geometries, as well as test the Hg pulser/Pockels cell system.

5.1.1 Broadband molecular iodine absorption

We measure the broadband absorption spectrum of molecular iodine using LED illumination. Three LED's were used: red (see Figure 5.1), yellow (see Figure 5.2), green (see Figure 5.3). The absorption features match those in the literature in shape and spectral position. Also the general observation that iodine exhibits heavier absorption in the green than the red is supported by the data.

As one of the first measurements recorded, these experiments were used to develop the essential components of this spectroscopic study: spectral analysis, light detection, data acquisition, light sources, and sample preparation. A side-view PMT is mounted at the monochromator output and encased in an aluminum foil lined cardboard box; this

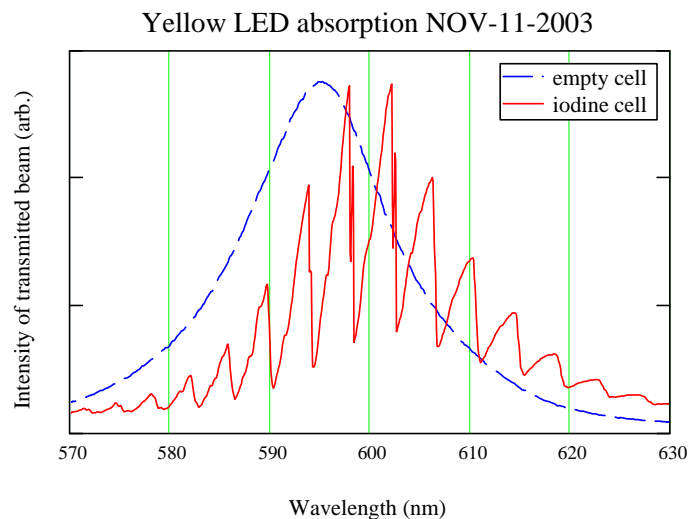


Figure 5.2: Yellow LED absorption in molecular iodine. The solid trace is about 5 times smaller than the dashed trace

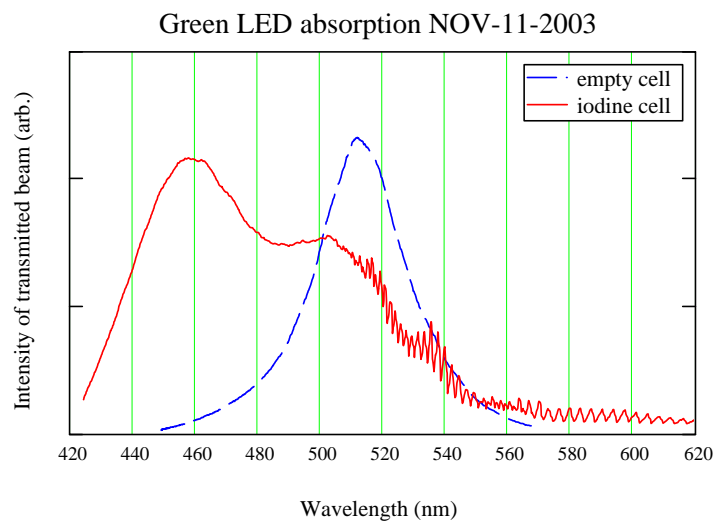


Figure 5.3: Green LED absorption in molecular iodine. The solid trace is about 10 times smaller than the dashed trace

primitive setup proves very reliable. A chart recorder is used to acquire data; the pen axis is “linearly” scanned using a voltage rise from a simple RC circuit. Data processing methods are developed to account for the non-linearity of the voltage rise. Gas lamp calibration procedures are developed for use with the monochromator.

A cell is prepared in a crude fashion by simply loading a sample cell with a few flakes of iodine in an unprotected environment (outdoors, in front of the physics building), closing the cell’s greased stop cock, connecting the cell to a mechanical vacuum pump, and evacuating the loaded cell at room temperature. The cell is closed off again, wrapped in heat tape, and temperature stabilized at 150° F with a bench top controller and used on the optical bench. Ideally at this temperature the overloaded iodine cell should have a collision lifetime of 11 ns, a density of 1.9×10^{17} molecules/cm³, and a pressure of 6.8 Torr (from an internal AHI document DN-3300-4 by Dr. Pui K. Lam). The cell is wrapped in aluminum foil giving it a “baked potato” appearance – hereafter, this cell will be referred to as such.

5.1.2 Boxcar averager and Hg pulser

Some of the LED absorption data were taken by pulsing the LED (using an HP model 8015A pulse generator) and averaging the PMT signal with a boxcar averager (PAR, model CW-1). The goal of this experiment is to determine the usability of the donated averager; it is determined that the averager is unusable in its present state. This prompted the purchase of a new boxcar averager system.

To check the performance of a high voltage fast rise time mercury wetted relay (C.P. Clare & Co., model HGSS 5060, called “Hg pulser” hereafter – see UH notebook UH-004 pages 49–53) and test the performance of a newly assembled fast photodiode (see UH notebook UH-015 pages 7–48), the LED’s used here were connected to the output of the relay and the resulting signal observed using the fast photodiode. The relay itself is found to perform faster than the response time of the scopes available in the lab. The LED tested can take at least 100 V in a 20 ns pulse without damage; however, it is found to have a slower response than the relay output. This may be due to the coupling between the LED and the signal cable.

5.1.3 Red and green HeNe LIF

Measurements of LIF from molecular iodine illuminated with red and green HeNe can be found in the literature and are performed in undergraduate labs. We repeat some

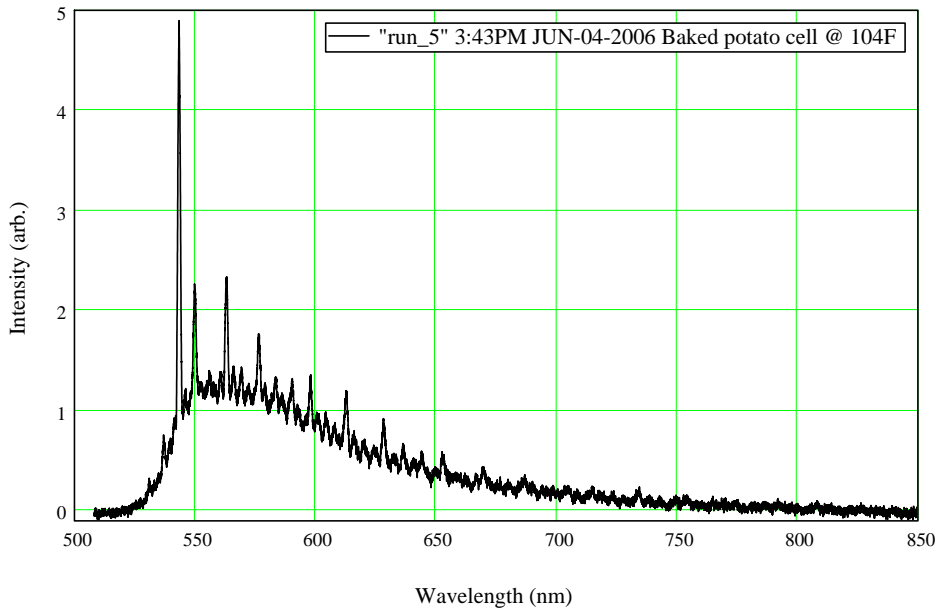


Figure 5.4: Red HeNe LIF from the “baked potato” iodine cell. Notice the broad pedestal absent in the “clean” cell scan in Figure 5.5 – see Section 5.2.2 for discussion.

of these experiments to verify the calibration procedures to acquire spectral data and the numerical model use to analyze these data. See Figures 5.4 and 5.5 for scans of a crudely prepared iodine cell and a scan from a commercially prepared cell.

The high voltage fast rise time relay mentioned in Section 5.1.2 will be used to provide the fast voltage pulse that will drive the Pockels cell in the final dye laser system. The simple beam line used for the LIF measurement mentioned above is exploited to test a recently acquired Pockels cell (Cleveland Crystals Inc., Impact 8 KD*P Pockels Cell with a 532 nm AR coating). A crude Pockels cell mount is quickly constructed and the red HeNe output is sent through two crossed polarizers with the Pockels cell mounted in between. Alignment proved difficult (this knowledge prompted the design and construction of a new Pockels cell mount); however, once setup properly, the Pockels cell/Hg pulser system worked well (see Sections 7.3.1 and 7.3.2 or UH notebook UH-015 page 59).

5.2 Dye laser test

This section describes three experiments mainly used to check the performance of the dye laser system (Sirah Laser model PRSC-D-24). A wavelength scanned absorption experiment reveals some problems with the mechanical systems in the dye laser. Resonant LIF from a quickly prepared cell confirms the trial molecule was a good choice and provides

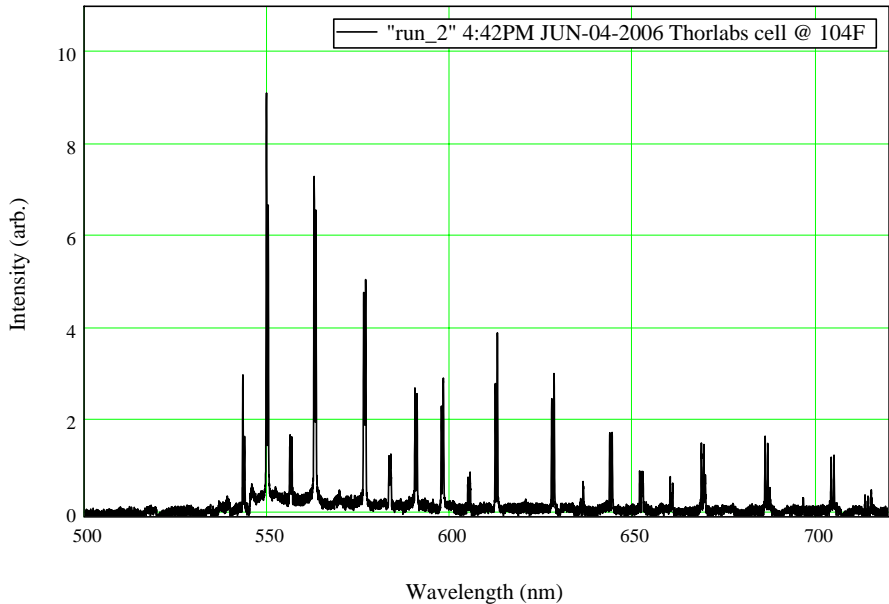


Figure 5.5: Red HeNe LIF from a “clean” commercial iodine cell (Thorlabs)

an opportunity to develop an automated computer based data acquisition system. Scanning the dye laser wavelength in a region containing two absorption peaks and observing the resulting fluorescence signal at high resolution reveals a subtle calibration issue and demonstrates one of the key issues in molecular discrimination: the high transition density of these systems.

5.2.1 Dye laser absorption in molecular iodine

The spectral region around a targeted absorption feature is scanned in a stepwise fashion (the wavelength “scan” feature of the dye laser has proven unrealizable) using the “lambdalok” feature of the dye laser. These scans will be referenced later when we observe LIF from excitation in this region.

The output of the dye laser is sent through three attenuation tools before going though the “baked potato” sample cell. The 13 mJ beam from the dye laser [see UH notebook UH-016 pg 62)] is reduced by a factor of 4^3 after the attenuation tools [see UH notebook UH-015 pg 117)] for an incident energy of 200 uJ in each 8 ns pulse at 20 Hz. The beam which passes through the cell is detected with a photodiode and averaged with a boxcar integrator then tabulated as a function of dye laser wavelength.

The output of the boxcar averager is connected to the vertical axis of a chart recorder. At each “lambdalok” setting the vertical position of the pen is recorded after

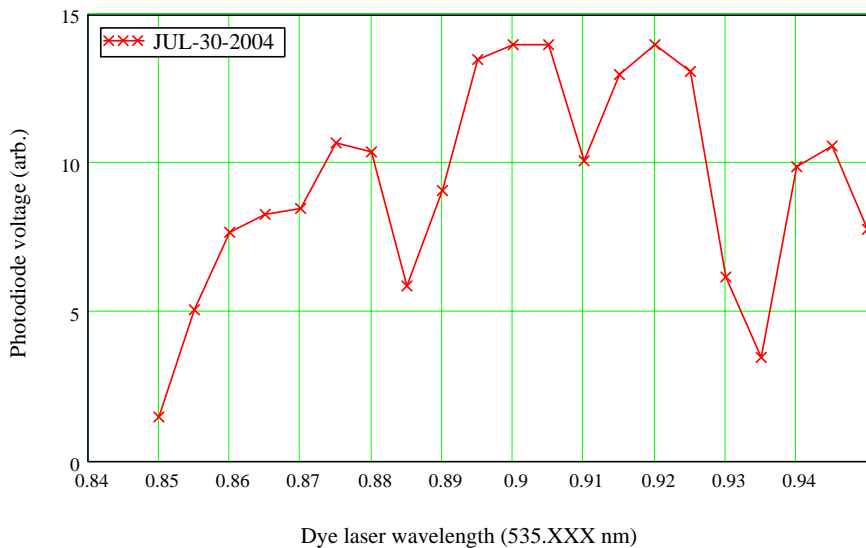


Figure 5.6: Iodine absorption dye laser scan. The fluctuations were about $\pm 20\%$ of the value on the vertical scale (see UH notebook UH-016 page 9).

the boxcar output stabilizes (the experimental repetition rate is 20 Hz and the “samples” setting on the averager is set to 300). See Figure 5.6 for a plot of these data. The absorption peak (the “peak” points down) near 535.885 nm is the focus of the following discussion.

There are two transitions under investigation in this study. The first is the transition between the $\nu'' = 0, J'' = 52$ state in the X band to the $\nu' = 30, J' = 51$ state in the B band, called “transition one” hereafter. The second is the transition between the $\nu'' = 0, J'' = 55$ state in the X band to the $\nu' = 30, J' = 56$ state in the B band, called “transition two” hereafter.

Transition one has an excitation energy corresponding to 535.8843 nm while transition two has an excitation energy corresponding to 535.8901 nm. The resolution of the scan is high enough to identify the absorption feature associated with these transitions; however, the individual transitions are not resolved and may indeed prove difficult to resolve with this scanning method. The goal of this exercise was not to identify specific peaks; instead, we simply seek to verify the performance of the dye lasers (again, it is discovered the “scan” feature was unreliable) and observe the basic absorption features of molecular iodine.

5.2.2 Resonant laser induced fluorescence

In this experiment the beam line is similar to the one described in Section 5.2.1 except here only one attenuation tool (measured pulse energy after the attenuator: 300 uJ)

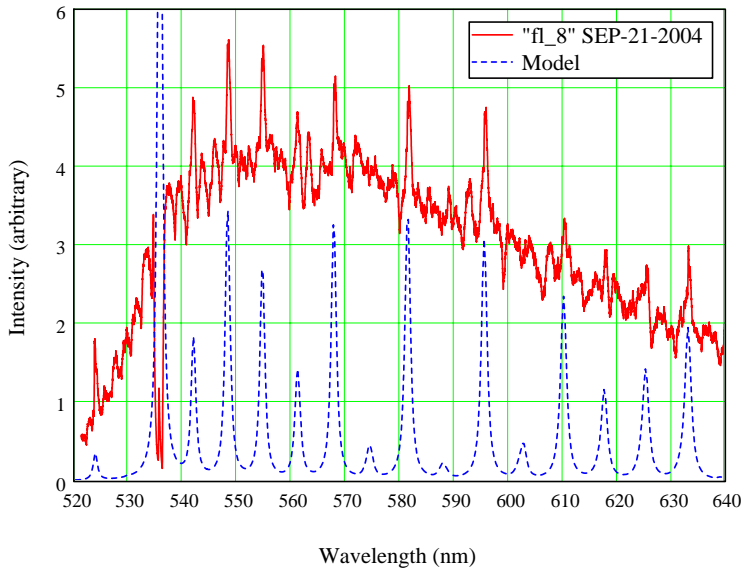


Figure 5.7: 535.8901 nm LIF from the “baked potato” iodine cell

is used and a +750 mm lens is placed 940 mm from the sample cell (between the sample cell and attenuation tool). The dye laser is tuned to 535.8901 nm and a side view geometry is used with a +100 mm object lens and a +500 mm image lens to collect the fluorescence radiation into a 1 m grating monochromator. A PMT is used to detect the signal at the monochromator output and a boxcar integrator is used to amplify/average the signal.

While targeting transition two (see Section 5.2.1) with the dye laser (wavelength set at 535.8901 nm), the boxcar output is recorded onto a computer while the monochromator is scanned from green to red. A 12.3 minute data run was recorded with the boxcar integrator “samples” setting at 30. The plot shows the raw data from the averager plus the numerical model output. During the wavelength scan a neutral density filter was inserted into the beam line to prevent PMT saturation (and possible damage) from the fundamental signal from the laser. This results in the discontinuity seen near 536 nm on the raw data trace (see Figure 5.7).

In general we have a large general spectral feature about 100 nm wide that “tails” off toward the red – this is typical of non-resonant fluorescence features, suggesting that the “baked potato” cell may have some contaminants (a reasonable conclusion). On top of the large feature are several distinct localized features corresponding to the resonant LIF response of molecular iodine. Comparing these features with the model calculation shows a close correspondence between the positions and relative heights of the peaks.

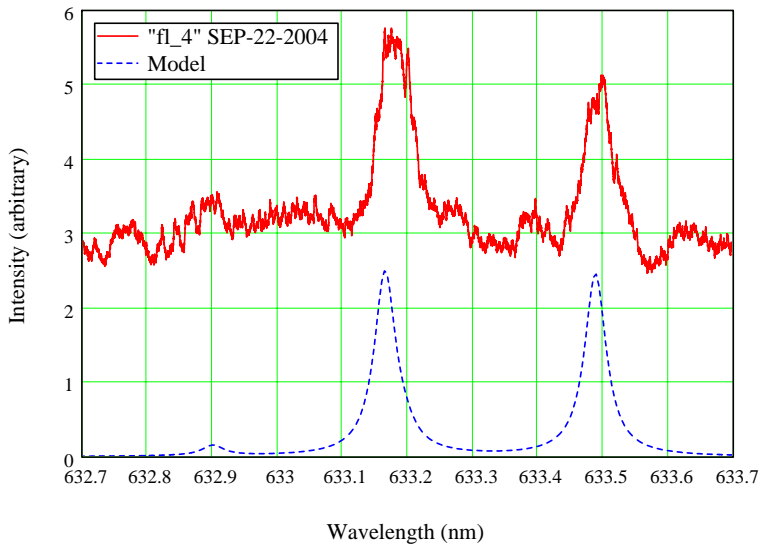


Figure 5.8: 535.8843 nm LIF (from “transition one”)

A major milestone in data acquisition development is reached in this test. The computer interface (Stanford Research Systems model SR245) purchased with the new boxcar system is introduced into the apparatus. LabView control software is written to simulate “chart recorder” type data acquisition; the data plotted in Figure 5.7 is one of the first data set acquired using the SR245.

5.2.3 Transition selection

The dye laser system maintains enough control of its output spectrum to allow discrimination between a target transition and its nearest strong neighbor. There may be some remaining calibration issues, but the numerical model for iodine LIF does a good job of modeling the observed spectral features in the LIF spectrum. Transition one and two (see Section 5.2.1) are selected by tuning the dye laser to their respective wavelengths and the resulting fluorescence spectra are observed.

The beam line used for these data is identical to the one described in Section 5.2.2 except two attenuation tools are used so that the energy after the attenuators is 120 uJ. The “lambdalok” feature on the dye laser is used to set the dye laser to within a claimed 2 pm of the set wavelength. Resulting iodine fluorescence spectrum features are analyzed and recorded for various excitation wavelengths.

The fluorescence feature near 633 nm is shown in Figures 5.8 and 5.9. The basic characteristics of the feature is its “paired” nature. Two lines representing the $J = \pm 1$

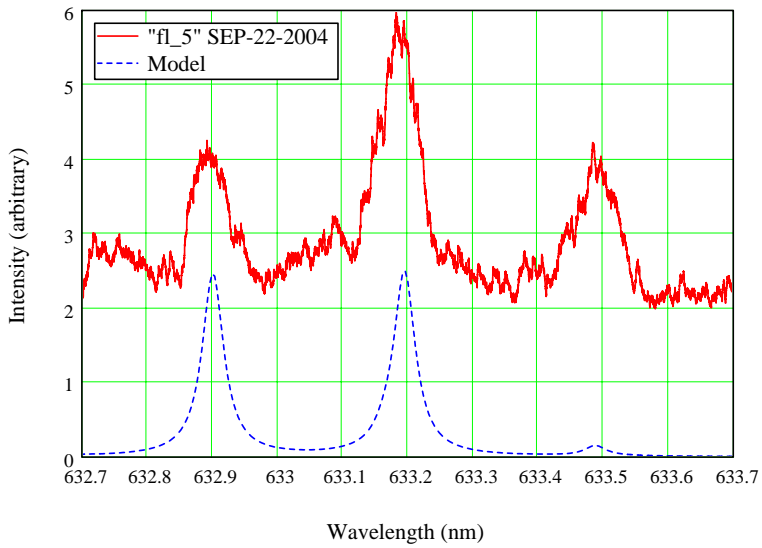


Figure 5.9: 535.8901 nm LIF (from “transition two”)

transitions (see Section 4.1.2) are clearly resolved in these data. The pair at 633.17 nm and 633.49 nm are associated with transition one (535.8843 nm). The pair at 632.90 nm and 633.20 nm are associated with transition two(535.8901 nm). See Figure 5.8 for the resulting features when the laser is tuned for 535.8843 nm and see Figure 5.9 for the resulting features when the laser is tuned for 535.8901 nm.

At first glance it seems that transition one was hit well and transition two was not. According to the model, the excited transitions (535.8843 nm and 535.8901 nm) should result in fluorescence with roughly the same intensity in the spectral window under consideration. Inspection of Figures 5.8 and 5.9 shows that the non-overlapped line (the right most line in Figure 5.8 and the left most line in Figure 5.9) do not have the same heights. In fact the data plotted in Figure 5.9 are consistent with excitation somewhere between transition one and two. This may be the result of a 3-4 pm shift in the calibration of the dye laser and/or the “lambdalok” feature performing below specification. And, since these transitions are separated by 6 GHz, it indicates that selective excitation can be difficult due to the relatively broad dye laser spectrum.

5.3 Single fluorescence line decay

Decay processes play a major role in this study. The target is assumed to be a relatively unprepared region of atmosphere; thus, in the actual application, we will have little

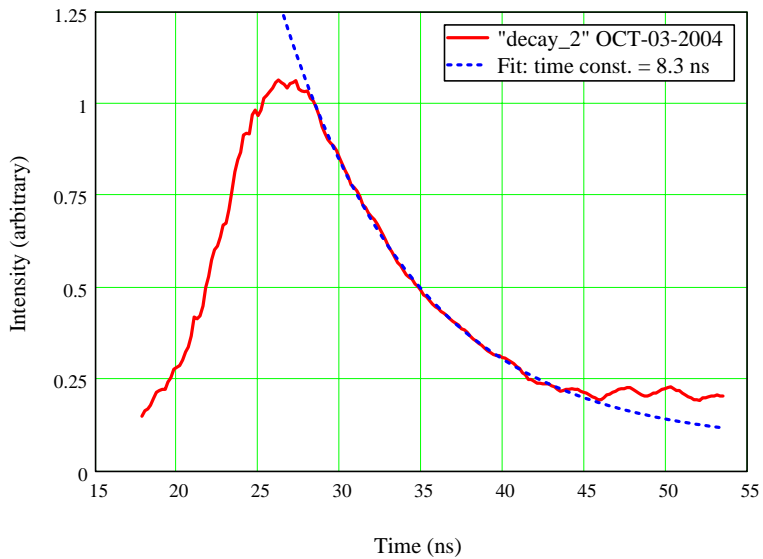


Figure 5.10: Decay of 535.893 nm LIF line at 632.9 nm (cell at 150° F). The decay rate is inconsistent with the ideal calculation from Section 5.1.1; however, considering the likely contamination of the cell (see Figures 5.4 and 5.7 and the associated discussion in Section 5.2.2

direct control of the parameters that influence the system relaxation. In the experiments leading up to the field demonstration, controlled samples will be used. Here we conduct an initial measurement of the lifetime of a single LIF feature using the “baked potato” iodine cell.

5.3.1 Pockels cell system integration

Integration of the Pockels cell into the dye laser system requires the design and assembly of a trigger/delay system used to trigger the YAG pump and delay the activation pulse to the Pockels cell until the incident dye laser pulse arrives at the Pockels cell location (see UH notebook UH-016 pages 56–59). The system consists of three signal generators (HP model 8015A pulse generators), a high voltage DC power supply to charge the Hg pulser (HP model Harrison 6525A), and the associated delay cables and attenuators. The Pockels cell is placed between two polarizing cube beam splitters.

5.3.2 Single fluorescence line decay in molecular iodine

There are several non-radiative decay mechanisms which can lead to an observed damping of the fluorescence lifetime of a single LIF line. The iodine molecule can dissoci-

ate, ionize (once, twice,...), internally decay via a non-optical transition, exchange energy through inelastic collisions, or de-phase through elastic collisions. In Section 3.3 we modeled de-phasing through collisions in a stochastic manner. Here we directly measure the observed decay of a LIF line in the “baked potato” iodine cell.

The beam line used here is similar to the one described in Section 5.2.2 except the attenuators are not used and in its place we use a pair of crossed polarizers (polarizing cube beam splitters) and a Pockels cell. The system has an extinction ratio of about 200:1 (see UH notebook UH-018 page 65) and produces a pulse with a FWHM of about 4 ns. Before the Pockels cell we have about 5.4 mJ, thus after the Pockels cell (heading toward the +750 mm lens) is about 27 uJ. The dye laser is tuned to 535.893 nm (a targeted absorption line) and the monochromator is tuned to capture a single LIF line at 632.9 nm. Again the signal from the PMT at the output of the monochromator is scanned (temporal gate scan) and averaged with a boxcar averager.

The measurement has facilitated the development of the data acquisition system required for lifetime measurements. The boxcar averager works at the 1000 ps gate width setting (it has settings down to 100 ps, but these have not been tried) and the LabView program records the data as a convenient text file. We have also discovered that the intensity fluctuations of the dye laser output introduce unwanted jitter in the position of the trigger relative to the peak – accurate lifetime measurements will require a way to eliminate the jitter or, better yet, reduce the intensity fluctuations in the input beam. Contamination of the cell may have introduced additional channels through which the iodine can decay. A clean loading method must be developed in order to isolate and measure specific effects on the fluorescence decay.

5.4 Aromatic compound LIF

Iodine is the trial system used to form the computational basis of many of the claims made in this dissertation. The scope of this general study and the development of the experimental equipment go beyond the iodine molecule; this section describes an experiment using naphthalene as a target. Temperature controlled sample cells containing naphthalene have been prepared along with flakes of naphthalene and anthracene. An attempt to observe a multi-photon process in these aromatic samples has led to more equipment development.

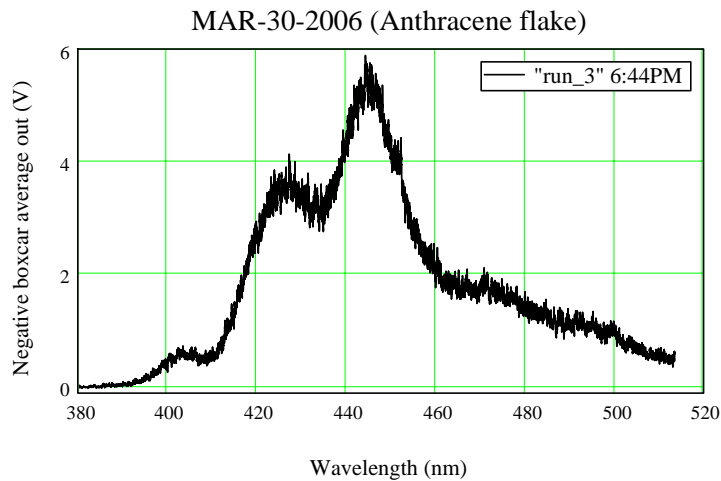


Figure 5.11: LIF from a solid anthracene flake illuminated by a 355 nm YAG

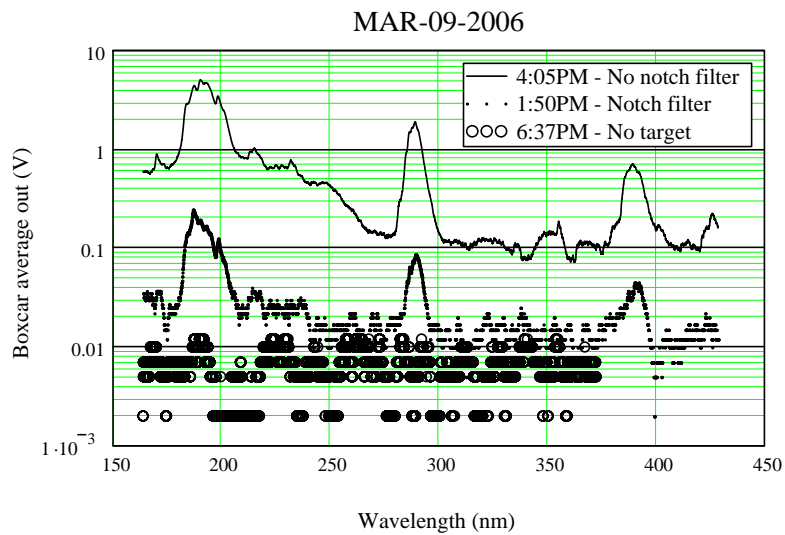


Figure 5.12: Grating ghosts from 1064 nm laser illumination. Using various targets (aromatic compounds, paper, and a calibrated Lambertian target) it was discovered that the spectral “features” observed in the UV were independent of the target. Then from the data shown here, acquired using a notch filter made for 1064 nm YAG output, it was concluded that the “features” were linearly related in intensity to the 1064 nm excitation and thus most likely “ghost lines” associated with the grating.

Measurements of the fluorescence response of aromatic compounds to YAG illumination have revealed some shortcomings of the 1 m monochromator. Figure 5.11 shows the LIF from an solid anthracene sample when excited by the output of a tripled Nd:YAG laser (355 nm). When the excitation is shifted to the doubled or fundamental output of the YAG, a complicated faint spectrum emerges in the scans. It was discovered that the faint features were independent of the target (paper and a white Lambertian target generated the same features). See Figure 5.12 for the ghost lines resulting from fundamental YAG (1.06 um) illumination. It is believed that these are “ghost lines” from sub-periods in the groove spacing [60]. A holographic replacement grating (which should be free of ghost lines) is being procured.

5.5 Conclusion

This chapter chronicles the stages of laboratory development undergone over the past few years. The main measurements at each stage were used as a guide to develop the equipment and techniques required for demonstration of molecular control in LIDAR systems.

As each stage was completed various components of the apparatus were either designed and assembled or evolved to the next generation. After the installation of the PMT at its output the monochromator served each experiment well until the recent aromatic compound measurements. The Hg pulser and Pockles cell system went through various stages of development starting with the initial tests of the Hg pulser on LED's to the integration of the system with the YAG pumped dye laser system during the fluorescence line decay measurements. The software model was tested at each stage from the familiar non-resonant HeNe LIF to pulsed resonant dye LIF. The data acquisition system was built for the first dye laser experiments and has remained relatively unchanged since then. Recently, a calibration issue with the monochromator self scan feature has prompted the need of a second generation of the data acquisition software.

Chapter 6

Mode Content of the Dye Laser System

In the chapter, a set of measurements used to determine the mode content of the dye laser output is presented. The transverse mode content is approximated by simulating transverse images recorded from a CCD. The dye laser beam's M^2 is also calculated. The axial/transverse mode content is measured by observing the RF beat spectrum of the laser output. It is shown that the estimated mode content of the laser output is not amenable to coherent molecular control.

Reference [19] describes the implementation of a single mode dye laser system. The limited tuning range renders the system un-useable in exploratory exercises; however, the techniques may be useful once target molecules are finalized and an exact excitation scheme is proposed with some confidence. Reference [76] discusses the theory of multi-mode laser output. The Hermite–Gauss basis set is used here to model the CCD images of the laser beam's transverse profile.

6.1 Transverse mode structure of the dye laser output

Measurements of the transverse variation in intensity of the dye laser output at various positions along the beam line are used to estimate the spatial mode content of the beam we had planned to use in coherent control experiments. A rough decomposition of the observed beam into the Hermite–Gauss modes is presented after an estimate of M^2 [1] is reported.

6.1.1 Experiment layout

A +2 m lens is placed 199.8" from the output surface of the dye laser. The beam is brought to a focus about 286.8" from the output surface (87" downstream from the lens). A CCD camera designed to record the transverse profile of laser beams (Spiricon, model COHU 4812) is placed on a rail such that images can be recorded at various positions along the beam line near the focus. The control software for the camera can record images and calculated parameters (like the $1/e^2$ width of the beam) for each shot of the dye laser. Figure 6.1 shows a fit made from the $1/e^2$ widths data and Figure 6.2 shows beam profile images recorded near the focus.

6.1.2 M^2 estimate

A rough estimate of M^2 for the beam from dye laser #22 is obtained from data acquired using the Spiricon CCD array system. Many shots were acquired at various positions downstream from a +2 m lens (more than 1000 at each position). For each shot, the Spiricon system records the $\frac{1}{e^2}$ full widths (the result of a Gaussian fit) of both the horizontal and vertical projections of the beam cross section. These widths are averaged (first horizontal and vertical, then to simplify the analysis these two are averaged together) over each set to give a single width at each beam position.

A Gaussian beam profile is manually fit to these data. The two free parameters used in the fit were waist position and far field divergence. The equation for the $\frac{1}{e^2}$ envelope of a Gaussian beam is [67]

$$w(z) = w_0 \sqrt{1 + \frac{(z - z_0)^2}{z_R}}, \quad (6.1.1)$$

where

$$w_0 = \sqrt{\frac{\lambda z_R}{\pi n}}, \quad (6.1.2)$$

and z_0 is the position of the waist, z_R is the Rayleigh parameter, λ is the wavelength, and n is the index of refraction. The Gaussian beam is propagated by keeping track of the complex source point, q . The real part of q is the distance the waist lags behind the origin and the imaginary part of q is the Rayleigh parameter. In free space, q propagates according to

$$q' = q + L \quad (6.1.3)$$

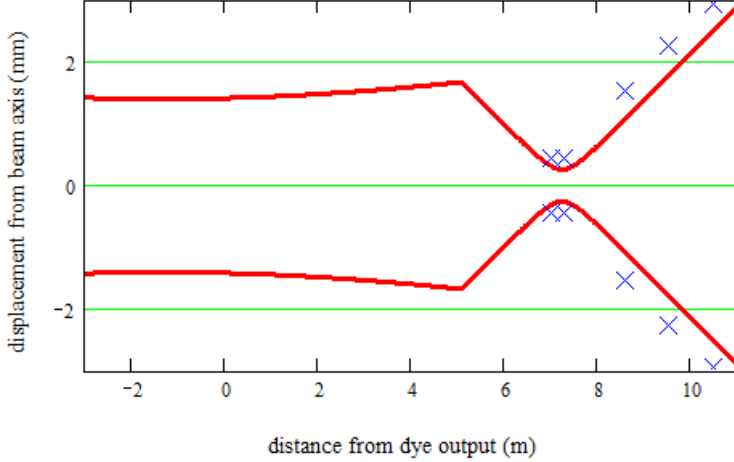


Figure 6.1: Dye laser output M^2 estimate. The solid lines show the $\frac{1}{e^2}$ width of the TEM00 mode, the x's are the data points from the Spiricon measurement. There were three measurements taken at the waist but only two are shown. The +2 m lens was placed at 5.075 m.

where L is the distance propagated. When transmitting through a thin lens, the q parameter obeys [67]

$$q' = \frac{q}{\frac{-q}{f} + 1} \quad (6.1.4)$$

where f is the focal length of the lens. The resulting hand fit implies the dye laser beam waist is 53 inches behind the output surface with $w_0 = 1.4$ mm when $\lambda = 628$ nm ($q = 1.346 + 9.808i$ in SI units). The Spiricon data imply the raw beam has a waist radius of $\omega_o = 439 \mu\text{m}$, with a far field divergence of $747 \mu\text{rad}$ (half the total divergence of the beam). Since [67]

$$M^2 = \frac{\theta\pi D}{\lambda}, \quad (6.1.5)$$

where θ is the far field divergence (half total divergence) and D is the waist (half width) of the raw laser beam; our estimate of M^2 is 1.6. See figure 6.1. One typical interpretation of M^2 is that it represents the number of modes present in the beam (technically in the x and y directions separately, but we have averaged the two together to simplify the results) so 1.6 may seem to imply near single mode operation with Gaussian transverse profiles; however, as we will see in Section 6.1.3 this is not the case.

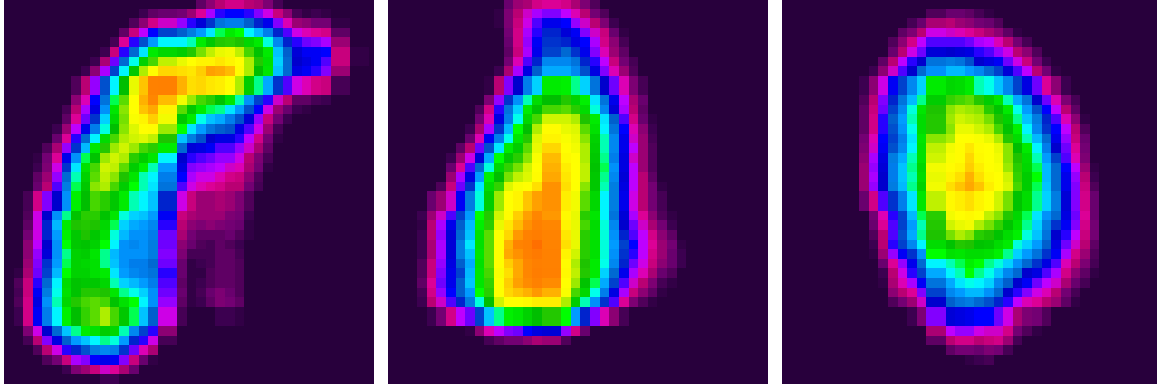


Figure 6.2: Transverse beam profiles from Spiricon camera. The center image was taken at the apparent waist (downstream from the 2 m lens), the left image was taken 12 inches downstream from the apparent waist, the right image was taken 12 inches upstream from the apparent waist.

6.1.3 Hermite-Gauss mode superposition

It was observed that the beam profile was asymmetric with respect to the upstream and downstream directions from the waist (see figure 6.2). As a check, we obtain a similar set of beam profiles using a superposition of the first 4 modes in the Hermite-Gauss expansion. The complex amplitude for the Hermite-Gauss beam is [76]

$$U_{\ell,m}(x, y, z) = A_{\ell,m} \cdot \frac{\sqrt{2}}{2^{m+\ell} m! \ell!} \cdot \frac{w_0}{w(z)} \cdot G_\ell \left(\frac{\sqrt{2}x}{w(z)} \right) \cdot G_m \left(\frac{\sqrt{2}y}{w(z)} \right) \cdot \Phi(x, y, z) \quad (6.1.6)$$

where

$$\Phi(x, y, z) = \exp \left(-ikz - ik \frac{x^2 + y^2}{2R(z)} + i(\ell + m + 1)\zeta(z) \right), \quad (6.1.7)$$

$$G_n(u) = H_n(u) \exp \left(\frac{-u^2}{2} \right), \quad n = 0, 1, 2 \dots, \quad (6.1.8)$$

$$\zeta(z) = \arctan \left(\frac{z}{z_0} \right), \quad (6.1.9)$$

$H_n(u)$ is the nth Hermite polynomial, and $A_{\ell,m}$ are the complex expansion coefficients.

It was found with some trial and error that the following set of expansion coefficients generated a composite beam which has a similar profile to the raw dye laser beam as

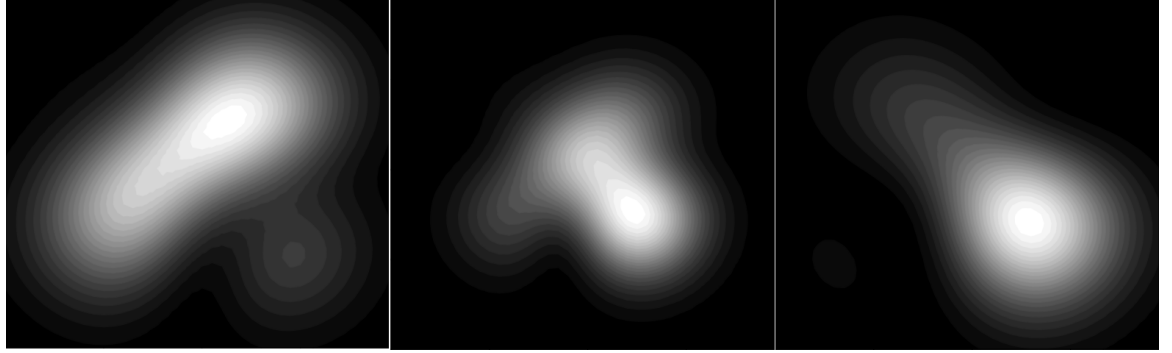


Figure 6.3: Superposition of the first four Hermite-Gauss modes. the left image is 0.3 m downstream from the waist, the center image is at the waist, the right image is 0.3 m upstream from the waist.

seen on the Spiricon camera:

$$A_{0,0} = 5 \exp(-i0.02\pi) \quad (6.1.10)$$

$$A_{0,1} = 1.4 \exp(i0.4\pi) \quad (6.1.11)$$

$$A_{1,0} = 1.8 \exp(i1.6\pi) \quad (6.1.12)$$

$$A_{1,1} = 1.5 \exp(i0.5\pi), \quad (6.1.13)$$

see figure 6.3. Thus, even though these results are consistent with $M^2 \sim 1-2$, we see that odd shaped non-uniform anti-symmetric beam profiles can result.

6.2 Dye laser output axial mode structure

The effects of the multi-mode nature of the dye laser output is observed and the RF intensity fluctuations recorded in the output of a square law detector. A RF receiver is used to spectrally analyze the detector output; and it is seen that many discrete spectral features exist out to the high frequency limit of the receiver. This measurement implies the dye laser runs multi-mode with as many as eight characteristic frequencies. Broad multi-mode laser output is not conducive to transition selection in the relatively dense energy structures of molecules.

6.2.1 Mode beating

The YAG-pumped dye laser system produces 8 ns pulses at 20 Hz - in the transform limit, these pulses should have a spectral width of 55 MHz. In fact, the manufacturer of the dye lasers claims the spectral width of each laser pulse to be 1 GHz with axial modes separated by 600 MHz. These specifications are assumed to not be base on measurement (they could not produce hard data), so we assume they arrived at these numbers through some calculation. For example, with a quick glance at the dye laser cavity, one can see that its approximate length is 30 cm. This corresponds to an axial mode spacing of 500 MHz which is consistent with the manufacture's claim.

If the dye laser output contains multiple longitudinal modes, this should show up as “beating” in the intensity profile. This can be seen by direct observation of the laser output on a square law detector using an oscilloscope; however, this method is usually limited by the bandwidth of the scope. For example, if the manufacture's claim is true and the dye laser output has 2 or 3 axial modes separated by 600 MHz, then we should see intensity beats at 600 MHz and 1200 MHz - this is beyond the bandwidth of typical oscilloscopes. However, when analyzed with a narrow band RF receiver, there should be 1 or 2 spectral features (in addition to the “DC” feature) at 600 MHz and 1200 MHz - well within the bandwidth of the RF receivers we have in the lab. See the discussion in Chapter 19 in reference [76].

6.2.2 Apparatus

The dye lasers used here are the Sirah Laser model PRSC-D-24 (dye #22 and dye #23) with the Lambda Lock feature. In addition to electrical power and computer control, these dye lasers require an external “pump” laser beam to run. The pump laser is the Continuum Powerlite Precision II Scientific Laser System: a Q-switched Nd:YAG laser running at the second harmonic (532 nm). The output of the YAG is split three ways and transported to the inputs of three dye lasers - the beam is stopped before the laser (dye #21) not being used. DCM dye, from Exciton, was dissolved in Methanol to produce the 628 nm beam used in this experiment. The resulting dye laser output has the following properties: linearly polarized (vertical), 20 Hz repetition rate, ~8 ns FWHM, and a pulse energy of about 58 mJ (38 mJ) for dye #22 (dye #23) at the laser output port.

The detector used here is the Hamamatsu R1193U-03 photodiode (S/N 903). The key characteristic is that it has a large active surface area: about 2 cm in diameter. Thus, since our beam is less than 0.5 cm in diameter, we can be sure that a majority of the beam is incident on the active portion of the photodiode to eliminate transverse mode beating [76]. Since only low light levels should be used with this photodiode, the signal from the photodiode was kept below 1 V (into $50\ \Omega$) even for low duty cycle laser output from the dye lasers. In this way we ensure there will be no damage to the large active area of the photodiode and its sensitivity will remain uniform over the entire area.

The Tektronix 7L14 and the 7L12 Spectrum Analyzers are both used here to process the signal from the photodiode. The key characteristics are their operating ranges: 1 kHz to 2.5 GHz for the 7L14 and 0.1 MHz to 1.8 GHz for the 7L12. For these data the largest resolution bandwidth, 3 MHz, is used. The output is designed to preserve Parseval's Theorem for RF electronic signals: mathematically, the output is the input's Fourier transform squared; i.e. the RF receiver's output voltage is proportional to the *square* of the input voltage. Thus, since the current from the photodiode is proportional to the incident intensity of the optical signal, the receiver's output is proportional to the *square* of the optical intensity. If a beam with a Gaussian intensity profile FWHM of σ_t is incident the photodiode, it can be shown that

$$\delta_\nu = \frac{\ln(16)}{\sqrt{2\pi}\sigma_t} \quad (6.2.1)$$

where δ_ν is the FWHM of the resulting spectral profile generated by the RF receiver. Compare this relationship to Equation 7.1.1.

To calibrate the scans, an accurate reading of the RF receiver center frequency must be acquired. The local oscillator output from the receiver is connected to a Tektronix TR 501 tracking generator. The generator produces a signal with a frequency identical to that of the receiver local oscillator. This signal is analyzed by a Hewlett Packard 53132A universal counter, thus the center frequency of the RF receiver can be directly observed on the counter readout. The tracking generator has a smaller operating range than the 7L14 receiver, however, and can only report accurately on frequencies less than 1.8 GHz. The calibration was linearly extrapolated for frequencies above 1.8 GHz for data taken with the 7L14.

The Stanford Research Systems SR250 Gated Integrator was used to temporally sample, amplify, and average the pulsed signal from the RF receivers. Even with a high pass

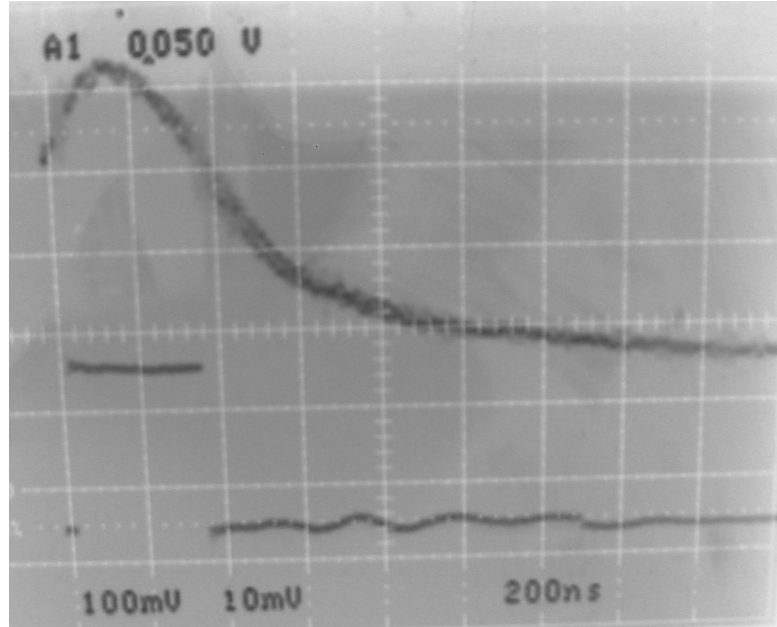


Figure 6.4: Boxcar gate placement for RF beat measurement. Channel one is the gate (lower trace, 100 mV/div), channel two is the receiver output (upper trace, 10 mV/div). This picture was taken with the receiver tuned to 50 MHz before we had the high pass filter, hence the large signal. Once the high pass filter was in place this “DC” signal was only \sim 15 mV. This signal was only used to place the gate - data was not taken this close to DC.

filter between the photodiode and the receiver, the output from the receiver above 150 MHz was buried in the noise. The boxcar averager was required to retrieve the signal from the usable range of each receiver. When the receiver’s center frequency is tuned down to about 130 MHz, a significant signal can be seen from the receiver (\sim 15 mV). This signal is used to place the boxcar gate. See Fig. 6.4 for a view of the oscilloscope during gate alignment. Once the gate is placed, appropriate gate widths, sensitivity settings, and sample numbers are selected. The boxcar gate is not temporally scanned in this experiment.

6.2.3 Photodiode calibration

This calibration procedure was motivated by a need to measure the radio frequency (RF) power spectrum distribution of the intensity profile of a pulsed dye laser’s output. When analyzing these data it is desirable to have the spectral response curve for the photodiode used to observe this intensity profile. Given this curve, we could compare

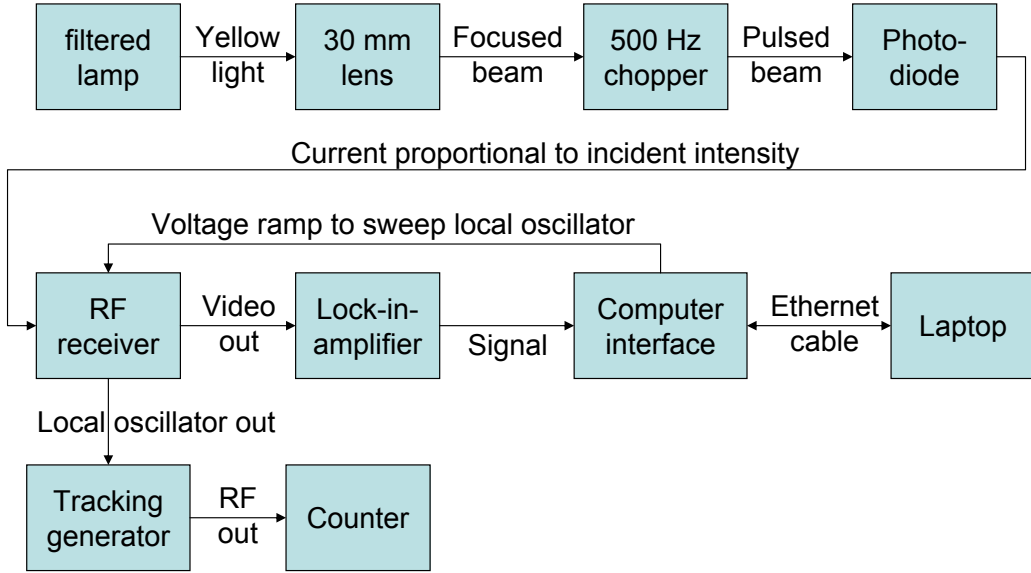


Figure 6.5: Photodiode calibration block diagram.

power amplitudes observed within spectral windows at various (differing) regions in the operating range of the photodiode. By exposing the photodiode to light with a white RF spectrum, we can directly measure this response curve using an RF receiver. Better yet, we may assume an equivalent circuit for the photodiode and fit the transfer function of this circuit to the RF receiver data; and thus obtain an analytic form for the response curve. This analytic form can be used to scale the raw data from the RF receiver/photodiode when measuring the RF spectrum of the dye laser output.

Suppose light from a hot filament is incident on a square law detector. If we assume the incident light originates at a black body source, it follows that the spectral power distribution is relatively flat in the radio frequency (RF) region - say from 100 MHz to 2 GHz. Thus, measuring the power within some small bandwidth across this RF region will reveal the transfer function of the photodiode and coupling circuit.

The light source in this experiment is a automotive style filament light bulb. The bulb was mounted in a desktop style lamp and plugged into a regular AC outlet. The switch on the lamp had three settings: “off” “low” and “high”; the “high” setting is used here. The bulb’s output is filtered through a yellow gelatin filter sheet (before being focused by a +30 mm lens) to limit the energy spread of the electrons emitted from the photocathode:

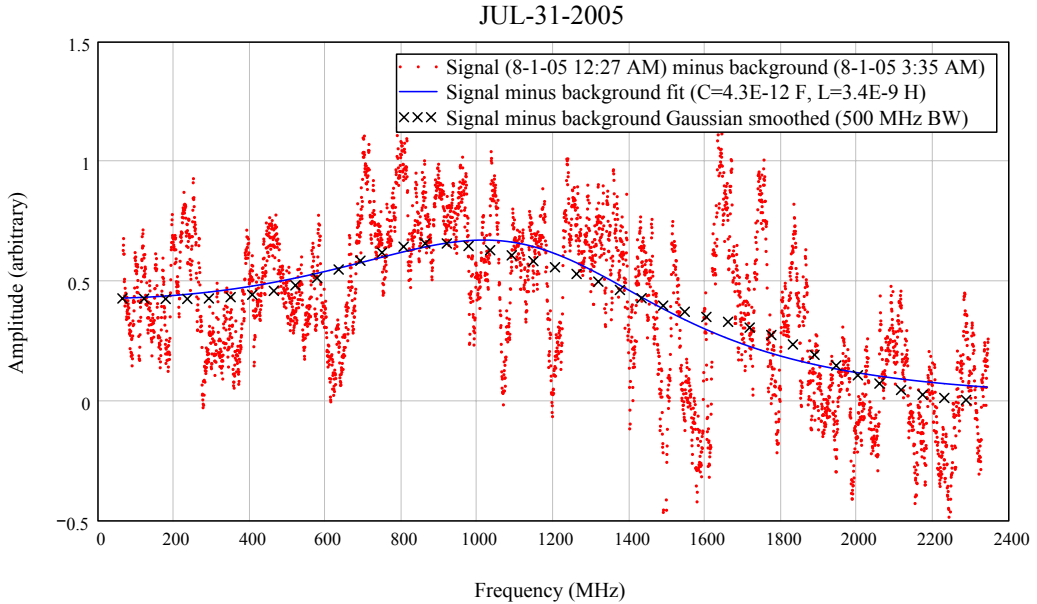


Figure 6.6: Photodiode calibration fit. The fit may be used to scale the output from the RF receiver/photodiode output to give realistic relative amplitudes over the operating range of the instrument

this will optimize the photodiode bandwidth by reducing transit time effect to a minimum. See Figure 6.5 for a block diagram of the calibration procedure.

The Hamamatsu R1193U-03 photodiode (S/N 878) is used here. Its key characteristics are its large active surface area (about 2 cm in diameter) and its fast response time. Some specifications from a reseller's site (Sphere Research Corporation) are: "High performance, bi-planar, ultra-fast phototube (270ps risetime, 100ps fall time) with integral light shield and lab housing (with tripod mount and connectors). UV sensitive, linearized for laser power detection, details coming from Hamamatsu, 2.5KV typical excitation."

The voltage-gain transfer function for the equivalent circuit of the photodiode and associated coupling circuit is (personal communication, John M. J. Madey, July 2005)

$$\frac{V_{out}}{V_{in}} = \frac{1}{1 + i\omega C(25 + i\omega L)} \quad (6.2.2)$$

where V_{out} is the voltage seen across the 50Ω external load resistor, V_{in} is the voltage across the capacitor (photodiode gap), C is the capacitance of this "gap", and L is the inductance associated to the photodiode. See Figure 6.6 for a plot of the data and the fit.

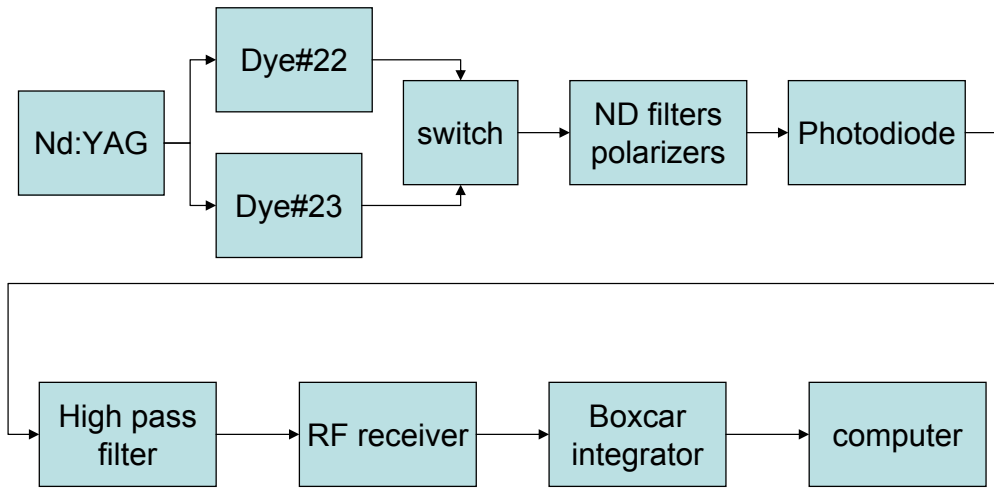


Figure 6.7: Block diagram RF beat spectrum measurement. The connection between the computer and the RF receiver (which carries the voltage ramp that scans the receiver) is not shown here.

6.2.4 Experiment layout

We measure the RF spectrum of two dye lasers (#22 and #23) using two receivers (the 7L12 and the 7L14). Selection between the two laser sources is facilitated through the use of a mirror mounted on a magnetic kinematic base (called the “switch” in Fig. 6.7). When the mirror is in place and the beam from dye #23 blocked, the beam from dye #22 is directed toward the photodiode. When the mirror is removed, the beam from dye #23 is incident on the photodiode. Switching between laser sources takes seconds. To attenuate the beam down to appropriate levels for the photodiode, the laser output is reflected off the front surface of a wedged quartz plate - the rear surface reflection is directed toward a beam dump while the front surface reflection is directed through two crossed polarizers and three neutral density filters (ND 0.3, 0.7, and 2.0). After the ND filters the beam is incident on the photodiode.

Before being analyzed by the receiver, the electronic signal from the photodiode is sent through a high pass filter (see Fig. 6.8 for the response curve for the filter). A 14 dB attenuator is placed between the photodiode and the filter to minimize back reflections from the filter (see Fig. 6.9 for the effect of the attenuator and filter on an actual pulsed signal from the photodiode). The SR250, triggered by the light scattered from the beam dump, gates and averages the receiver output. A laptop computer using the “voltage ramp

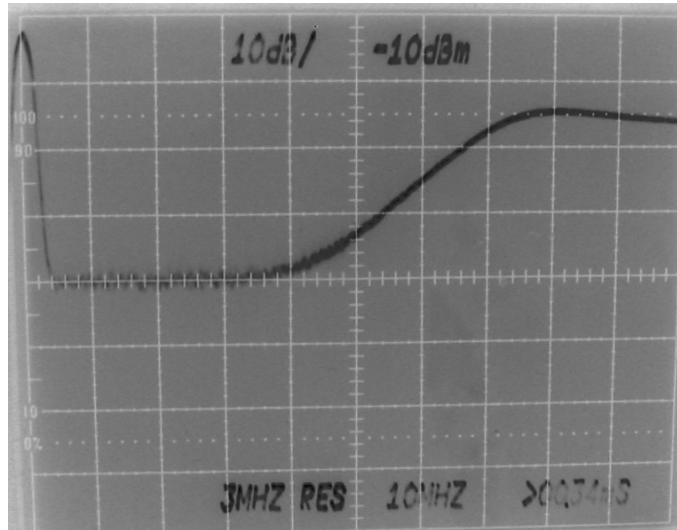


Figure 6.8: Highpass filter response. The output of the tracking generator was feedback into the RF receiver through the highpass filter while the receiver self-scanned. We see the filter begins to pass significant power at 50 MHz and reaches 100% transmission at 75 MHz.

chart recorder” LabView program (see AHI00-TP3300-01-VR03) simultaneously samples the boxcar integrator output and supplies a voltage ramp to the receiver. The voltage ramp scans the receiver across most of its usable range.

6.2.5 Data acquisition

Four data sets (1 hour each) are taken with the 7L12 receiver. First, dye laser #22 is scanned; next the beam is blocked for another 1 hour scan; then dye laser #23 is scanned; finally the YAG seeder is turned off and dye #23 is scanned again. Before each dye laser scan, the polarizers are adjusted so that the signal from the photodiode has an approximate amplitude of 100 mV. The 7L12 settings are as follows: amplifier set to its 5th notch, attenuator at 0 dB (together the amplifier and attenuator give a reference level of -70 dB), the video filter is active, FREQ SPAN/DIV is MAX (1.8 GHz), bandwidth 3 MHz, scale is linear (not log). The SR250 settings are as follows: gate width 300 ns, sensitivity 5 mV, samples 100. The computer settings are as follows: number of points acquired is set to 4000, the scan length is 3600 seconds, and the voltage ramp range is 0.5 - 10 volts.

Three data sets (1 hour each) are taken with the 7L14 receiver. First, dye laser #23 is scanned; next the beam is blocked for another 1 hour scan; finally dye laser #22 is

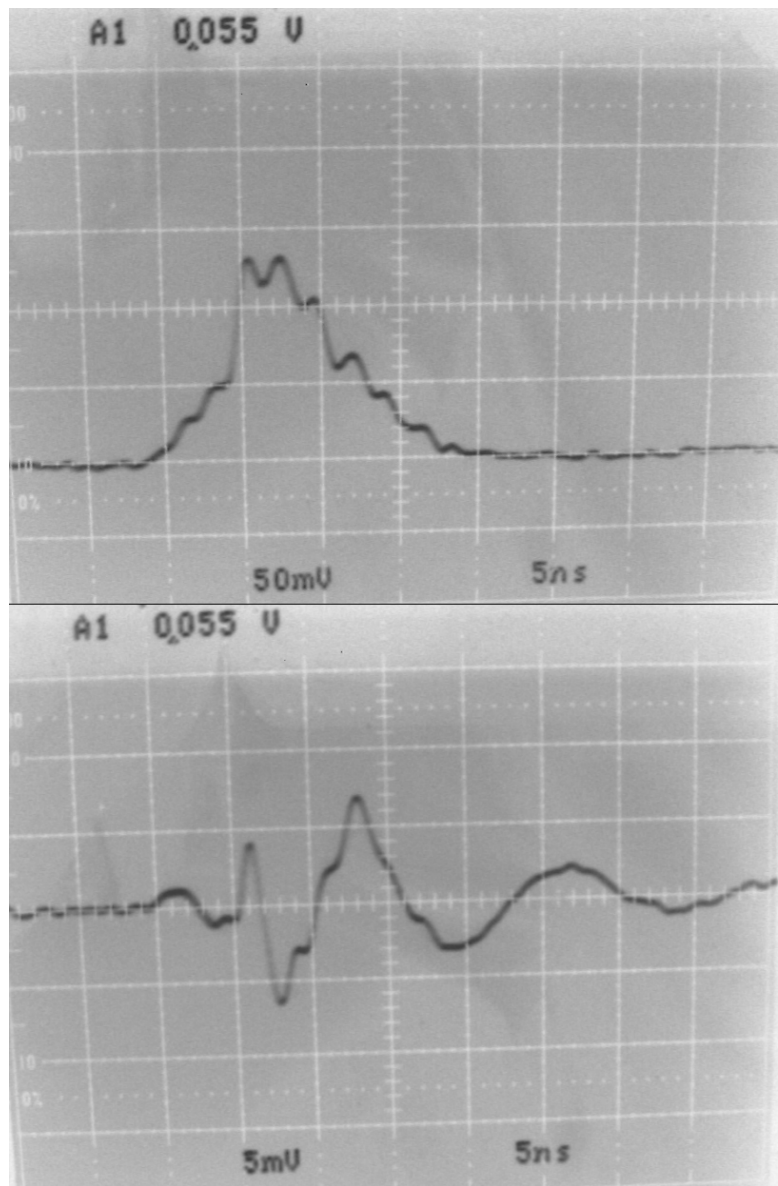


Figure 6.9: Photodiode signal through the highpass filter (and 14 dB attenuator). The upper photo shows a typical signal from the photodiode after a dye laser pulse is detected. The lower photo shows a typical signal after the insertion of the 14 dB attenuator and the highpass filter between the photodiode and the oscilloscope.

scanned. Before each dye laser scan, the polarizers are adjusted so that the signal from the photodiode has an approximate amplitude of 15 mV (the 7L14 is more sensitive than the 7L12). The 7L14 settings are as follows: amplifier set to its 5th notch, attenuator at 0 dB (together the amplifier and attenuator give a reference level of -70 dB), the video filter is active, FREQ SPAN/DIV is MAX (2.5 GHz), bandwidth 3 MHz, scale is linear (not log). The SR250 settings were not changed. On the computer the voltage ramp was changed to 0.9 - 10 volts.

6.2.6 Data analysis

First, the raw data sets are calibrated. The computer records the voltage sampled from the SR250 versus the associated voltage level sent to the receiver from the voltage ramp. The relationship between voltage sent to the receiver and the corresponding center frequency of the receiver is obtained by taking pictures of the laptop computer next to the HP 53132A counter. Each picture shows the current voltage on the voltage ramp (displayed on the laptop screen) and the current center frequency of the receiver. Several such pictures are taken during each scan. The relationship is found to be very linear, but shifts a little bit from scan to scan.

Once calibrated, each scan is scaled to compensate for the response curve of the photodiode (see AHI02-DN3300-5-VR08). Only one of the two photodiodes was calibrated (S/N 878) - here we use the one that wasn't calibrated and assume it has a similar response. See Figs. 6.10 and 6.11 to see the data for dye laser #22 taken with the 7L12 and 7L14 respectively. See Figs. 6.12 and 6.13 to see the data for dye laser #23 taken with the 7L12 and 7L14 respectively. The following overlays are of the raw data - calibrated but not scaled for the photodiode response. Figs. 6.14 and 6.15 show overlays of the data from the two lasers taken with the 7L12 and 7L14 respectively. Fig. 6.16 shows an overlay of the data from dye laser #23 with the YAG pump in two states: seeder on and seeder off.

Finally, to check the spectral width of the observed features, the peak at 1200 MHz from the 7L12 scan of the #23 dye laser is fit to a Gaussian (see Fig. 6.17). Using the FWHM from the fit, Eqn. 6.2.1 is used to determine the corresponding transform limited temporal width.

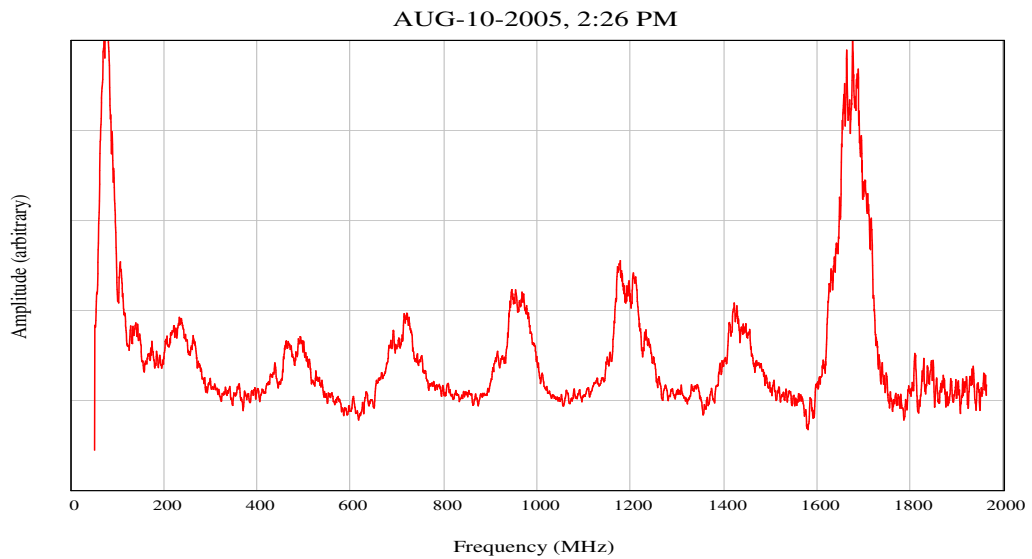


Figure 6.10: Dye laser #22 scanned with the 7L12

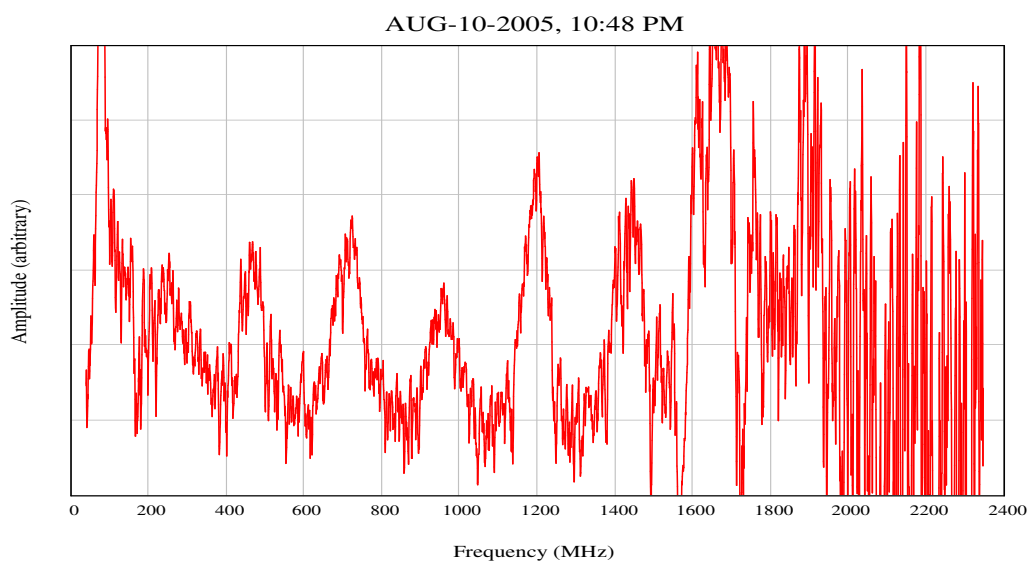


Figure 6.11: Dye laser #22 scanned with the 7L14

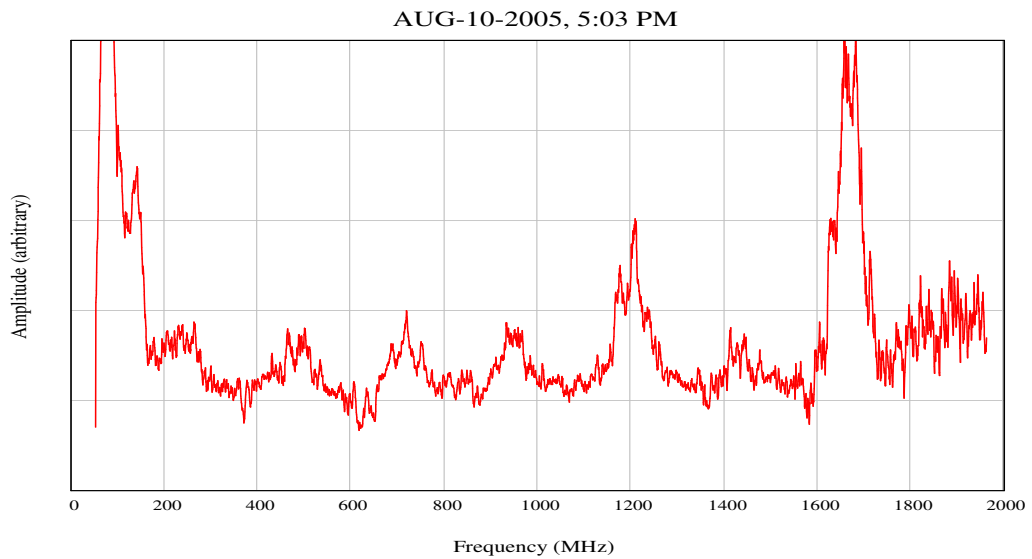


Figure 6.12: Dye laser #23 scanned with the 7L12

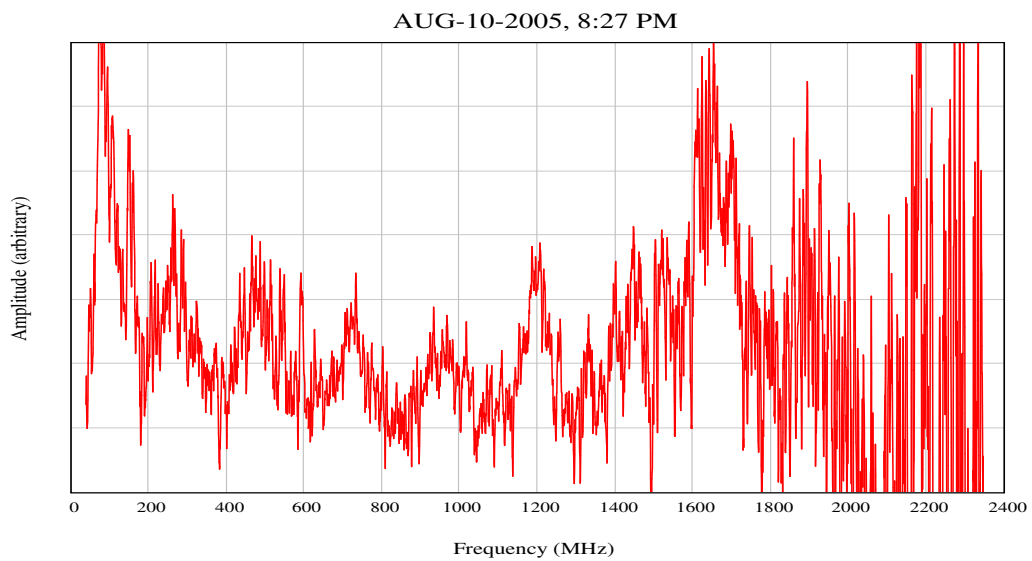


Figure 6.13: Dye laser #23 scanned with the 7L14

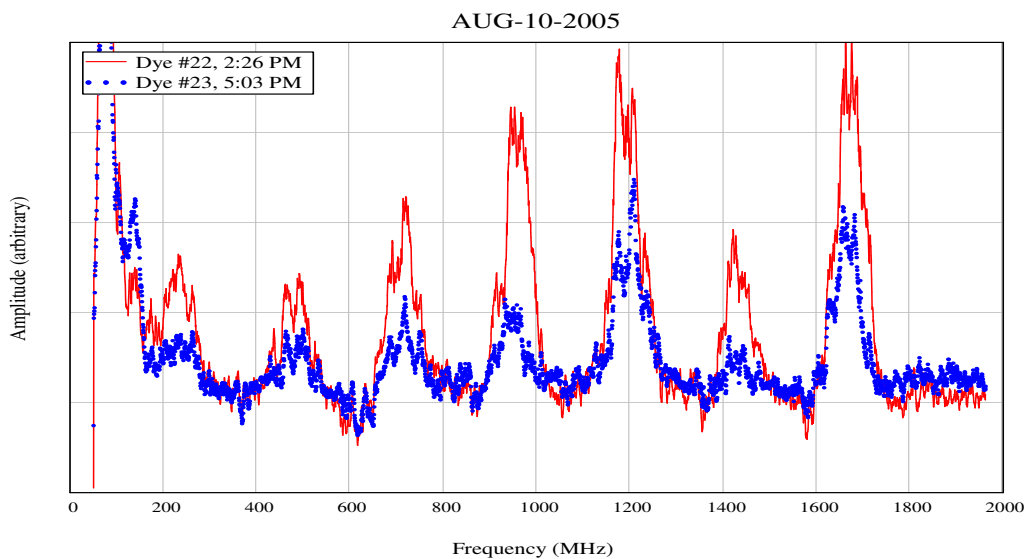


Figure 6.14: Both dye lasers scanned with the 7L12 (raw data)

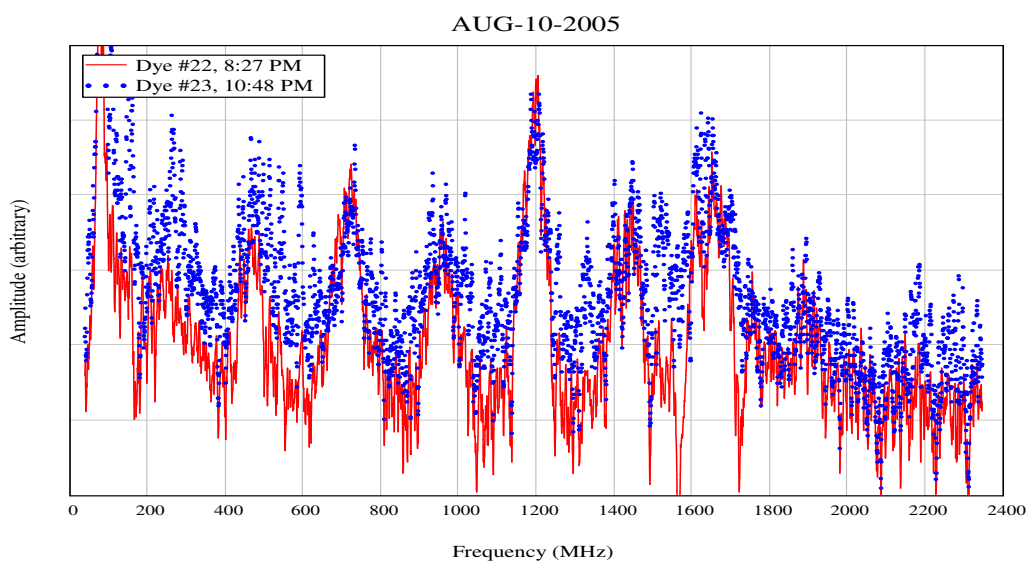


Figure 6.15: Both dye lasers scanned with the 7L14 (raw data)

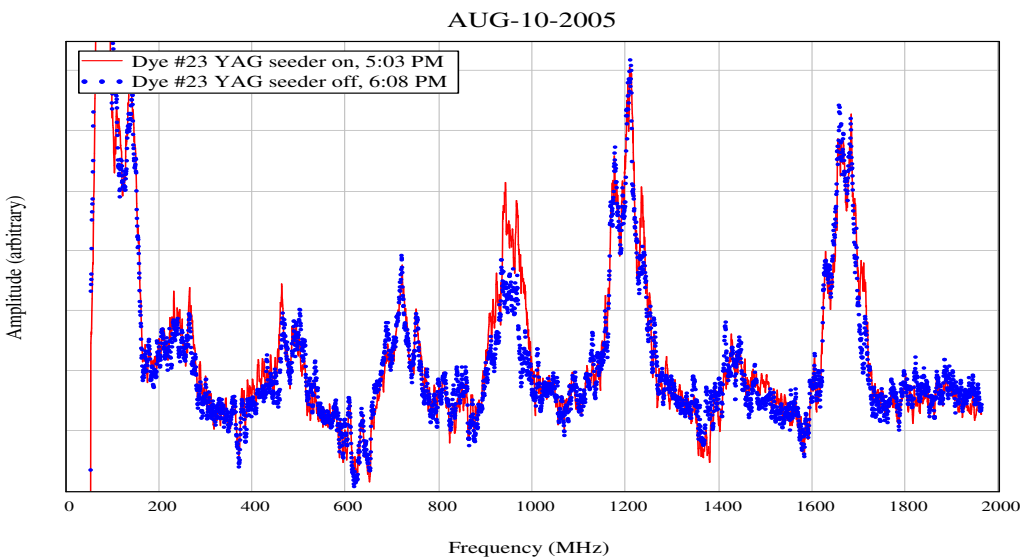


Figure 6.16: Dye laser # 23, with YAG pump with the seeder on/off, scanned with the 7L12 (raw data)

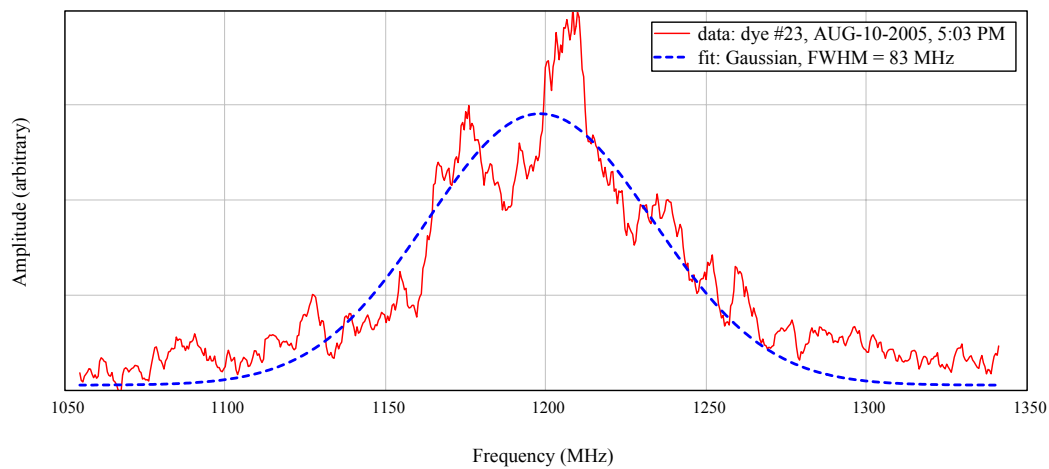


Figure 6.17: The spectral feature at 1200 MHz fits a Gaussian with a FWHM of 83 MHz. This corresponds to a Gaussian in the time domain with a FWHM of 7.5 ns. This matches the observed pulse width - implying each mode is transform limited.

6.3 Conclusion

A series of measurements have shown the dye laser to be a multi-mode source. The transverse mode content is revealed using CCD images of the transverse profile of the dye laser output. A RF receiver has exposed multiple discrete spectral features in the beat spectrum of the intensity profile of the pulses which are interpreted as the result of interference between axial modes with 240 MHz spacing. Given the length of the cavity (about 30 cm), this spacing is consistent with the mode spectrum of a *confocal* cavity [76].

The results in this chapter imply that before embarking on an exploratory program of coherent molecular control processes the dye laser output must be conditioned if we choose to leave the dye laser system intact. [19] details an effort to generate dye laser output for use in a coherent control experiment; but at the cost of power and tuning range. There may be fundamental issues keeping the possibility of broad tunability, high peak power, and mode purity out of the question for systems based on fluorescent dye.

Chapter 7

Issues for the Design and Operation of Multicolor Dye Laser Systems

7.1 General description

Armed with the information from the previous chapters, we outline methods employed to condition the dye laser system for coherent control spectroscopy. This section introduces the systems used to condition a single dye laser, then outlines the method of mixing and delaying the pulses, and finally gives a brief description of the interaction region and the data acquisition chain.

7.1.1 Single dye laser conditioning

It has become clear that the main issue one must deal with to prepare a commercial dye laser for use in a multi-color coherent control experiment is the multi-mode nature of these sources. The processes under investigation demand transform limited pulses [19] and well controlled intensity profiles. The raw output of each of the three dye lasers is unusable since it is not transform limited, has non-Gaussian anti-symmetric transverse intensity profiles (M^2 not close to unity), and cannot be arbitrarily delayed with respect to the pump laser. To condition each beam for use in the experiment, we temporally condition the pulse into a Gaussian shape, run the pulse through a variable delay line, spatially filter

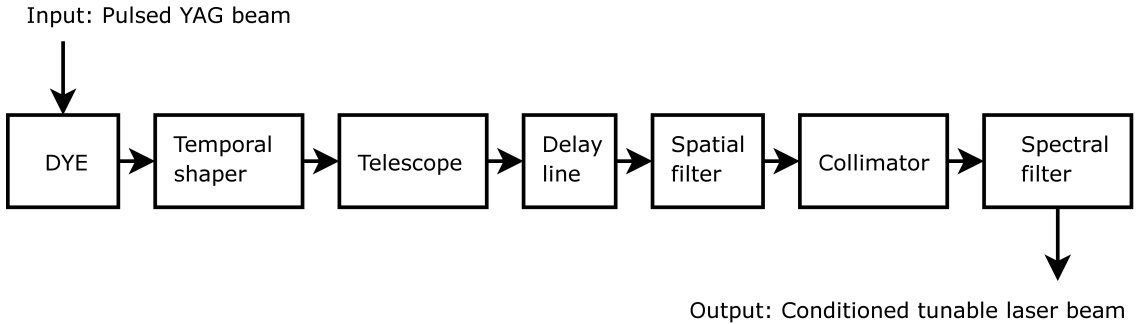


Figure 7.1: Single dye laser conditioning block diagram

the beam to eliminate the non-TEM00 transverse modes ($M^2 \sim 1$), then spectrally filter the pulse to its transform limit (see figure 7.1).

The temporal shaper is a Pockels cell (the Pockels cell will also be used to set the amplitude of each pulse). It has been shown in the lab that the Pockels cell can create dye laser pulses with widths from 0.8 ns to 4.4 ns. The lower limit is a characteristic of the Pockels cell and its associated electronics; the upper limit is roughly the longest pulse we are able to generate when we eliminate the ragged leading and trailing edges of the raw laser output. For transform limited shapes (Gaussians), the temporal FWHM of the intensity is related to the spectral FWHM of the power spectrum by

$$\sigma_\nu = \frac{\ln(16)}{2\pi\sigma_t}, \quad (7.1.1)$$

where σ_ν is the spectral FWHM and σ_t is the temporal FWHM.

Thus, if σ_t is 0.8 ns then σ_ν is 552 MHz, and if σ_t is 4.4 ns then σ_ν is 100 MHz. These are the target spectral filter widths for long and short pulse experiments. The spectral filters are etalons with a FSR big enough to prevent aliasing and a mode width of 100 MHz to 552 MHz depending on the type of experiment.

The delay line extends the path length of the beam in such a manner to allow arbitrary delay between the dye laser pulse and YAG pump. A telescope is used upstream from the delay line to minimize the effect of the variable path length between the dye laser output and the spatial filter. The spatial filter is placed downstream from the delay line and shall consist of a focusing lens and a pinhole. The central maximum from the pinhole (Airy function) is mode matched into the etalon (beam is collimated if a planar configuration is

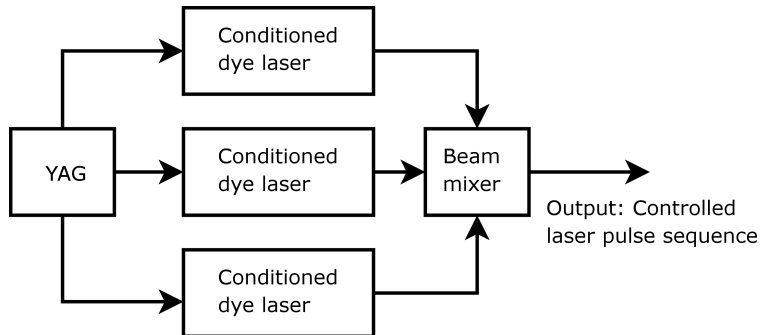


Figure 7.2: Three conditioned and synchronized dye lasers block diagram

used - or focused if confocal). Then the beam is finally collimated (if necessary) and sent to the molecular interaction region.

7.1.2 Controlled three pulse sequence

The experiment requires three properly conditioned pulses, all incident upon the same spatial region, sequenced in a specific temporal order. A single Nd:YAG pulsed dye laser is used to simultaneously pump three dye lasers; thus the relative delay between each dye laser is fixed. We will obtain arbitrary control of the pulse sequence by delaying two pulses with respect to the third. By manipulating the beam line design, we can force all three pulses to be temporally coincident while the delay lines are in their middle positions. In this way each of the two delayed pulses can be retarded or advanced by 4 ns with respect to the un-delayed pulse. We can even swap dye cells between dye lasers for complete control of the color order in the pulse sequence.

Once the pulses are properly delayed and ordered, they are aligned in a “beam mixer” so that their optical axes are collinear. The final output of the laser system is a three color transform limited pulse sequence with user specified color triple, amplitude triple, and relative delay of the pulses within the sequence. We use a 50/50 beam splitter as the beam mixer. Since we do not yet know the optimal color sequence, in the initial stages of this experiment, we will use broadband 50/50 beam splitters as we explore different color sets. Once the optimal color sequence is set, then more efficient optics could be specified if required. See figure 7.2.

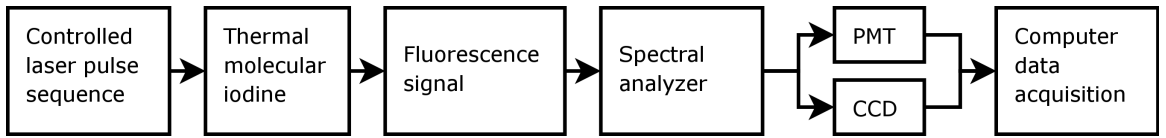


Figure 7.3: Interaction and data acquisition block diagram

7.1.3 Interaction and data acquisition

The collimated output of the three dye laser system is incident on a controlled sample of thermal molecular iodine. A circular aperture is placed immediately upstream from the sample to approximate a top hat spatial field in the interaction region. Initially, the sample is pure molecular iodine vapor at various concentrations - i.e., low buffer gas pressure. Once the various coherent processes of interest are verified (proof of concept), a buffer gas is introduced at various concentrations to measure the noise suppression limit of each of the coherent processes (efficiency).

The fluorescence signal from the interaction region is imaged onto the input slit of the monochromator by a lens system. The output of the monochromator may be read by either a CCD array (good for initial exploring and verification) or a PMT (temporally resolved and gated). The CCD image is directly downloaded into a PC for processing. The PMT signal is gated, amplified, and averaged (if necessary) in a gated boxcar averager system; the output of the boxcar system may then be read by either a chart recorder or a ADC equipped PC for processing. See figure 7.3.

7.2 Layout

The entire system will span three optical tables: the laser beams start on the “dye laser” table, proceed to a “conditioning” table, then finally reach an “interaction” table. This section gives the precise layout of the key optical components (here we assume a pinhole will be used for completeness).

7.2.1 Dye laser table

We specify the position of the lasers on the dye laser table with respect to the output port and output surface (measured from the edge holes) of each laser. The YAG has three output ports; we will use the middle port for this experiment. The dye lasers have

two ports - and input and output port. The output port is on the right if you are facing the front of the laser. The tolerance for these positions is $\pm \frac{1}{8}$ inch. See figure 7.4.

The output from the Nd:YAG is split into three equal parts and sent to the input ports of each dye laser. First the beam is sent through a beam splitter that transmits two thirds of the incident beam power and reflects the remaining third. The transmitted beam is then sent through a beam splitter that transmits half and reflects half the incident beam power. In this way, we pump each dye laser with equal power allowing the most flexibility when exploring different pulse sequences. See figure 7.5

The output from each dye laser is conditioned with respect to polarization and amplitude before it leaves the dye laser table. This is mainly for safety reasons, but also has the added advantage of localizing the Pockels cell system, along with its associated fast high voltage electronics, far from the data acquisition region of the experiment. The relative delay between each beam is adjusted on the dye laser table to allow for a convenient beam line on the next two tables. See figure 7.6.

The Pockels cell system consists of a pile-of-plates polarizer, a Pockels cell, then a Brewster plate. The output of the pile-of-plates will be highly polarized in the horizontal direction. When switched, the Pockels cell will rotate this horizontal polarization toward the vertical by a specified amount. The Brewster plate will then output a sample of the vertical component of this beam. In this way we produce a vertically polarized output beam with continuously selectable pulse energy. See figure 7.11

7.2.2 Beam conditioning table

On the conditioning table we delay and spatially filter the three dye laser beams. The delay line is a rail with a sliding “car” which the user moves by hand. With the beam line folded four times, we can achieve delays of ± 8 ns using a 4 foot rail. It will only be necessary to delay two of the beams (dye lasers #22 and #23) to generate arbitrary pulse sequences with internal delays less than 8 ns. After the beams are synchronized, we spatially filter each beam using a pinhole. The filter consists of a focusing lens, high damage threshold pinhole, and a collimating lens to capture the usable portion of the pinhole output. See figure 7.8.

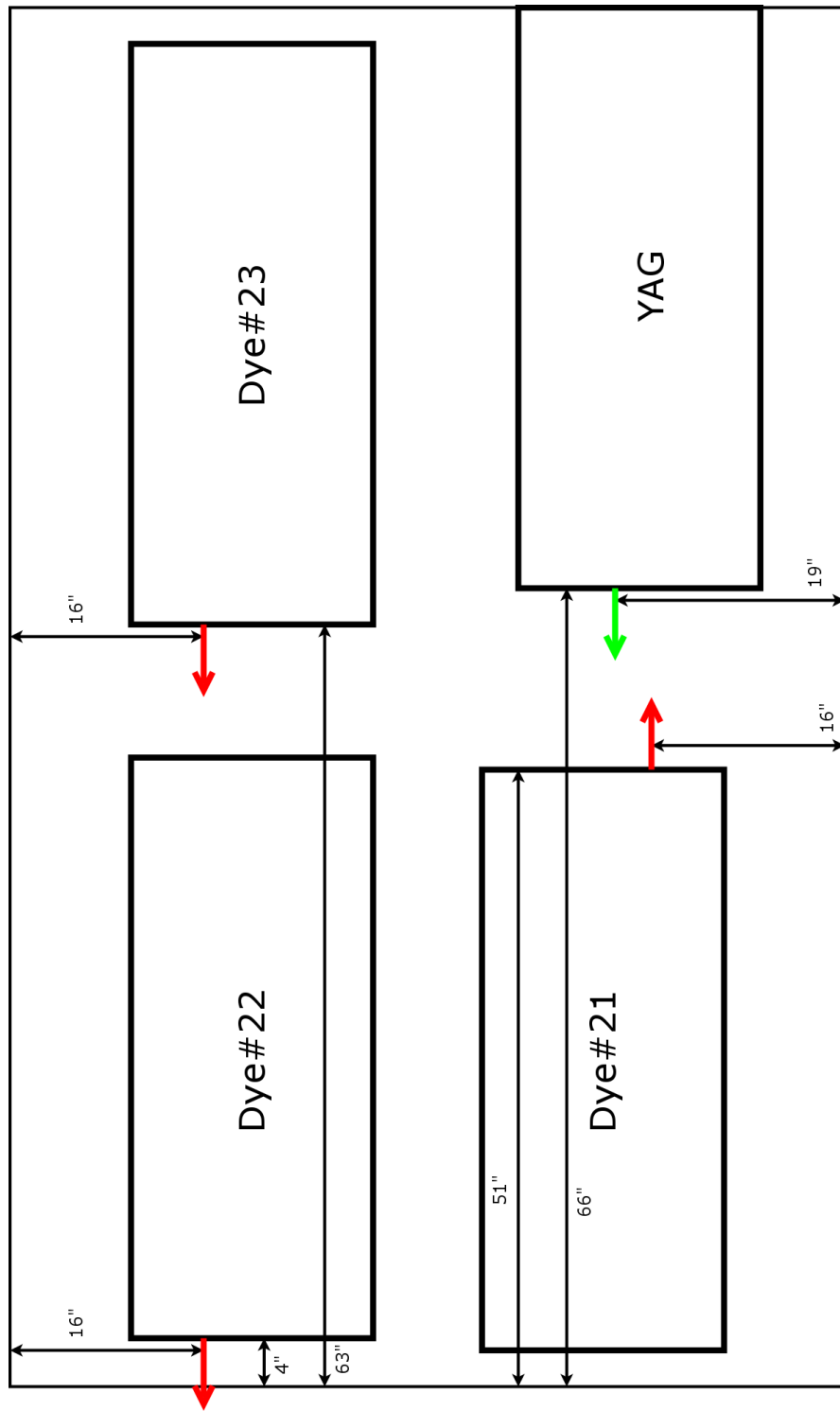


Figure 7.4: Laser positions on dye laser table. The outside border of the diagram (i.e., the reference edge for all dimensions) is the line defined by the last column (or row) of 1/4-20 tapped holes on the optical bench (NOT the actual edge of the table).

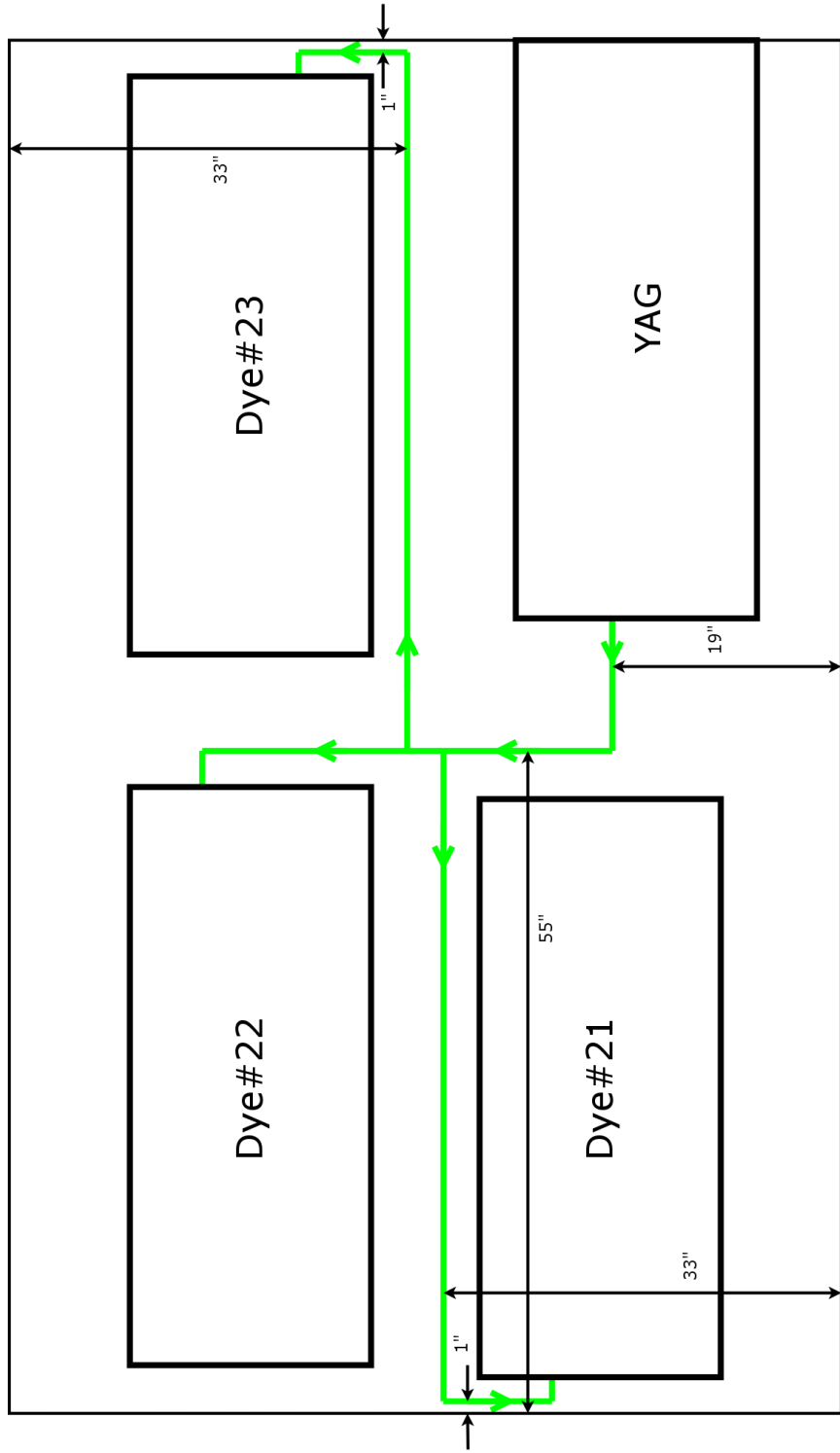


Figure 7.5: YAG beam positions

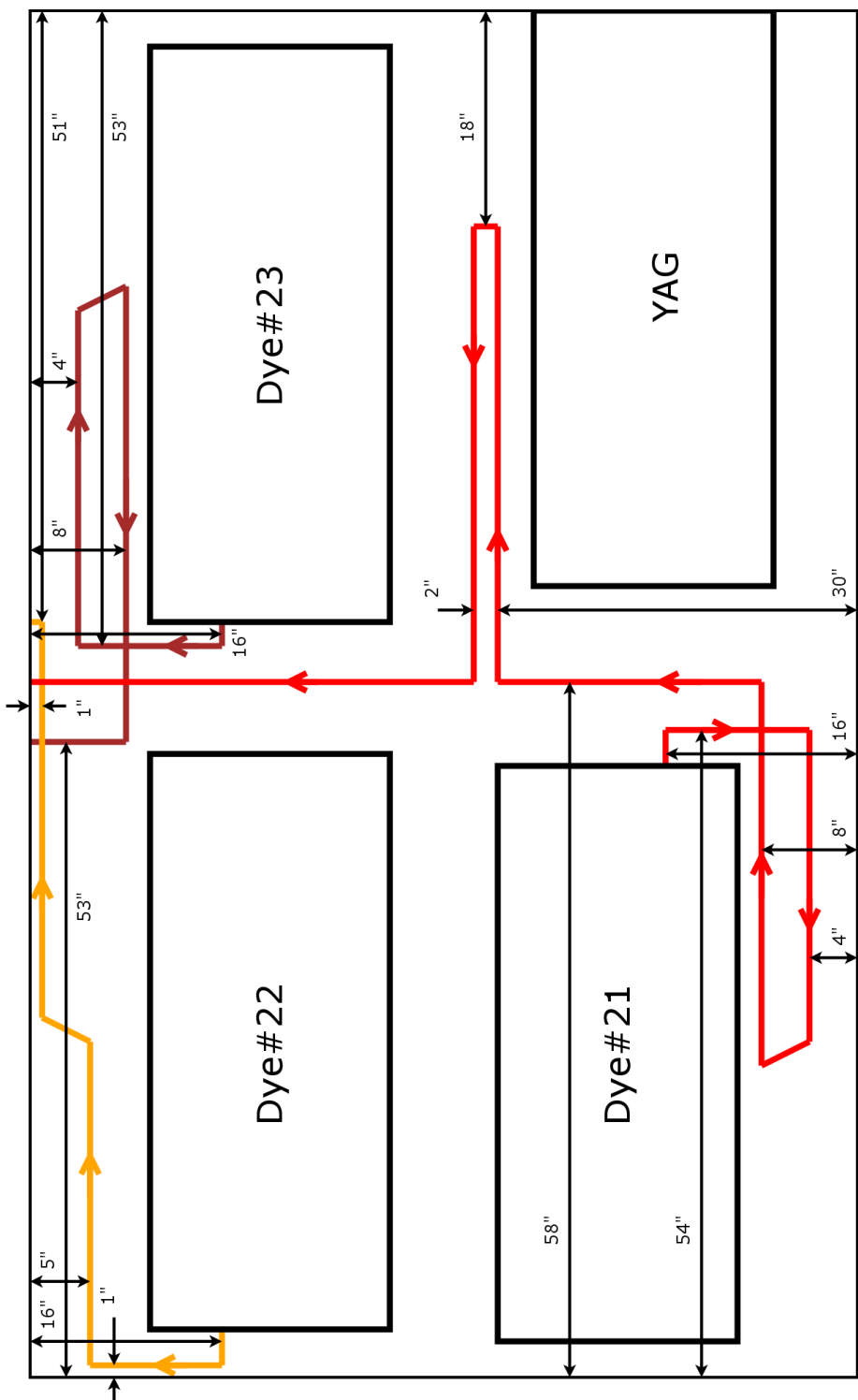


Figure 7.6: Dye beam positions

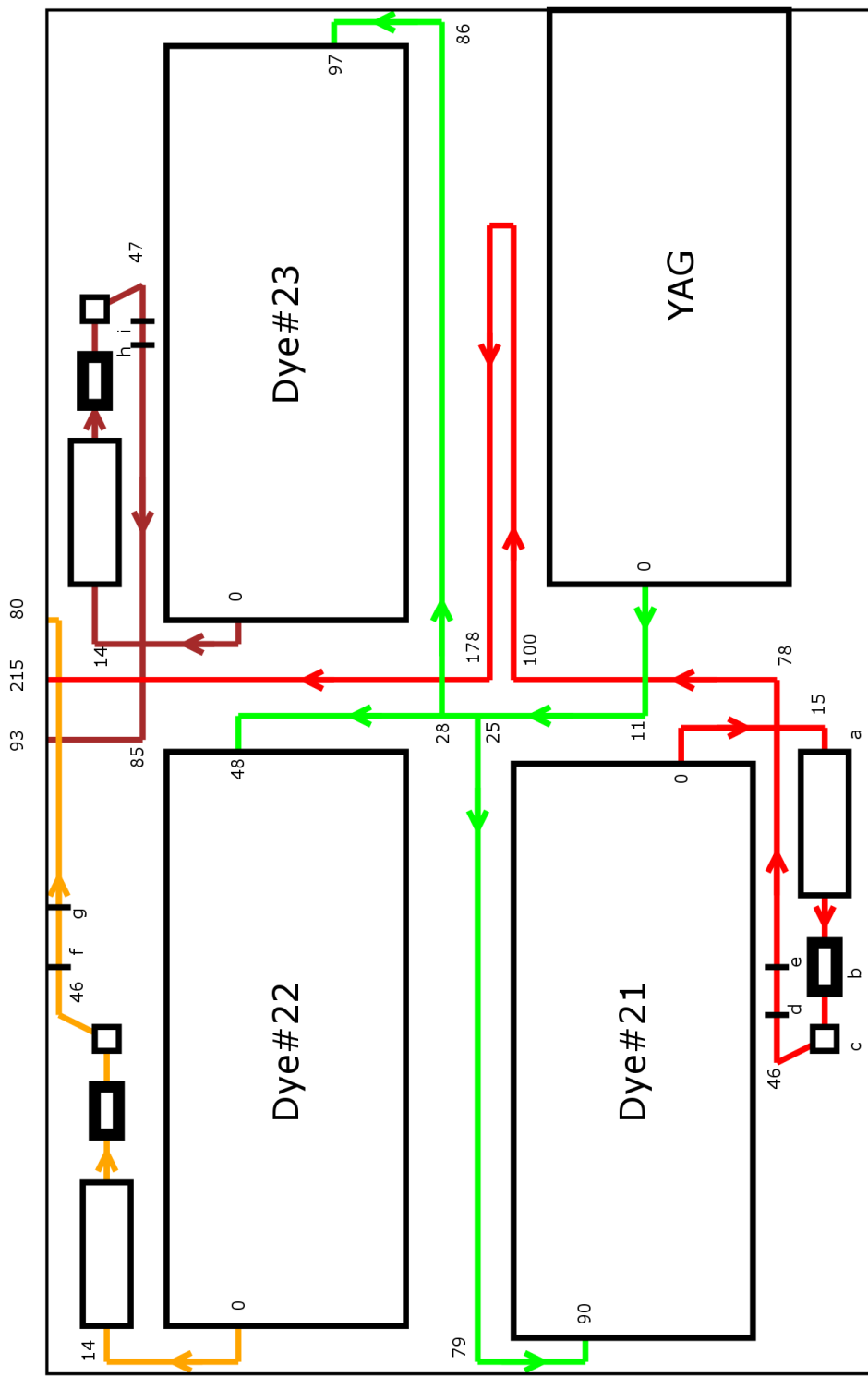


Figure 7.7: Beam mileposts and optics on the dye laser table. the mileposts along each beam line is given in inches. Optic (a) is a pile-of-plates polarizer; (b) Pockels cell, (c) Brewster plate, (d) +1 m lens at mile post 50, (e) -1 m lens at milepost 54, (f) +1 m lens at milepost 50, (g) -1 m lens at milepost 55, (h) +1 m lens at milepost 50, (i) -1 m lens at milepost 52.5.

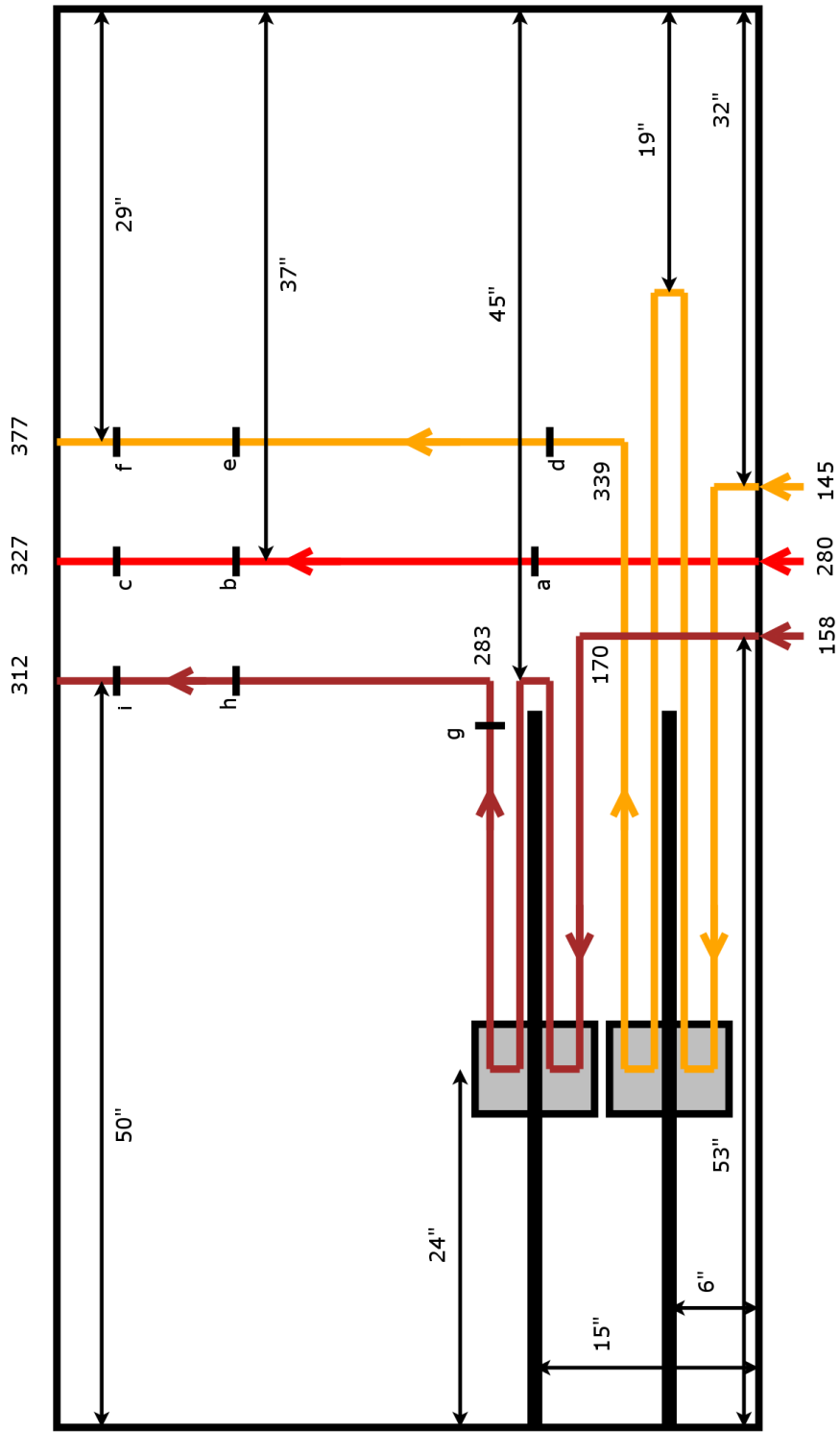


Figure 7.8: Beam conditioning table. (a) is a +0.5 m lens at milepost 315.3, (c) is a +0.2 m lens at milepost 323.2, (d) is a +0.5 m lens at milepost 344, (e) is a +0.2 m lens at milepost 372.5, (g) is a +0.5 m lens at milepost 280, (h) is a pinhole at milepost 300.3, and (i) is a +0.2 m lens at milepost 308.2. The delay lines are shown as horizontal black bars; the delay “cars” (in the zero delay position) are shown as gray rectangles.

7.2.3 Interaction table

The interaction table begins with the final stage of conditioning: spectral filtering. The spectral filter is an etalon with a FSR < 3GHz (to prevent aliasing) and mode widths ranging from 100 MHz (for long pulse experiments) to 552 MHz (for short pulse experiments). The beam line presented here assumes planar etalons - some redesign will be required if confocal etalons are used. See figure 7.9.

The three dye laser beams are then mixed using beam splitters. Once the beam are collinear, they are incident upon a pinhole placed just upstream from the iodine cell. Pick-offs are placed before the beams splitters to sample each input beam. Energy detectors are placed downstream from the pick-offs so that they are at the same beam milepost as the iodine cell. Duplicate pinholes are placed upstream from each detector; identical to the iodine cell's pinhole. Figure 7.10 shows the beam positions required.

In figure 7.9 we see that the beam from dye laser #21 traveled 413 inches to reach the energy detector labeled (e) in the figure. This is the same distance the beam travels to reach the iodine cell labeled (m). If we add the distance the YAG beam traveled to pump dye laser #21 we obtain 503 inches. It can be shown using figures 7.11 and 7.9 that the other two dye lasers have this same sum. Thus, assuming the path lengths inside each dye laser is the same, we conclude the three pulses arrive at the iodine cell (and the energy detectors) simultaneously.

7.3 Filters

There are three filters under consideration: a temporal shaper, a spatial filter, and a band pass spectral filter. The filter with the most development history is the temporal shaper: the Pockels cell. The pinhole is analyzed here in terms of its effectiveness as a spatial filter for high peak power pulsed control experiments. A fundamental limitation on the transmitted power of etalon type filters is parameterized – this brings into question the rationale for using etalons when beam energy is important to the experiment. Finally we present the results of a test of a confocal etalon purchased for evaluation purposes.

7.3.1 Pockels cells DC test

Here we describe a test to determine a basic performance parameter of the Pockels cell: the applied voltage at which a beam passing through the cell will experience a 90 degree

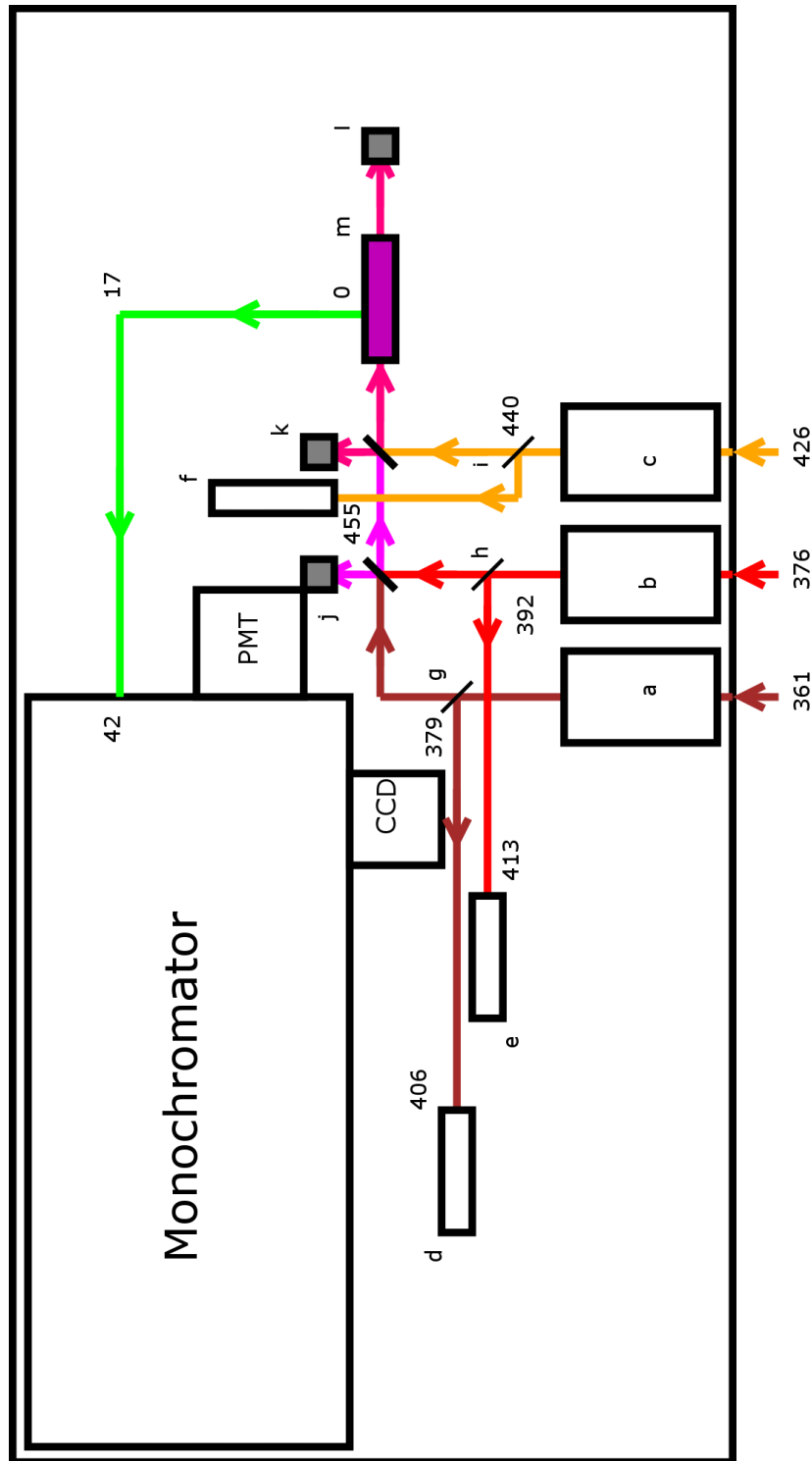


Figure 7.9: Interaction table beam mileposts and optical component labels. There is a 6X8 inch foot print for the etalons (a), (b), and (c). (d),(e), and (f) are the energy meters and pinholes for each beam. (g) is a pick-off placed at milepost 379 along the beam from dye laser #23 - similarly for (h) and (i). (j), (k), and (l) are beam dumps and (m) is the iodine cell and its pinhole.

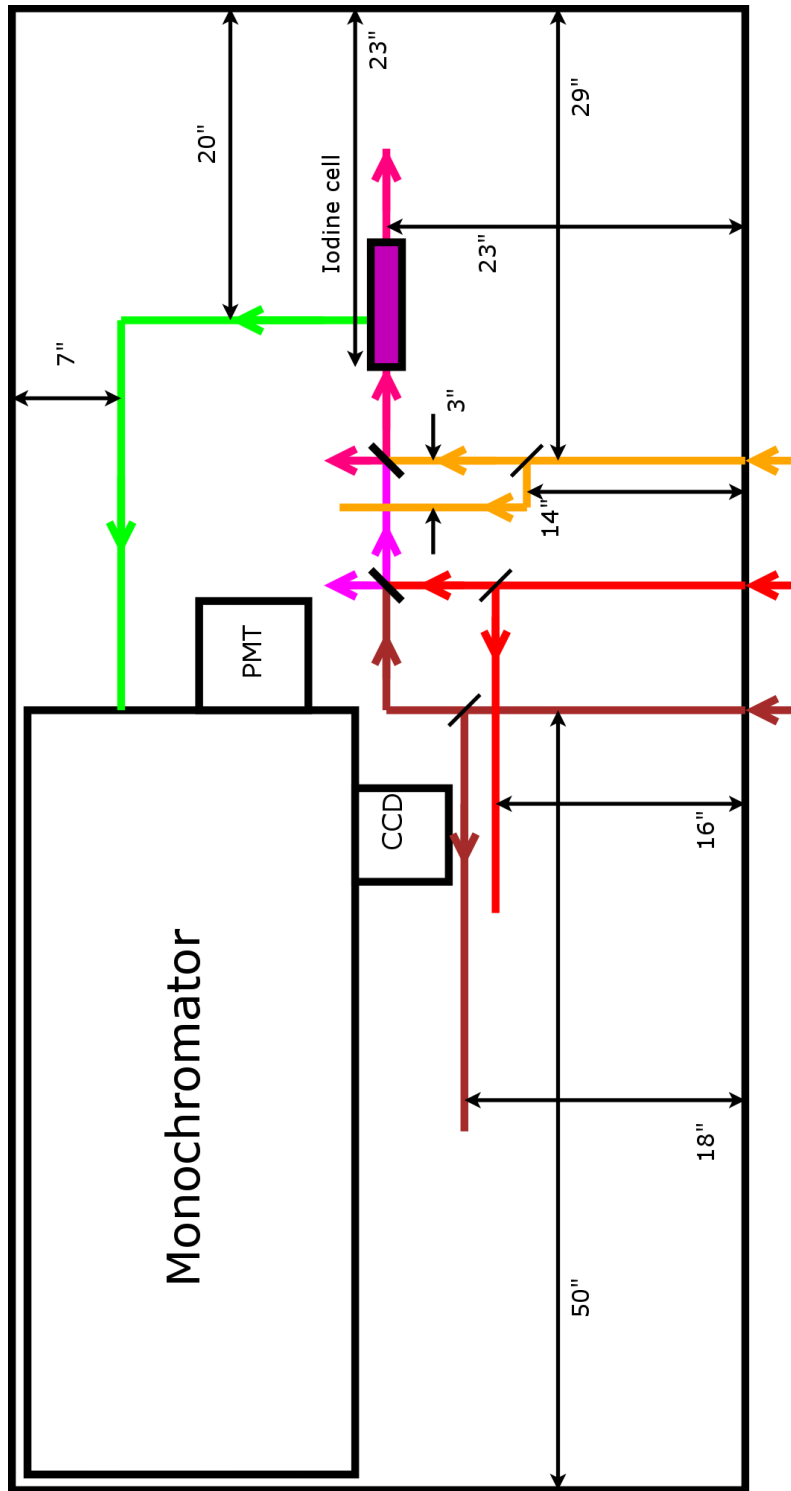


Figure 7.10: Interaction table beam positions. The mixed beams are shown in light pink and dark pink, the green beam is the fluorescence signal.

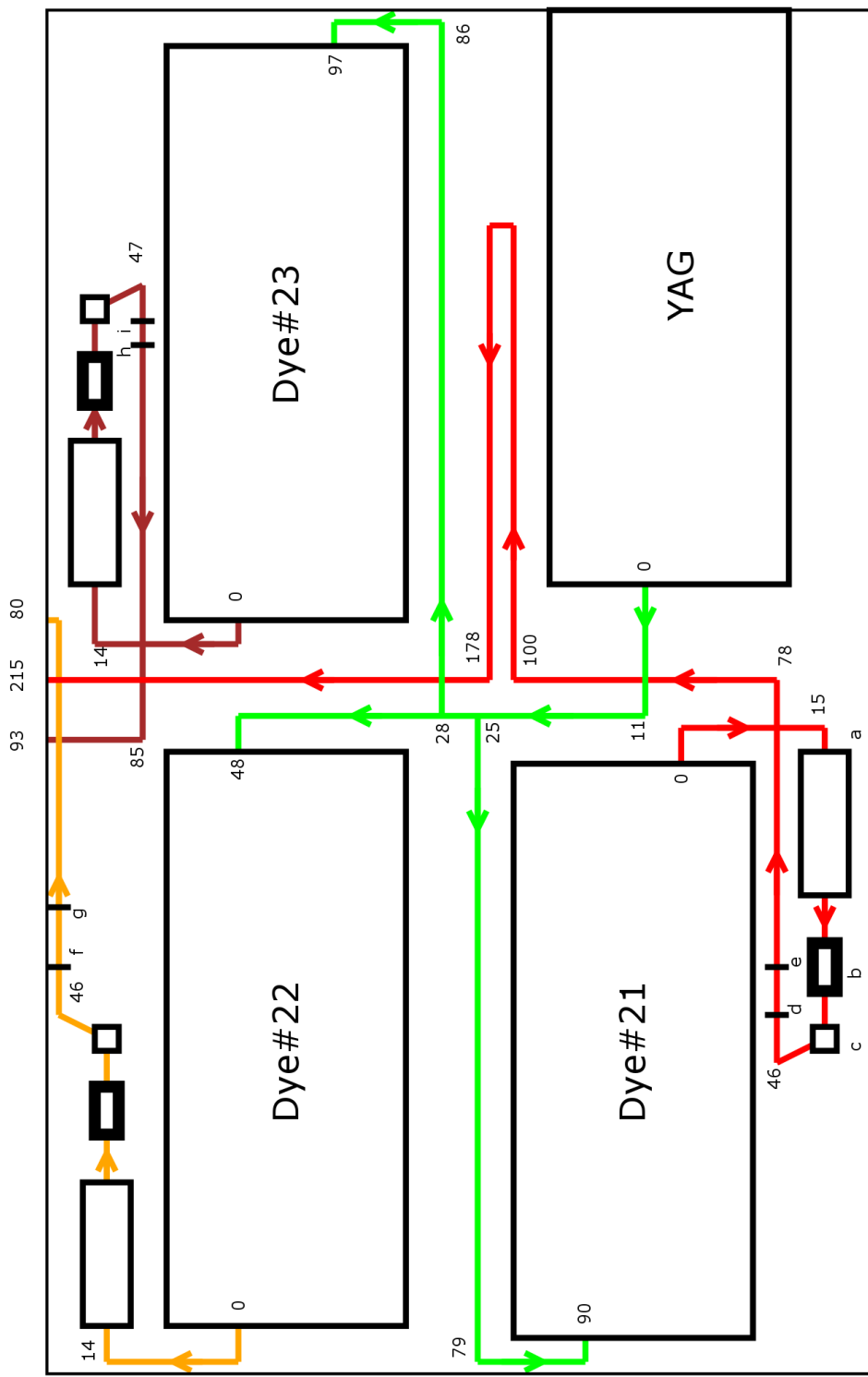


Figure 7.11: Beam mileposts and optics on the dye laser table. the mileposts along each beam line is given in inches. Optic (a) is a pile-of-plates polarizer; (b) Pockels cell, (c) Brewster plate, (d) +1 m lens at mile post 50, (e) -1 m lens at milepost 54, (f) +1 m lens at milepost 50, (g) -1 m lens at milepost 55, (h) +1 m lens at milepost 50, (i) -1 m lens at milepost 52.5.

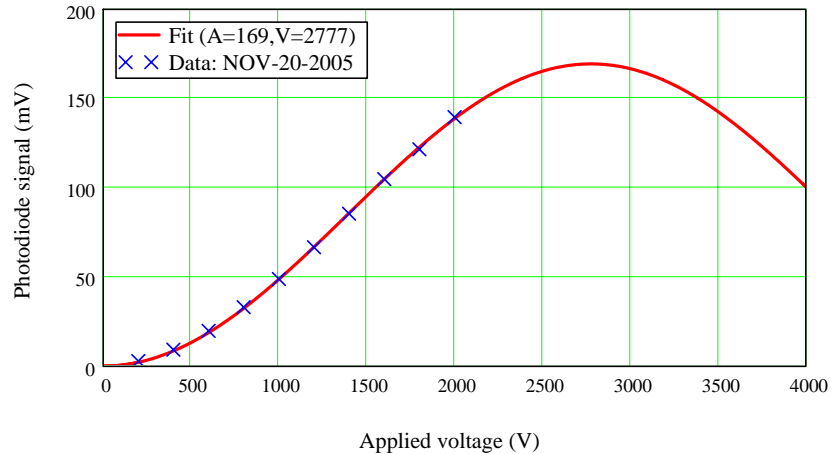


Figure 7.12: DC test of 628nm coated Pockels cell. A base line photodiode reading (with the crossed polarizers and Pockels cell removed) was not recorded for these data; however, we expect the efficiency to be better than the green case in Figure 7.13 since the laser wavelength of 633nm is closer to AR coating wavelength.

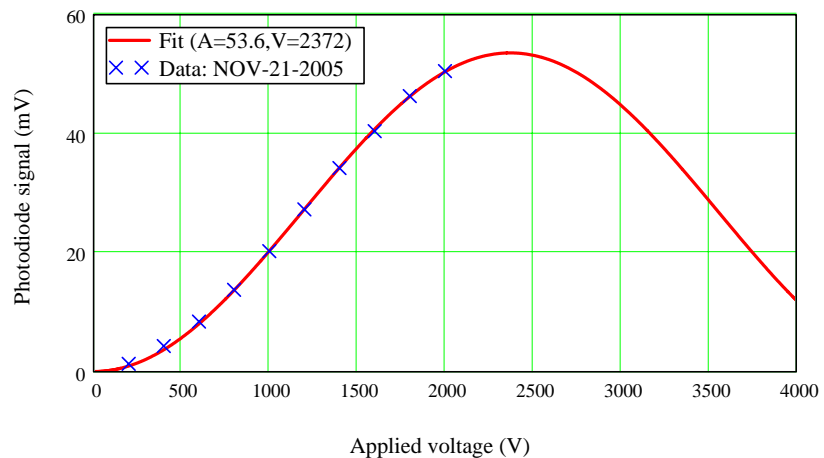


Figure 7.13: DC test of 532nm coated Pockels cell. Since the photodiode signal is 76 mV with the crossed polarizers and Pockels cell removed, the fit value for A (53.6 mV) implies an efficiency of $e \sim 70\%$. Some of the attenuation may be due to the fact the laser wavelength of 543nm is different than the AR coating wavelength. The polarizers will also contribute to the attenuation factor for the system.

polarization rotation. By placing the Pockels cell between two crossed polarizers (10LP-VIS, Newport), the complete system (crossed polarizers and Pockels cell) becomes a light gate with respect to the applied voltage. If the cell is in a state where the polarization is not rotated, then light cannot pass through the system. However, if the Pockels cell rotates the beam polarization, significant power can begin to pass through the system. Maximum transmission occurs when the beam polarization is rotated 90°. Specifically [67],

$$P_{out}(V_a) = P_{in}e \sin^2\left(\frac{\pi V_a}{2V}\right) \quad (7.3.1)$$

where P_{out} is the power downstream the system, P_{in} is the power incident the system, e is the efficiency of the system, V_a is the applied voltage, and V is the voltage at which maximum transmission occurs.

The mount for the Pockels cell provides delicate adjustment of the cell's orientation and clearance for the high voltage connectors. The Pockels cell is sensitive to yaw and pitch, requiring fine adjustment, while coarse adjustment of the roll angle and translation was sufficient. A transformer which increases the pulse height by a factor of two is placed close to the Pockels cell. The connection between the Pockels cell and the transformer is made using short wires about 2" in length. This connection produces a lot of RF noise when the cell is run at high voltages and needs to be shielded to prevent interference with sensitive instruments. A simple tin foil shell was sufficient.

To determine the voltage at which the plane of polarization of a linearly polarized beam is rotated by 90° when run through the Pockels cell, a Hammarlung DC test power supply was used. A collimated CW green HeNe beam was chopped (50% duty cycle at 200Hz) and sent through the crossed polarizer/Pockels cell system. A large area photodiode (Thorlabs PDA55) was used to detect the power transmitted through the system. A few ND filters were placed upstream the photodiode to select appropriate power levels for the diode. The output of the DC power supply was directly connected to the input terminals of the Pockels cell; thus, when the power supply's foot switch was depressed, the voltage applied to the Pockels cell could be read directly from the meter on the supply. Once the Pockels cell was activated in this manner, the corresponding voltage (representing the power transmitted through the system) from the photodiode could be observed using an oscilloscope.

The input beam to the Pockels cell was vertically polarized, while the Pockels cell was oriented so that the high voltage input terminals were horizontal (the terminals were

pic #	Raw data				Calculations				comment
	Height (mV)	FWHM (ns)	10%-90% rise time (ns)	10%-90% fall time (ns)	corrected rise time (ns)	corrected fall time (ns)	FWHM form factor (ns)	FWHM corrected (ns)	
15	110	1.100	0.800	1.700	0.714	1.636	0.440	1.034	4" delay line
16	90	0.900	0.700	1.200	0.600	1.108	0.474	0.809	3" delay line
17	210	1.450	1.000	1.450	0.933	1.375	0.592	1.366	1ns delay line
18	225	3.250	1.100	1.800	1.039	1.740	1.121	3.115	2ns delay line

Figure 7.14: Pulse length data/calculation table. Data resulting from various delay lines are corrected for the limited temporal properties of the data acquisition system. The 1ns delay line is 7 7/8" long and the 2ns delay line is 15 3/4" long (from connector tip to connector tip).

at the “9 o’clock” position when facing downstream toward the cell). DC power supply voltages between 200V and 2000V were used in 200V steps. For each DC voltage applied to the Pockels cell, the corresponding voltage from the photodiode was recorded. A red HeNe was used for the Pockels cell coated for 628nm and a green HeNe was used for the 532nm coating. The data for each cell was fit to Equation 7.3.1. The coefficient $P_{in}e$ was fit as a single parameter A , so the efficiency of the system could be obtained indirectly by measuring the power incident the system and comparing it to the fit parameter A . See Figure 7.12 for the 628nm cell results, and Figure 7.13 for the 532nm results.

7.3.2 Pockels cells minimum pulse length

The dye laser generates 535.892nm output (held within 2 picometers by the “LambdaLok” feature of the dye laser) at 20Hz with 5ns pulse lengths using a Coumarin 153 dye pumped with a tripled Nd:YAG (355nm) beam. In order to shape the pulsed dye laser output with the Pockels cell, the YAG pump is synchronized with the Hg pulser (which runs the Pockels cell) so that the cell activates at the exact same time the dye laser pulse traverses the crossed polarizers (in the case of the dye laser, we use two polarizing cube beam splitters from Lambda Research Optics) and the cell. This is accomplished through the use of three HP 8015A pulse generators and a few delay lines. Pulser #1 is designated the “clock generator” and triggers the Hg pulser and the flashlamps in the YAG.

The trigger signal for the Hg pulser is sent directly while the TTL trigger signal for the flashlamps is delayed in pulser #2 (designated the “flashlamp delay generator”) by about 1060 μ s. This flashlamp delay is varied so that the Q-switch opens near the peak

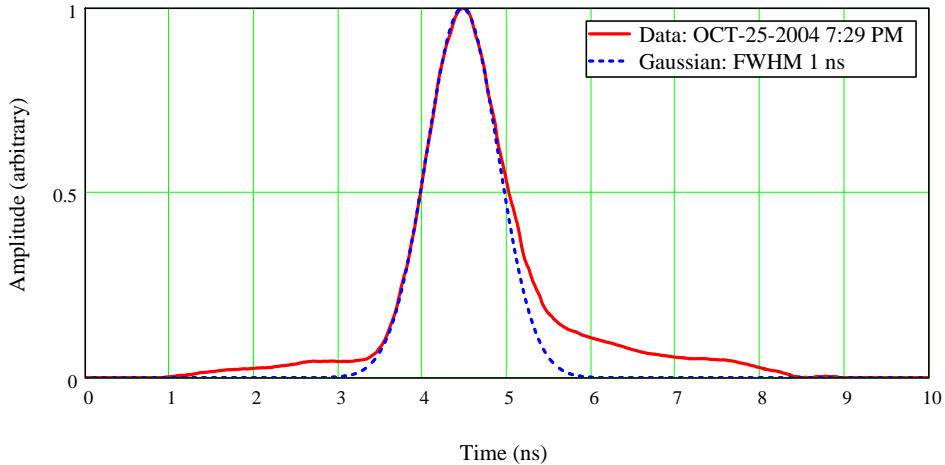


Figure 7.15: Pockels cell minimum pulse length (temporal profiles). Here the data corresponding to a 3" delay cable is overlaid with a computer generated Gaussian pulse. There is significant leaking before and after the pulse; this perhaps due to the relatively low (manufacturer specified) extinction ratio of 1k:1 for the polarizers (compared to 10k:1 for the polarizers used in the HeNe test) and the mismatch between the design wavelength and the laser wavelength.

of the flashlamp induced population inversion in the Nd:YAG rods; in our case this was about 340 μ s before the Q-switch delay generator (see below) TTL pulse. Upon receiving the trigger signal from the clock generator, the Hg pulser closes in about 1.4ms: the high voltage output pulse is to the Pockels cell through 220' of coax cable (introducing a fixed delay of 300ns) while the trigger output is sent to the Q-switch in the YAG.

On its way to the YAG's Q-switch input, the trigger signal from the Hg pulser is first sent through a 20dB attenuator and then through pulser #3 designated the "Q-switch delay generator", which adds about 200ns of variable delay. This TTL delay pulse is adjusted to that the subsequent dye laser pulse (the activated Q-switch generates a YAG pulse which in turn generates a dye laser pulse) arrives at the Pockels cell at the exact moment the Pockels cell is activated; in our case this was about 80ns before the Pockels cell is activated. A paper target is placed at the output of the optical switch and the scattered light from the target is observed using a fast photodiode (Electro-optics ET-2000).

For the Hg pulser, a delay line controls the pulse length. The high voltage output pulse is split: half of the signal is sent to the Pockels cell while the other half is sent down an un-terminated (delay line) cable. The high voltage rise reflects inverted from the open end of the cable and returns to cancel the signal sent to the Pockels cell – this terminates

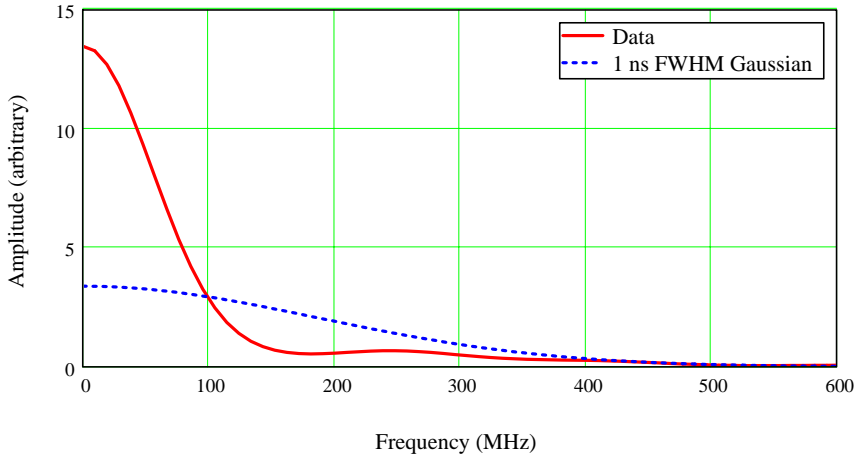


Figure 7.16: Pockels cell minimum pulse length (spectral profiles). The power spectrum of the pulses in Figure 7.15 (from a FFT of the temporal profiles) are show here. The leaking results in significant distortion from the optimal Gaussian profile.

the voltage signal. Thus, the height of the output pulse is half the charging line voltage. Moreover, the pulse length is twice the delay line travel time and the falling edge should have a similar shape as the rising edge. In fact the falling edge shape will always be a distorted version of the rising edge shape due to the inherent frequency dependent attenuation and phase shift introduced by the losses in real cables. We are able to produce fairly symmetric looking pulses out to 200 ns using typical coaxial cable as a delay line.

To determine the minimum pulse length obtainable, a 7" delay line is successively shortened (using wire cutters) by 1" increments and the resulting laser pulses at each length are observed on a Tektronix 7104 oscilloscope. The pulse images are recorded using a Polaroid camera attachment for the scope. The Polaroid prints were then analyzed with dividers and a straight edge to determine the height (in mV), the rise and fall times (in ns), and the FWHM (in ns) of each photographed trace. Given the rise/fall time of the photodiode (200/350ps) and the rise/fall time of the oscilloscope (300ps), the rise/fall time and FWHM measurements from the Polaroid images can be corrected using the following formulae

$$t_r^2 = \tau_r^2 + p_r^2 + s_{rf}^2, \quad (7.3.2)$$

$$t_f^2 = \tau_f^2 + p_f^2 + s_{rf}^2, \quad (7.3.3)$$

$$t_w = f_w(t_r + t_f), \quad (7.3.4)$$

and

$$\tau_w = f_w(\tau_r + \tau_f) \quad (7.3.5)$$

where p_r is the photodiode rise time, p_f is the photodiode fall time, p_r is the photodiode rise time, s_{rf} is the Tektronix 7104 rise/fall time, t_r is the measured rise time, t_f is the measured fall time, t_w is the measured FWHM, τ_r is the corrected rise time, τ_f is the corrected fall time, f_w is the FWHM form factor, and τ_w is the corrected FWHM.

We found that a 3" delay cable produced the best results; see Figure 7.14 for a data/calculation table. To determine the degree to which the output pulse approximates a Gaussian, a power spectrum of the (uncorrected) temporal envelope is calculated. See Figure 7.15 and 7.16 for the results. It is found that "leaking" caused by poor polarizer extinction ratios can significantly distort the power spectrum profile from the Gaussian case.

7.3.3 Pinholes

The envelope for the TEM00 mode from dye laser #21 is calculated for the beam line described in figures 7.11 and 7.8. Equations 6.1.3 and 6.1.4 are used to propagate the complex source point q down the beam line. We obtain the following complex source points for key points along the beam line ($\lambda = 725$ nm):

$$q_0 = 1.346 + 8.495i, \quad (7.3.6)$$

$$q_{50} = -1.022 + 0.114i, \quad (7.3.7)$$

$$q_{54} = -3.144 + 5.885i, \quad (7.3.8)$$

$$q_{295} = -0.515 + 0.036i, \quad (7.3.9)$$

where the subscript denotes the milepost at which the complex source is reported. See figure 7.17 for a plot of the beam envelope up to the pinhole. The beam lines for the three dye lasers are very similar. So, without corresponding plots like figure 7.17, we report the complex source at key points along the beam lines for dye laser #22 and #23. For dye laser #22 we have ($\lambda = 628$ nm)

$$q_0 = 1.346 + 9.808i, \quad (7.3.10)$$

$$q_{50} = -1.016 + 0.099i, \quad (7.3.11)$$

$$q_{55} = -4.008 + 4.493i, \quad (7.3.12)$$

$$q_{344} = -0.515 + 0.040i; \quad (7.3.13)$$

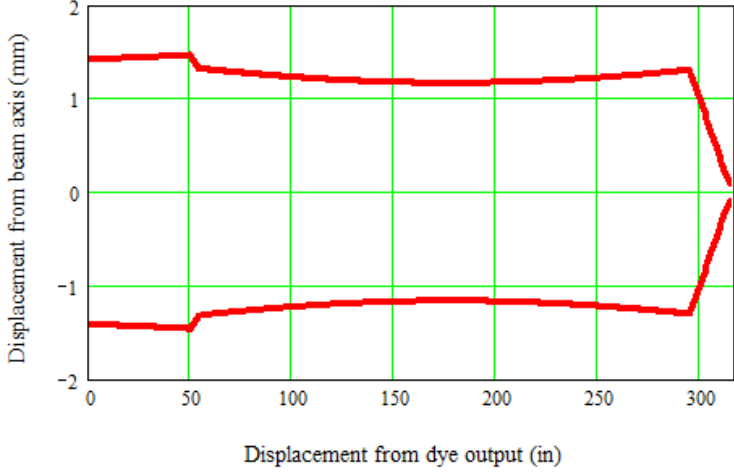


Figure 7.17: TEM00 envelope for dye laser #21

and for dye laser #23 we have ($\lambda = 872$ nm)

$$q_0 = 1.346 + 7.063i, \quad (7.3.14)$$

$$q_{50} = -1.031 + 0.135i, \quad (7.3.15)$$

$$q_{52.5} = -0.707 + 7.018i, \quad (7.3.16)$$

$$q_{280} = -0.516 + 0.025i. \quad (7.3.17)$$

Note that the initial complex source point is slightly different for each laser. This is because the waist was fixed and the Rayleigh parameter was recalculated given the different wavelength of each laser. The far field diffraction pattern of a uniformly illuminated pinhole is the well known Airy function. The radial displacement r_1 of the first minimum some distance z down the beam line is given by [67]

$$r_1 = z \frac{1.22\lambda}{2r}, \quad (7.3.18)$$

where λ is the wavelength of the incident beam, and r is the pinhole radius. The Rayleigh range for a circular aperture is [67]

$$z_R = \frac{\pi r^2}{\lambda}. \quad (7.3.19)$$

For distances $z > z_R$ we will assume to be in the far field limit. For the beam line in figure 7.8, the pinholes (b), (e), and (h) are 0.2 m upstream from +0.2 m lenses. Suppose the pinholes have a diameter of 25 μm and consider the beam from dye laser #21 (725 nm).

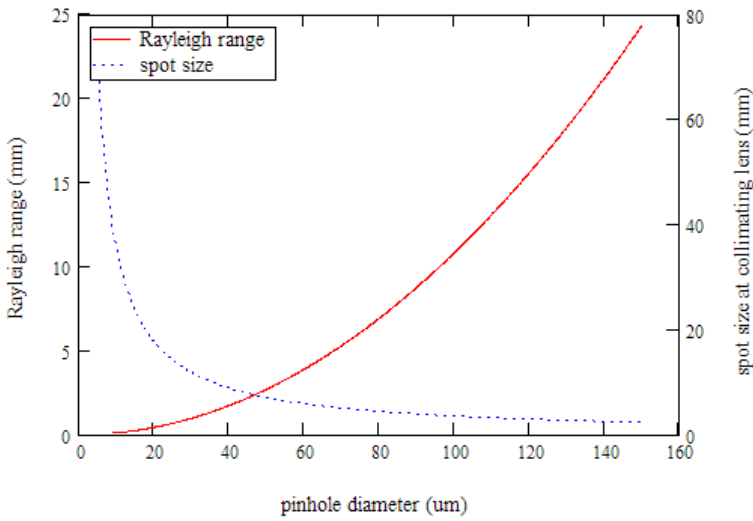


Figure 7.18: Rayleigh range (724 nm) and spot size vs. pinhole diameter. Even with a pinhole as large as 150 μm the Rayleigh range for the pinhole function is only 24.374 mm while the spot size 20 cm from the pinhole is 2.359 mm in diameter. For a pinhole with a diameter of 50 μm the Rayleigh range is 2.708 mm and the spot size at 20 cm is 7.076 mm.

The Rayleigh range for this pinhole is 677 μm ; thus, the lenses are in the far field. At the lens the radial displacement of the first minimum is 7.076 mm, yielding a semi-Gaussian (by placing a 14.2 mm aperture before the +0.2 m lens) beam with a full width of about 14 mm. See figure 7.18.

Damage threshold

In the following analysis we will assume the beams involved have a circular top-hat intensity distributions for simplicity.

Pinholes made to handle high power from standard suppliers typically have a damage threshold of around 1MW/mm². Given a waist at the pinhole of about 80 μm , we can only use 4.4 ns pulses with about 100 μJ of energy. The ratio of the area of the pinhole to the total area of the beam implies that only 10% of the energy incident on the pinhole makes it through. Since the central maximum of the Airy function contains about 84% of the energy in the pinhole, the beam after the +0.2 m lens can have about 8 μJ of energy at most. This 8 μJ is then run through an aperture before the iodine cell. If this aperture has a radius of around 1 mm then the energy of the beam at the iodine sample is about 160 nJ. This is 2 to 3 orders of magnitude less than our estimate of the energy needed at

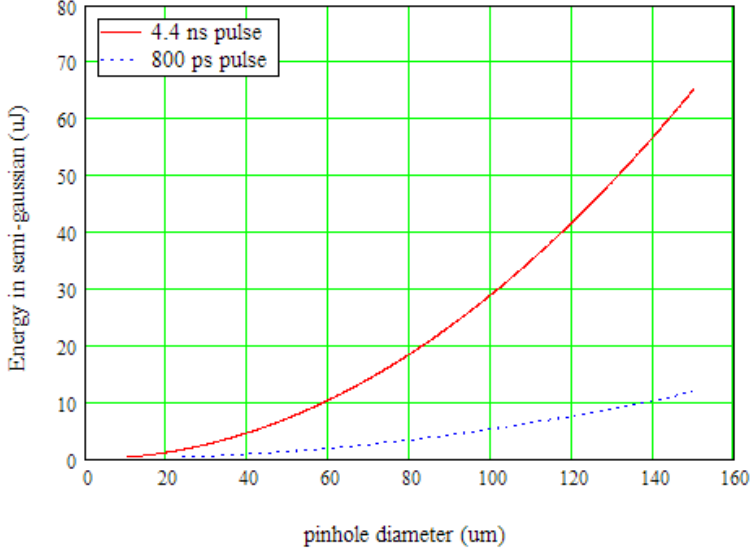


Figure 7.19: Energy in the Airy function central max vs. pinhole size.

the iodine sample for coherent control. Thus, an ordinary metallic pinhole may not be the best choice. A glass fiber will be better: the only limit is the surface damage threshold of the glass: around $5\text{GW}/\text{cm}^2$. See figure 7.19.

7.3.4 General discussion on etalon efficiency

We seek a relationship between the resolution and power transmittance of a etalon type interferometer. Interferometers are subject to the localization property from (spatial) Fourier analysis:

$$\Delta x \propto \frac{1}{\Delta k} \quad (7.3.20)$$

where Δx is the width of some localized feature in space and Δk is the corresponding width in inverse space. In optical interferometers, Δk is the “resolution” of the resulting interferogram and Δx is the largest optical path length difference associated with the interferometer. In the case of a etalon type interferometer Δx is equal to the optical path length of the etalon medium times the number of passes the reflection coatings can support; thus, we will assume

$$\Delta x \propto n \equiv \frac{1}{1 - R} \quad (7.3.21)$$

where n is the number of passes and R is the reflectance transmission of the etalon coating. This is reasonable when one considers that this implies Δx diverges toward infinity as R

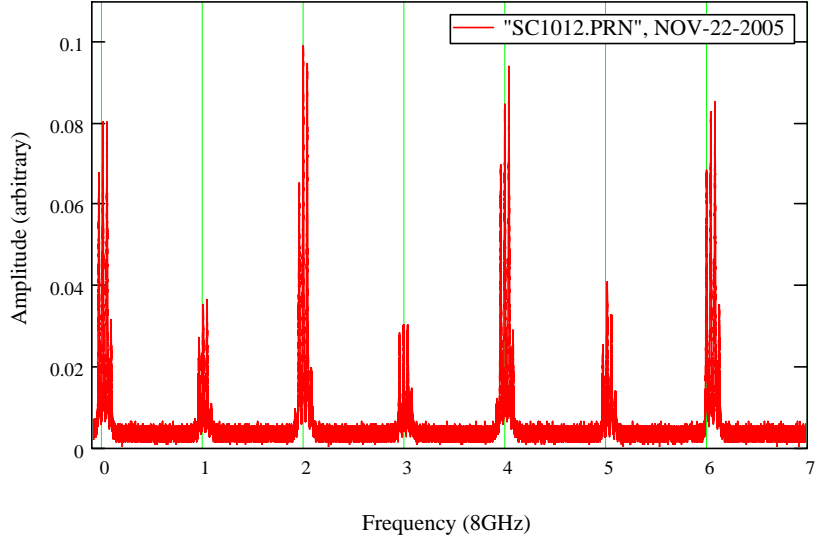


Figure 7.20: Green HeNe transmission through a scanned confocal etalon

approaches unity and the fact that if $R = 0.9$ then one would expect about ten reflections until the beam would no longer contribute significantly to the etalon's interference effect.

The power transmittance of the etalon is a function of the losses at each mirror and the bulk absorption in the etalon material. Clearly, a reasonable form for the power transmission is

$$T \propto \gamma^n = \gamma^{1/(1-R)} = \gamma^{\zeta \Delta x}. \quad (7.3.22)$$

where γ is the transmission of one pass (representing the effects of reflection and bulk losses) and ζ is a constant with units of inverse length. Moreover, application of the localization property gives

$$T \propto \gamma^{\zeta/\Delta k}. \quad (7.3.23)$$

Thus, we see that because $\gamma < 1$, any attempt to increase the resolution of the instrument will result in a reduction in power transmission.

7.3.5 Confocal etalon test

The Burleigh SA-Plus confocal etalon is tested on green HeNe output. This etalon is designed for laser beam analysis; however, in this test we attempt to investigate the possibility of using this type of etalon as a spectral filter for the dye laser output.

The output of a green HeNe is collimated using a telescope. The resulting beam is directed to the input of the confocal etalon. Careful alignment is required for optimal performance so a mount is assembled giving the proper number of adjustable parameters. The output of the etalon is then collected with a positive lens and focused onto the sensitive area of a photodiode. The diode is viewed on a digital oscilloscope which also provides a storage function so that scope traces can be easily transported to a computer.

The rear mirror of the etalon is allowed to translate under the action of a piezo actuator. Translating the cavity mirror essentially “sweeps” the comb band pass function of the etalon across the (stationary) laser line. If a voltage ramp is used to drive the piezo and the scope sweep, periodic maxima appear corresponding to each comb “tooth” that passes over the laser line. The mode spacing in the etalon used here is 8 GHz (this is half of the FSR since the etalon is confocal [76]) thus the scans can be calibrated as long as two maxima appear.

Optimal alignment for laser beam analysis is achieved when the half axial modes of confocal cavities can be identified and the full FSR of 16 GHz is apparent [76]. See Figure 7.20 for a scope trace resulting from such an alignment. The maxima alternate in height with the tall peaks corresponding to the axial modes of the cavity and the short peaks the displaced odd transverse modes (the so called “half axial” modes). Within each maxima an inner structure is seen. Figure 7.21 is a zoom into one of the axial peaks in the trace.

Figure 7.22 show the output of the etalon when run in a “near-confocal” geometry. The etalon modes become non-degenerate and can be selected by adjusting the DC voltage to the piezo. When run in this mode with the TEM00 selected, the output of the etalon is not visible (even when focused) in room light.

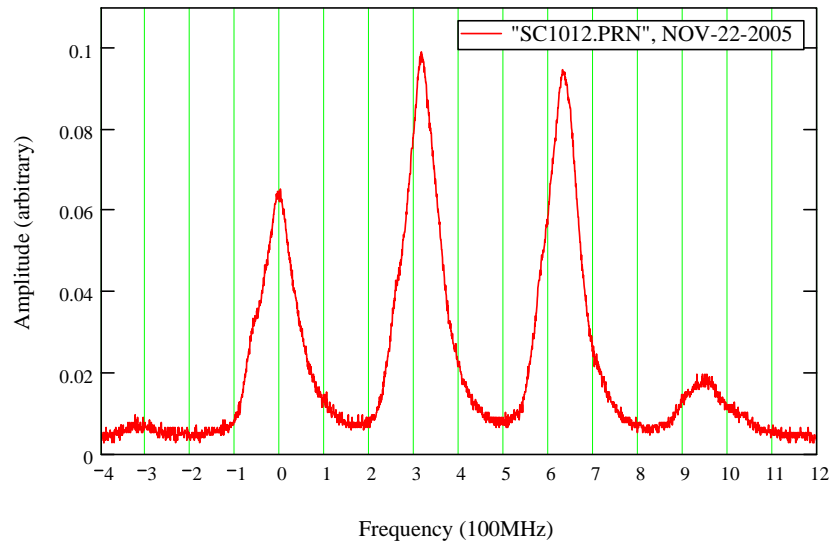


Figure 7.21: Green HeNe transmission through a scanned confocal etalon (zoom)

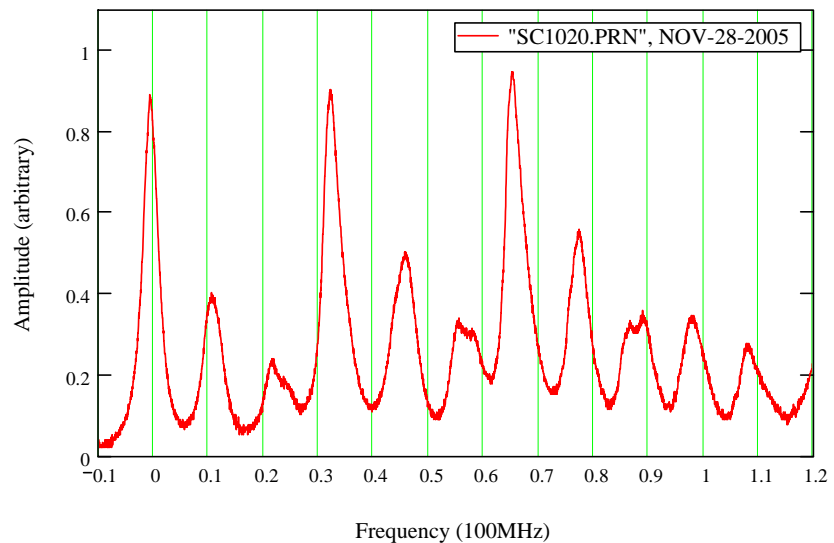


Figure 7.22: Green HeNe transmission through a scanned near confocal etalon

Chapter 8

Conclusion

This investigation into the application of quantum control techniques to LIDAR systems shows the theoretical potential, and details the experimental complexities involved in the merger. Atmospheric conditions are expected to force the interaction time to sub nanosecond time scales and the scale of molecular coupling constants demand a high fluence to induce the coherent processes under investigation. The only commercial broadly tunable laser source available with mJ pulse energies at the nanosecond time scale are dye lasers. As an option to undergoing the line of research outlined in [19] passive filtering techniques are explored.

Numerical studies of some coherent population transfer processes reveal some potential advantages these experimental techniques may have on the LIDAR problem. The “robustness” of the STIRAP with respect to the coupling yields near complete population inversion (even in a randomly polarized ensemble) and top hat spatial inversion profiles (even when using Gaussian beams). The “ridge” detuning feature may seem like a disadvantage at first; however, considering the Gaussian-like falloff when traversing the anti-ridge, this detuning feature may be exploited, for instance, to reduce the coupling to a particularly strong non-target transition to a degree not possible with Lorentzian-like detuning features. In the numerical studies mentioned above, the open nature of the problem is ignored. A simple model for the collision process combined with a parametric fit produced some intriguing initial results suggesting a mathematical form for the inclusion of relaxation processes into future numerical studies of open systems.

In the investigation into the application of these processes on thermal molecular systems, iodine is used as the trial system since its energy structure is well understood. To make headway simulating molecular response to pulses laser output without a tractable

dynamical model for molecular systems, a crude model is implemented and fluorescence responses are approximated. These numerical studies imply fluorescence extinction ratios around 10^{-8} .

A set of fundamental measurements serve as a guide to develop the laboratory techniques, apparatus, and data acquisition systems appropriate for these types of synchronized pulsed laser experiments on thermal molecular systems. The 1 m monochromator available in the lab is fitted with a PMT and, for most fluorescence measurements, this system was adequate; however, in aromatic compound LIF experiments, the monochromator was shown to exhibit significant “ghosting”, prompting a grating upgrade. The chart recorder has been replaced with a ADC/LabView system allowing long run times (some of the laser diagnostic scans were over two hours in length) and, because of its digital format, the data is immediately amenable to digital processing. The iodine broadband absorption tests generated a set of LED light sources; which could further be used to test the Hg pulser and a fast photodiode. The HeNe LIF experiments were used to try different beam line geometries: sideview and backscatter.

The dye laser performance tests provide insight into the complexities of these types of experiments. The wavelength “scan” feature of the dye lasers is not stable: it can not be used to determine the positions of absorptions features in molecular iodine. Upon the arrival of a CCD based laser beam profile imager, it is shown that the dye laser output contains more than a few spatial modes. RF analysis of the dye laser pulse intensity profiles revealed a axial mode structure with discrete features extending out to 1.8 GHz (at least) with 240 MHz spacing. Not only is the 240 MHz spacing inconsistent with the manufacturer’s specifications; but it exposes a property of the laser output that must be dealt with before coherent control experiments can succeed.

The sources of the multi-mode nature of the dye laser are fundamental to the operation of its cavity. The lasing medium has a broad gain bandwidth – this provides it with broad tunability at the cost of supporting a family of modes in the cavity instead of one. To get into the mJ range in pulse energy, it is required to place the lasing modes very close to the walls of the dye flow cells. In this way the pumping efficiency is optimized, but at the cost of symmetric cavity modes. The dye cavity does not consist of two spherical mirrors; instead it has one output coupler (spherical) and two gratings. It is not clear what the dominant modes would be in such a resonator. The fact that the gain medium is suspended in a flowing solvent subject to periodic intense bursts of radiation makes the

idea of a feedback system to stabilize the cavity modes to optical path length modulations daunting. In the literature, there is one example of a single mode dye laser system made specifically for coherent control experiments [19], but this system was severely limited in tunability making it useless for the exploratory demonstration experiments needed in the research proposed in this dissertation.

Tasks for future development must include a system to condition the dye laser output. Pinholes and confocal etalons are considered as spatial filters. The pinhole method is limited by the damage threshold of the pinhole material – glass fibers may be the best option here. Near confocal etalons can be used to generate single mode output from multimode input and etalon mirrors can be made with high damage thresholds. This gives some hope to the possibility that a near confocal etalon may be able to solve both the transverse and axial mode problems simultaneously. Unfortunately, the multi-pass nature of the etalon places a fundamental limit on the transmitted power – this limit decreases as resolution increases. The etalon tested here reduced 5 mW CW Green HeNe output such that the scattered radiation from a white target was not visible in room light.

The temporal shaper must also be developed since optimal Pockels cell performance has not been achieved. Current efforts are centered on a replacement for the cube beam splitters as the high power polarizer. A “pile-of-plates” ZnSe polarizer has been assembled but has not been tested with the Pockels cell. There may also be an issue with the Pockels cell itself. Even when used in the beam waist, the Pockels cell causes significant leakage between two crossed polarizers.

A data acquisition system must be developed to handle the stochastic nature of the experiment. Given the dye laser diagnostics presented here it is apparent that not only will the dye laser output be significantly reduced after passing through the temporal and modal filters, but its amplitude will not be able to be controlled. Discriminators might render the duty cycle of the three color experiment unworkable, so each run of the experiment will have to be recorded. This means at least four data channels: one for each of the three input laser pulses and one for the resulting fluorescence. This shot-to-shot requirement may eliminate the possibility of a sensitive CCD array in the data acquisition chain.

An immediate extension to this research is to include other molecular systems. This line of research has started with the cursory investigation of aromatics. In view of the difficulties described here with respect to multicolor coherent population transfer, this ex-

tension should await a successful demonstration in molecular iodine unless the iodine system proves untenable and an alternative molecular (or atomic) system has to be considered.

In addition to other targets, extensions could also include other coherent processes. The multi-color LIDAR idea presented here can be extended to more colors and/or separate packets. For example, the first multi-color packet could “prepare” the atmosphere in some way to help the secondary multi-color packets [56, 23, 73, 58, 32]. Moreover, the processes selected for investigation here were simply plucked from the current literature. Other novel processes exist; for example, the “quantum zeno” effect [41, 21] may allow selective control of the decay process in target molecules [42]. Thus, not only could we exploit the large spectral shift of fluorescence energy, but also a possible *temporal* shift of the fluorescence energy.

Finally, there may be implications into other areas of research; for example, these types of experiments (tunable laser targeting molecular systems) could be used to explore the field of quantum computing. [31] theoretically explores the possibility of “ensemble quantum computing” using multi-color optical spectroscopy of molecules. This remains one of the most exciting possibilities.

Bibliography

- [1] *Defining, measuring, and optimizing laser beam quality*, volume 1868, Los Angeles, CA, August 1993. Laser resonators and coherent optics: Modeling, technology, and applications; Proceedings of the Meeting.
- [2] *Phaseonium: Media of Unusual Optical Properties*, Washington, D.C., August 1997. Proceedings of SPIE – Volume 3186.
- [3] *Pump-and-Probe Lidar: OH kinetics Study for determining a New Indicator for the Ozone Production*, Annapolis USA, 1998. Proc., 19th ILRC.
- [4] *Fault Scarp Detection Beneath Dense Vegetation Cover: Airborne LIDAR Mapping of the Seattle Fault Zone, Gainbridge Island, Washington State*, Washington, D.C., May 2000. Proceedings of the American Society of Photogrammetry and Remote Sensing Annual Conference.
- [5] *Applications of Airborne LIDAR Mapping in Glacierised Mountainous Terrain*, Sydney, Australia, 2001. Geoscience and Remote Sensing Symposium, 2001. IGARSS '01. IEEE 2001 International.
- [6] *Modeling of collection efficiency in lidar spectroscopy*, San Diego, California, Spetember 2005. Proceedings of SPIE – Volume 5887, Lidar Remote Sensing for Environmental Monitoring VI, Upendra N. Singh, Editor.
- [7] L. Allen and J. H. Eberly. *Optical Resonance and Two-Level Atoms*. Dover Publications, Inc, New York, 1987.
- [8] E. Arimondo. Coherent population trapping in laser spectroscopy. *Progress in Optics*, 35:257, 1996.

- [9] Y. B. Band and P. S. Julienne. Density matrix calculation of population transfer between vibrational levels of na2 by stimulated raman scattering with temporally shifted laser beams. *Journal of Chemical Physics*, 94(8):5291–5298, April 1991.
- [10] I. V. Bargatin and B. A. Grishanin. Fluorescence and absorption spectra of the λ -system in the case of raman resonance. *Optics and Spectroscopy*, 87(3):400–408, 1999.
- [11] K. Bergmann, H. Theuer, and B. W. Shore. Coherent population transfer amoung quantum states of atoms and molecules. *Reviews of Modern Physics*, 70(3):1003–1025, 1998.
- [12] Z. Bialynicka-Birula, I. Bialynicka-Birula, J. H. Eberly, and B. W. Shore. Coherent dynamics of n-level atoms and molecules. ii. analytic solutions. *Physical Review A*, 16(5):2048–2054, November 1977.
- [13] F. Bloch. Nuclear induction. *Physical Review*, 70:460–474, October 1946.
- [14] Karl Blum. *Density Matrix Theory and Applications*. Plenum Press, New York, 1981.
- [15] B. H. Bransden and C. J. Joachain. *Introduction to Quantum Mechanics*. Longman Group UK Limited, Essex, England, 1989.
- [16] J. Cao, C. J. Bardeen, and K. R. Wilson. Molecular " π pulse" for total inversion of electronic state population. *Physical Review Letters*, 80(7):1406–1409, February 1998.
- [17] A. S. Choe, Jaemin Han, and Jongmin Lee. Nonadiabatic loss in coherent population transfer due to optimal detunings. *Journal of the Korean Physical Society*, 31(4):703–707, 1997.
- [18] Claude Cohen-Tannoudji and Serge Reynaud. Dressed-atom description of resonance fluorescence and absorption spectra of a multi-level atom. *J. Phys. B: Atom. Molec. Phys.*, 10(3):345–363, 1977.
- [19] John D. Corless, James A. West, Jake Bromage, and Jr. C. R. Stroud. Pulsed single-mode dye laser for coherent control experiments. *Review of Scientific Instruments*, 68(6):2259–2264, June 1997.
- [20] M. V. Danileiko, V. I. Romanenko, and L. P. Yatsenko. Landau–zener transitions and population transfer in a three–level system driven by two delayed laser pulses. *Optics Communications*, 109:462–466, 1994.

- [21] F. B. do Jong, R. J. C. Spreeuw, and H. B. van Linden van den Heuvell. Quantum zeno effect and v-scheme lasing without inversion. *Physical Review A*, 55(5):3918–3922, 1997.
- [22] J. L. Dunham. The energy levels of a rotating vibrator. *Physical Review*, 41:721–731, September 1932.
- [23] J. H. Eberly. Area theorem rederived. *Optics Express*, 2(5):173–176, March 1998.
- [24] U. Fano. Description of states in quantum mechanics by density matrix and operator techniques. *Reviews of Modern Physics*, 29(1):74–93, January 1957.
- [25] F. G. Fernald. Analysis of atmospheric lidar observations: some comments. *Applied Optics*, 23:652, 1984.
- [26] U. Gaubatz, P. Rudecki, M. Becker, S. Schiemann, M. Klz, and K. Bergmann. Population switching between vibrational levels in molecular beams. *Chemical Physics Letters*, 149:451–586, 1988.
- [27] S. Gerstenkorn and P. Luc. Molecular constants describing the b-x transitions of i2(127,129) and i2(129,129). *Canadian Journal of Physics*, 69:1299–1303, 1991.
- [28] S. Gerstenkorn, P. Luc, and J. Verges. On the ground vibrational level of the a(3)pi(1u) state of the i2 molecule. *Journal of Physics B: Atomic, Molecular and Optical Physics*, pages L193–L196, 1981.
- [29] S. Godin-Beekmann, J. Porteneuve, and A. Garnier. Systematic dial lidar monitoring of the stratospheric ozone vertical distribution at observatoire de haute-provence (43.92 degrees n, 5.71 degrees e). *Journal of Environmental Monitoring*, 5(1):57–67, 2003.
- [30] J. E. M. Goldsmith, F. H. Blair, S. E. Bisson, , and D. D. Turner. Turn-key raman lidar for profiling atmospheric water vapor, clouds, and aerosols. *Applied Optics*, 37:4979–7990, 1998.
- [31] Debabrata Goswami. Laser phase modulation approaches towards ensemble quantum computing. *Physical Review Letters*, 88(17):17901, April 2002.
- [32] R. Grobe, F. T. Hioe, and J. H. Eberly. Formation of shape-preserving pulses in a nonlinear adiabatically integrable system. *Physical Review Letters*, 73(24):3183–3186, December 1994.

- [33] T. Halfmann and K. Bergmann. Coherent population transfer and dark resonances in so2. *Journal of Chemical Physics*, 104:7068–7072, May 1996.
- [34] T. W. Hänsch and H. Walther. Laser spectroscopy and quantum optics. *Reviews of Modern Physics*, 71(2):242–252, 1999.
- [35] S. E. Harris, J. E. Field, and A. Imamoglu. Nonlinear optical processes using electromagnetically induced transparency. *Physical Review Letters*, 64(10):1107–1110, 1990.
- [36] Stephen E. Harris. Electromagnetically induced transparaency. *Physics Today*, pages 36–42, July 1997.
- [37] Sadri Hassani. *Mathematical Physics*. Springer, New York, February 2002.
- [38] Eugene Hecht. *Optics*. Addison Wesley, New York, 2nd edition, 1987.
- [39] Gerhard Herzberg. *Molecular Spectra and Molecular Structure: Spectra of Diatomic Molecules*. D. Van Nostrand Company, Inc., Princeton, New Jersey, 1950.
- [40] J. Höffner and J. S. Friedman. Metal layers at high altitudes: A possible connection to meteoroids. *Atmos. Chem. Phys. Discuss.*, 4:399–417, 2004.
- [41] D. Home and M. A. B. Whitaker. A conceptual analysis of quantum zeno; paradox, measurement, and experiment. *Annals of Physics*, 258:237–285, 1992.
- [42] Wayne M. Itano, D. J. Heinzen, J. J. Bollinger, and D. J. Wineland. Quantum zeno effect. *Physical Review A*, 41:2295–2300, 1990.
- [43] Richard S. Judson and Hershel Rabitz. Teaching lasers to control molecules. *Physical Review Letters*, 68:1500–1503, March 1992.
- [44] P. L. Kelley, P. J. Harshman, O. Blum, and T. K. Gustafson. Radiative renormalization analysis of optical double resonance. *J. Opt. Soc. Am. B*, 11(11):2298–2302, November 1994.
- [45] Navin Khaneja, Burkhard Luy, and Steffen J. Glaser. Boundary of quantum evolution under decoherence. *Proceedings of the National Academy of Sciences*, 100(23):13162–13166, November 2003.

- [46] Z. Kis and S. Stenholm. Optimal control approach for a degenerate stirap. *Journal of MODern Optics*, 49:111–124, 2002.
- [47] James F. Koehler. Quenching of iodine fluorescence by iodine and argon. *Physical Review*, 44:761–768, 1933.
- [48] J. B. Koffend, R. Bacis, and R. W. Field. The electronic transition moment of the bo(+u)-x(1)sigma(+g) system of i₂ through gain measurements of an i₂ optically pumped laser. *Journal of Chemical Physics*, 70:2366–2372, March 1979.
- [49] J. R. Kuklinski, U. Gaubatz, F. T. Hioe, and K. Bergmann. Adiabatic population transfer in a three-level system driven by delayed laser pulses. *Physical Review A*, 40:6741–6744, 1989.
- [50] M. Lamrini, R. Bacis, D. Cerny, S. Churassy, P. Crozet, and A. J. Ross. The electronic transition dipole moment of the bo(+u)-xo(+g) transition in iodine. *Journal of Chemical Physics*, 100:8780–8783, 1993.
- [51] E. L. Lewis, C. W. P. Palmer, and J. L. Cruickshank. Iodine molecular constants from absorption and laser fluorescence. *American Journal of Physics*, 62:350–356, 1993.
- [52] E. L. Lewis, C. W. P. Palmer, and J. L. Cruickshank. Iodine molecular constants from absorption and laser fluorescence. *American Journal of Physics*, 62:350–356, 1994.
- [53] William H. Louisell. *Coupled Mode and Parametric Electronics*. John Wiley & Sons, Inc., New York, 1960.
- [54] Alfredo Luis. Quantum-state preparation and control via the zeno effect. *Physical Review A*, 63(5):052112, Apr 2001.
- [55] F. Martin, R. Bacis, S. Churassy, and J. Verges. Laser-induced-fluorescence fourier transform spectrometry of the xo(+g) state of i₂: Extensive analysis of the bo(+u)-xo(+g) fluorescence spectrum of 127i₂. *Journal of Molecular Spectroscopy*, 116:71–100, 1986.
- [56] S. L. McCall and E. L. Hahn. Self-induced transparency. *Physical Review*, 183(2):457–485, July 1969.

- [57] Gregory A. Neumann, David D. Rowlands, Frank G. Lemoine, David E. Smith, and Maria T. Zuber. Crossover analysis of mars orbiter laser altimeter data. *Journal of Geophysical Research*, 106(E10):23753–23768, October 2001.
- [58] J. Oreg, F. T. Hioe, and J. H. Eberly. Adiabatic following in multilevel systems. *Physical Review A*, 29(2):690–697, February 1984.
- [59] G. E. Pake. *Paramagnetic Resonance*. W. A. Benjamin, Inc., New York, 1962. 16–39.
- [60] Christopher Palmer. *Diffraction Grating Handbook*. Thermo RGL, Rochester, New York, 2002.
- [61] Anthony P. Peirce, Mohammed A. Dahleh, and Herschel Rabitz. Optimal control of quantum-mechanical systems: Existence, numerical approximation, and applications. *Physical Review A*, 37:4950–4964, June 1988.
- [62] William H. Press, Brian P. Flannery, Saul A. Teukolsky, and William T. Vetterling. *Numerical Recipes in C*. Cambridge University Press, New York, NY, 2 edition, 1992.
- [63] J. Qi, F. C. Spano, T. Kirova, A. Lazoudis, J. Magnes, L. Li, L. M. Narducci, R. W. Field, and A. M. Lyyra. Measurement of transition dipole moments in lithium dimers using electromagnetically induced transparency. *Physical Review Letters*, 88(17):173003, April 2002.
- [64] Herschel Rabitz, Regina de Vivie-Riedle, Marcus Motzkus, and Karl Kompa. Whither the future of controlling quantum phenomena. *Science*, 288:824–828, May 2000.
- [65] L. P. Rapoport, V. I. Lisitsin, and S. M. Yazykova. Semi-emperical calculation method for the variation of electronic transition moments in diatomic molecules. *Journal of Physics B*, 10(17):3359–3363, 1977.
- [66] V. I. Romanenko and L. P. Yatsenko. Adiabatic population transfer in the three-level λ -system two-photon lineshape. *Optics Communications*, 140:231–236, 1997.
- [67] Bahaa E. A. Saleh and Malvin Carl Teich. *Fundamentals of Photonics*. Wiley-Interscience, New York, 1991.
- [68] S. Schiemann, A. Kuhn, S. Steuerwald, and K. Bergmann. Efficient coherent population transfer in no molecules using pulsed lasers. *Physical Review Letters*, 71(22):3637–3640, November 1993.

- [69] S. G. Schirmer. Laser cooling of internal molecular degrees of freedom for vibrationally hot molecules. *Physical Review A*, 63:013407, 2000.
- [70] M. Schmitt, G. Knopp, A. Materny, and W. Kiefer. Femtosecond time-resolved four-wave mixing spectroscopy in iodine vapour. *Chemical Physical Letters*, 280:339–347, 1997.
- [71] M. O. Scully and M. S. Zubairy. *Quantum Optics*. Cambridge University Press, Cambridge, United Kingdom, 1997.
- [72] Marlan O. Scully. From lasers and masers to phaseonium and phasers. *Physics Reports*, 219:191–201, October 1992.
- [73] Marlan O. Scully, Girish Saran Agarwal, Olga Kocharovskaya, Victor V. Kozlov, and Andrey B. Matsko. Mixed electromagnetically and self-induced transparency. *Optics Express*, 8(2):66–75, January 2001.
- [74] Raymond A. Serway. *Physics for Scientists & Engineers with Modern Physics*. Saunders College Publishing, Philadelphia, 1990.
- [75] B. W. Shore, J. Martin, M. P. Fewell, and K. Bergmann. Coherent population transfer in multilevel systems with magnetic sublevels. i. numerical studies. *Physical Review A*, 52(1):566–582, July 1995.
- [76] A. E. Siegman. *Lasers*. University Science Books, Sausalito, CA, 1986.
- [77] P. Sikora, P. Wiewior, P. Kowalczyk, and C. Radzewicz. Laser-induced fluorescence of i_2 molecule in an undergraduate student laboratory. *European Journal of Physics*, 18:32–39, 1997.
- [78] Ignacio T. Sola, Vladimir S. Malinovsky, and David J. Tannor. Optimal pulse sequences for population transfer in multilevel systems. *Physical Review A*, 60(4):3081–3090, October 1999.
- [79] Eric B. Szarmes, John M.J. Madey, and Karl D. Straub. Observation of a cw dark-field signal in an absorption spectroscopic experiment using a phase locked free-electron laser. *Physical Review Letters*, 84(13):2849–2852, March 2000.

- [80] J. Tellinghuisen. Transition strengths in the visible-infrared absorption spectrum of i2. *Journal of Chemical Physics*, 76:4736–4744, May 1982.
- [81] Joel Tellinghuisen. Intensity factors for the i2 b-x band system. *Journal of Quantitative Spectroscopy and Radiative Transfer*, 19:149–161, 1978.
- [82] E. B. Treacy. Adiabatic inversion with light pulses. *Physics Letters A*, 27:421–422, August 1968.
- [83] Nikolay V. Vitanov, Thomas Halfmann, Bruce W. Shore, and Klaas Bergmann. Laser induced population transfer by adiabatic passage techniques. *Annu. Rev. Phys. Chem.*, 52:763–809, 2001.
- [84] James Wei and Joel Tellinghuisen. Parameterizing diatomic spectra: "best" spectroscopic constants for the i2 b-x transition. *Journal of Molecular Spectroscopy*, 50:317–332, 1974.
- [85] T. C. Weinacht, R. Bartels, S. Backus, P. H. Bucksbaum, B. Pearson, J. M. Geremia, H. Rabitz, H. C. Kapteyn, and M. M. Murnane. Coherent learning control of vibrational motion in room temperature molecular gases. *Chemical Physics Letters*, 344(3):333–338, August 2001.
- [86] P. F. Williams, D. L. Rousseau, and S. H. Dworetsky. Resonance fluorescence and resonance raman scattering: Lifetimes in molecular iodine. *Physical Review Letters*, 32(5):196–199, 1974.
- [87] Q. Wu, D. J. Gauthier, and T. W. Mossberg. Optical resonance and coherent transients in dressed atomic systems. *Physical Review A*, 50(2):1474–1478, August 1994.
- [88] Amnon Yariv. *Quantum Electronics*. John Wiley & Sons, New York, 1989.
- [89] S. M. Yazykova and E. V. Butyrskaya. Mathematical justification of the r-centroid method in diatomic molecules. *Journal of Physics B*, 13:3361–3367, 1980.
- [90] K. Zaheer and M. S. Zubairy. Atom-field interaction without the rotation-wave approximation: A path-integral approach. *Physical Review A*, 37(5):1628–1633, March 1988.